ABSTRACT

NELSON, NOEL. Validation and Uncertainty Quantification of the Data Integration with Modeled Predictions (DIMP) Inverse Radiation Transport Model For Holdup Measurements. (Under the direction of Yousry Azmy and John Mattingly).

The original work performed by Hykes [1] validated the Data Integration with Modeled Predictions (DIMP) inverse particle transport method for Cs-137 and Co-60 point and line sources. The original source predictions were fairly accurate with a few minor limitations: source solutions were often placed within the walls of the room in cells adjacent to the true source location and the search space needed to be reduced for DIMP to converge. These limitations were suspected to arise from the low intensity of the source strengths and the large average intervening distances between detectors and sources. This work sought to explore this assumption through stronger, realistic simulated holdup source measurements in a laboratory setting, and by improving the DIMP models. Radioactive source holdup is the intended application, which involves nuclear material deposits that build up in processing equipment at nuclear facilities. Currently, the Generalized Geometry Holdup (GGH) method is often employed in several nuclear facilities to measure holdup. GGH is reasonable at quantifying amounts of material present and the approximate source distribution, but it requires a lot of initial measurements and planning to locate radioactive sources. The DIMP method takes an alternative approach of predicting radiation source locations, distributions, and strengths purely through grids of passive detector response measurements in a facility. The original DIMP optimization algorithm was improved by incorporating a basin-hopping global search algorithm in addition to the original Quasi-Newton line search algorithm. In global DIMP search iterations were added to randomly shake the optimizer out of local chi-squared minima wells and better explore the cost function space. First, a numerical convergence study was performed in order to determine the stability of the original local DIMP algorithm and the sensitive input parameters within DIMP. DIMP proved to be conditionally stable when detectors were not placed overly close to the source of interest. Sensitive parameters included the detector response function (DRF) and the detector location. Also, a study was performed using unshielded (bare) detector responses only on Hykes's Cs-137 point source, which is advantageous for higher detector efficiencies, simpler DRF models, and full 4π directional sensitivity to sources. Unfortunately, neither local nor global DIMP were able to accurately locate the source leading to the conjecture that it is more difficult to locate sources against boundaries and corners due to limited measurement angles and directions. Next, three validation experiments were performed, compared to a current GGH based system, and analyzed using DIMP source prediction methods: a Cs-137 button source, a highly enriched uranium (HEU) metal calibration disk source, and a long line of HEU oxide line sources taped end to end. The original local DIMP Cs-137 button source prediction results were accurate in source location and strength

but required similar search space reductions as Hykes's original work [1]. Global DIMP determined the correct solution without search space reduction. The HEU validations revealed a discrepancy between the measured detector responses and the DENOVO (the transport solver employed by DIMP) calculated detector responses using the true source input parameters. The measured detector response values were compared to MCNP [2] models and simple analytical source approximations of the actual experimental configuration, and the modeled and analytical values were in reasonable agreement. This led to the conclusion that either an unknown source was measured, or equipment malfunction occurred during the experimental campaign. To facilitate completion of this project, synthetic data calculated by MCNP tallies was used for DIMP verification to further compare local to global DIMP performance. Similar results were obtained with the HEU synthetic data as with the Cs-137 validation. Global DIMP again was able to avoid search space reduction requirements, and both DIMP algorithms were able to locate the source with an acceptable underestimation of source strength (due to differences between DENOVO cubic source cell representations and the actual source geometry). However, both DIMP algorithms suffered from alternative solutions in the HEU line source case, which again used unshielded only detector response data. DIMP often placed weaker sources in cells a small distance away from the true location but outside of the steel pipe enclosure. In the presence of noisy detector responses, DIMP is unable to distinguish between the true strong source that is attenuated by the pipe and a weaker unattenuated source that sits outside the pipe closer to the detectors. It was surmised that this alternative solution comes from DIMP's use of the uncollided detector peak response. Use of the collided response (Compton Continuum) with a more sophisticated DRF in future versions of DIMP might eliminate at least some of the alternate solutions. Furthermore, DIMP's uncertainty in attenuated and unattenuated source determination may have further compounded noisy responses in the unshielded Hykes's case study. Finally, a sensitivity study based on randomization of detector locations in sets of 7,15, and 24 locations using realizations of either 10 (global DIMP) or 100 (local DIMP), since global DIMP runs 10 local search iterations per run. The results showed some improvement in global DIMP over the local version in minimizing weak solutions far away from the true source location, but increased source strength errors. Source strength errors were common to both DIMP methods, and sources were often buried in the wall similar to Hykes's original results. This result further illustrates DIMP's current inability to distinguish between attenuated and unattenuated sources.

Validation and Uncertainty Quantification of the Data Integration with Modeled Predictions (DIMP) Inverse Radiation Transport Model For Holdup Measurements

by
Noel Nelson

A dissertation submitted to the Graduate Faculty of
North Carolina State University
in partial fulfillment of the
requirements for the Degree of
Doctor of Philosophy

Nuclear Engineering

Raleigh, North Carolina

2018

APPROVED BY:

Ralph Smith	Louise Worrall
Yousry Azmy Co-chair of Advisory Committee	John Mattingly Co-chair of Advisory Committee

DEDICATION

In memory of my dearest and loving mother, Deanna Nelson.

BIOGRAPHY

The author was born in a small town in Oregon called John Day, to parents R. Bryan and Deanna Nelson as the youngest of two children. He graduated from Grant Union High School as the Valedictorian in 2008. He continued his studies at Oregon State University (OSU) for four years in Nuclear Engineering.

At OSU he worked diligently beside his studies as a cook for the university dormitory kitchens and as an undergraduate researcher for the chemistry department. In his chemistry research, he observed the effects of electric voltage, frequency, and amperage on the polymer brush growth of hemoglobin for use in the manufacture of prosthetics. He graduated Summa Cum Laude from Oregon State with an Honors B.S. in nuclear engineering in the summer of 2012.

He continued his graduate studies at North Carolina State University under the direction of Dr. Yousry Azmy. His research includes inverse holdup source characterization methods, and detector response validation and uncertainty quantification.

ACKNOWLEDGEMENTS

We thank the Nuclear Energy Universities Program (NEUP) for its financial support of the initial project, and the Consortium of Nonproliferation Enabling Capabilities (CNEC) for its continued financial support.

We also thank the National Nuclear Security Administration (NNSA) Graduate Fellowship Program and the NNSA Production Office (NPO) for their support in the last year and a half of the project.

We acknowledge Oak Ridge National Laboratory (ORNL) for the use for the Safeguards Laboratory facility, equipment, and materials.

TABLE OF CONTENTS

LIST OF TABLES

LIST OF FIGURES

CHAPTER

1

INTRODUCTION

1.1 Research Motivation and Goals

The goal of this work is to validate the Data Integration with Modeled Predictions (DIMP) inverse particle transport method for solving the special nuclear material (SNM) holdup problem. Holdup problems arise when radioactive material becomes trapped in processing equipment at nuclear fuel processing facilities. Examples of processing equipment can include but are not limited to pipes, ducts and filters, glove boxes, and valves. [3] SNM holdup is of interest to the nuclear fuel industry for many reasons. These reasons include: criticality safety, maintaining accurate SNM inventory and nuclear safeguards regime, and radiation worker safety.

Criticality safety is important because if enough nuclear material buildup occurs over time in a section of equipment, it can present a criticality risk. Even if the holdup deposit geometry is not at risk of becoming critical, accumulation of radioactive materials can pose a radiation hazard to facility employees who may become exposed to the resulting radiation field while working in the vicinity of the held up material. Finally, SNM is important to track for economic purposes and to ensure nonproliferation transparency. All fissile nuclear material must be accounted for within reasonable margins to verify that it is exclusively used for the peaceful purposes of the facility's operations under applicable international safeguard protocols and treaties.

Therefore, holdup sources are important to quantify in total material mass, isotopic composition, as well as distribution and location. There are several models to choose from in order to solve the

holdup problem. The most common model used in industry is called the Generalized Geometry Holdup (GGH) model. [3] The GGH model is based on a set of core assumptions. All sources in the model must be approximated as a point, line, or area source. The source type is chosen based on the measurements and judgements of a holdup survey crew. They use handheld field detectors (often simple Geiger counters) to measure the approximate distribution of the source in a piece of equipment. After determining the relative size, shape, and location of a source, measurement points are determined, and another survey crew will take spectral measurements of the source with gamma-ray detectors (generally NaI or CdZnTe). The GGH model is then employed based on one of the three GGH source distributions using background correction models and a self-attenuation factor to calculate the approximate amount of radiation source material present in grams. [3] This model can have a high degree of uncertainty and requires a large amount of measured data and application of user judgement.

The DIMP method, in contrast, seeks a more automated system by posing the holdup configuration as an inverse problem. Initial survey crews would not be required, and few assumptions are necessary to predict source distribution, size, strength, and location within equipment. DIMP uses an adjoint particle transport model to calculate an importance map for a grid of detectors in the target geometric configuration utilizing as-built information of dimensions and material composition of the facility's structure. Deterministic transport codes are capable of modeling such configurations with a varying degree of fidelity of the models to achieve a desirable computational precision. Together, the computed flux and detector response function can be used to predict detector responses from a given source distribution. Alternatively, and more efficiently in the present case, folding the importance function with a given source distribution yields an estimate of the detector response where the importance function is the adjoint flux computed with an adjoint source set to that detector's response function. DIMP calculates the optimal source distribution(s), location(s), and strength(s) that best match calculated responses to experimental responses with no presumptions of the source shape and minimal logical restrictions on its physical location, e.g. a source cannot be hanging in the air in the middle of a room.

Currently, the DIMP model has been validated for a Cs-137 point source and a Co-60 line source. [1] It performed well with low error that was mostly attributed to the weakness of the available sources (older button sources). [1] The original plan for this work intended to expand upon the model and previous research with realistic holdup experiments using strong Uranium sources measured with a field holdup NaI detector, and compare the results to the Holdup Measurement System (HMS-4), a GGH model. [4] Four experimental holdup measurement campaigns were performed in this work including a Cs-137 point source, a highly enriched Uranium (HEU) disk source, an HEU line source in a pipe, and a set of HEU area sources in a duct. While these measurements were completed successfully, their utility in validating DIMP was undermined by their incompatibility with the applicable radiation transport models employed by DIMP. This discrepancy is elaborated

below, as reason for completing the DIMP verification exercise using synthetic MCNP responses.

1.2 Summary of Results

First, numerical studies were performed that showed the stability of DIMP and helped to quantify uncertainty in the detector location parameter. DIMP converges consistently to reasonable source distribution predictions with an increasing number of detector locations. Unfortunately, both local and global DIMP struggled to accurately predict the Cs-137 point source distribution in the corner of a room from Hykes's [1] case using purely ushielded responses. Two logical reasons were surmised to explain the inaccuracy. First, DIMP may perform poorly due to limited directional information obtained from the small range of measurement angles permitted in situations where the source is against a boundary or in a corner. Second, DIMP cannot distinguish between attenuated and unattenuated sources, since it relies solely on the peak detector response. Continuum response information based on particle scattering may provide more information about sources near objects and boundaries.

Next, a detector location based sensitivity study was performed with DIMP. The source distribution predictions tended to produce clusters around three types of solutions: the correct solution (1x the source strength and close to the true source location), high distance from the true solution but generally weak source (typically close to a detector grouping), or low distance but high intensity (meaning it was buried in a wall or in the floor). The wall solution is a problem common to the overall method attributed to using the peak uncollided detector response as the measurement vector.

This alternative solution was obtained in all of the holdup validation exercises where a source was contained within a steel enclosure. DIMP cannot distinguish between solutions that are attenuated within the object and solutions that are weaker and located immediately outside the object. This is because DIMP has no continuum (particle scattering information). Using simple continuum collided flux models (as in Ref. [1] and Ref. [12]) proved insufficient. Better response functions need to be developed and tailored to DIMP in order to address this issue.

Only the first three source validation measurements were analyzed due to an unforeseen measurement issue. After correcting for the collimation geometry of the measurement detector in the DRF model, the Cs-137 point source was successfully predicted by both local and global DIMP. The HEU based results included local and global DIMP source predictions and were also compared to HMS-4 gram quantities. Both DIMP methods located and greatly overestimated the source due a discrepancy between the measured and calculated detector responses, while strangely HMS-4 predicted the HEU disk correctly and underestimated the HEU line source. Equipment failure or an unknown source presence affected the HEU validation measurements and produced a large discrepancy between the computed responses and the measured values. Several MCNP models were compared to the DIMP calculated fluxes and the measured responses. The discrepancy appeared to

solely afflict the measured data because models based on Monte Carlo, on Discrete Ordinates, and on simplified analytical formulations were in reasonable agreement and differed by about an order of magnitude from the measured values.

Therefore, synthetic data obtained with MCNP was used to recover and to perform a numerical validation. DIMP performed well using synthetic data with the exception of still predicting alternative lower strength sources outside of the steel enclosure in the HEU line case as detailed later in this dissertation. The result is still encouraging because the line case was also performed using purely unshielded responses, and global DIMP performed better than the earlier Hykes's case. Unshielded detectors have a higher detector efficiency, less complex DRFs, and do not require an operator to allign the detector towards a source to measure useful information.

1.3 Outline of this Document

The structure of this dissertation is as follows.

- Chapter 2 provides an overview of the literature for the underlying the DIMP method. Bayesian principles, radiation transport methods, and optimization methods for local and the improved global DIMP algorithm are discussed.
- Chapter 3 discusses the numerical studies performed with local and global DIMP. One study verifies the stability of DIMP with increasing synthetic detector information by solving Hykes's problem [1] incrementally with additional detector locations. Another analyzed its performance using purely unshielded responses only, and a third analyzed the sensitivity of source prediction to detector location.
- Chapter 4 discusses the experimental setup used in the validation and a summary of the general principles underlying the current holdup NDA code developed at ORNL, HMS-4. The experimental parameters discussed include source strength specifications and location, container and object locations and dimensions surrounding the source, and detector specification and measurement locations.
- Chapter 5 contains the numerical results and analysis of the experiments performed at ORNL using both synthetic and experimental measurements.
- The conclusions are presented in Chapter 6
- Appendix A displays the outputs from the HMS-4 system for two of the HEU validation experiments performed.

CHAPTER

2

REVIEW OF THE LITERATURE

2.1 Inverse Problems

Inverse problems are often more complex than their counterparts, the forward problem. In the forward problem, an effect is predicted from an imposed cause. For example, in the typical forward radiation transport problem, a source with an initial state and parameters (e.g. radiation source distribution in space and angle, and its energy spectrum, etc.) are known and the state of the system at other points in space and time (e.g. radiation flux, temperature, dose, etc.) are unknown. A forward model is used to calculate the solution at those points from the known source and properties of the problem domain (e.g. dimensions, material composition, nuclear data, etc.).

An inverse problem, in contrast, poses the reverse question. The cause(s) are sought from a set of measured effects, or a model is identified to connect a set of input causes to output effects. Information at various points in space and time called "measurements" are considered known, but the source state or the domain configuration that produces them is treated as unknown. An inverse model is used to calculate a possible solution state of the system from the measurements. This is where the difficulty of inverse problems arises. The existence and uniqueness of an inverse solution is typically not certain, and solutions can be very unstable depending on the quality of the measurements.

One way to approach the difficulty of inverse problems is to find solutions with probabilistic methods. While the solution that best fits the measurement data is not always the true solution, the

chance that it is the true solution should increase with increasing amount of measured data. This idea is formalized via Bayes' theorem [5]:

$$p(hypothesis|data,I) \propto p(data|hypothesis,I)p(hypothesis|I), \tag{2.1}$$

where $data$ is the experimentally measured data (e.g. detector responses), the $hypothesis$ is the unknowns of the system (source parameters in this work), and I is all the additional knowledge of the system (system geometry, detector efficiency, detector response functions, etc.). The three probability density functions (PDFs) appearing in Eq. 2.1, namely $p(hypothesis|data,I)$, $p(data|hypothesis,I)$, and $p(hypothesis|I)$ are the posterior, likelihood, and prior respectively. The prior is the conditional probability that the hypothesis occurs based only on information I. The likelihood represents the probability of measurement data occurring based on a given configuration of the unknown data (hypothesis) and the information in I. This is proportional to the posterior, or the probability of the given $hypothesis$ (source configuration) being true based on the information I and the measurement $data$.

In order to solve an inverse problem, the likelihood function is maximized thereby minimizing the error between the experimentally measured data and the results predicted by the model from an input configuration of the source parameters. The most probable source parameter values are determined by nonlinear least squares estimation. Ideally, the source configuration that produces the minimum error between the measured data and the predicted data is close to the true solution (if the measurement and model errors are sufficiently small).

2.2 NDA and GGH

Nuclear material holdup is an application of the unknown radiation source inverse problem. The typical holdup configuration comprises material containing sources of radiation that have accumulated potentially for decades as radioactive deposits in nuclear fuel processing equipment at facilities. These deposits need to be located and their mass quantified for criticality safety, radiation safety, inventory, and nonproliferation purposes. One method of achieving this goal is destructive analysis (DA). DA involves taking the piece of equipment apart or dislodging the radioactive deposit chemically by dissolution to physically examine the source. Naturally, DA is often costly and disruptive to ordinary fuel processing operations. Therefore, it is often more appealing to perform nondestructive analysis or NDA.

NDA methods seek to gather information about the fuel deposit (or radiation source) without physically or chemically altering it or the structure containing it. This is normally accomplished through the interpretation of information obtained from radiation detector response spectra. Several models have been developed for interpreting radiation measurements and solving general inverse

radiation problems including: the Monte Carlo Library Least-squares method for determining elemental composition of a target material by active source interrogation [6], a Levenberg-Marquardt nonlinear optimization of the radiation transport model for determining nuclear metal thicknesses [7], and the GGH model [3] commonly used in the nuclear fuel processing industry to quantify holdup sources.

The base model used for performance comparison of the DIMP methodology developed in this work is the GGH model, a standardized industry approach. GGH is often used in industry because of its ease of implementation and acceptable accuracy for relatively simple calculations. However, it requires a fair amount of active user interface and time, as the method requires an initial source search survey. Then after planning a case by case measurement scheme depending on the type of source discovered, the attention of a measurement crew is required to execute the measurements with portable field radiation detectors.

GGH requires a specific set of assumptions and conditions in order to accurately predict holdup source characteristics. The system based on the GGH model used in this work for direct comparison is called the Holdup Measurement System (HMS-4) [4]. HMS-4 relies on a survey crew to scan for sources inside equipment, and when found, determine their approximate spatial distribution. After the survey, measurement points are chosen based on the approximate source distribution, local area geometry, and model assumptions. Then these measurements are used to calculate the approximate mass of radioactive material contained within the holdup source.

The four core assumptions of GGH are as follows: first, the radiation detector used for measurements is shielded on the back and sides. Second, a cylindrical collimator is attached to the front of the crystal to restrict the field of view of the detector to a known solid angle. Third, the detector is properly placed such that each holdup source can be generalized to a point source, uniform line source, or uniform area source. Fourth, the distance between the detector and holdup source is known. Several correction factors are used along with these assumptions to calculate the total mass of the holdup deposit. [3]

In order to comply well with the third assumption, many measurements locations are determined by the detector's field of view. For example, in order to measure a point source, the source distribution must hold 5% or less of the detector's field of view (based on the solid angle between source and detector). A line source must cross the entire view of the detector but remain thin. An area source must occupy 95% or more of the detector's field of view. [3] Some of the measurement locations chosen in this work followed these constraints in order to serve as HMS-4 measurement points and potentially serving the purposes of response measurements for our new approach, DIMP, as well.

2.3 DIMP methodology

DIMP is a more general inverse problem solution method that requires no correction factors and that does not limit the spatial distribution of the source to a preconceived set of options. Instead, it maximizes agreement between the measurement vector $\vec{r}_m$ (responses) and the modeled responses, $\vec{r}_p$, predicted by a configuration of the model parameters, $\vec{\alpha}$

$$\vec{r}_m = R\vec{\alpha} \tag{2.2}$$

where R is the mapping operator from the model parameter input space to the response space. The solution of this problem is linear for radiation transport and has a closed form solution for the posterior means and covariances. Cacuci's Best Estimate method based on Bayesian inference is used to find the posterior solution mean and uncertainty. [8]

2.3.1 Radiation Transport

First, the model used in the inverse framework will be described in detail followed by specification of the source parameters contained in $\vec{\alpha}$, and a few notes on the measurements $\vec{r}_m$. The model for the radiation transport problem is based on the time independent linear Boltzmann Transport equation for neutral particles in non-multiplying media. [9]

$$\hat{\Omega}\cdot\vec{\nabla}\psi(\vec{x},E,\hat{\Omega})+\sigma(\vec{x},E)\psi(\vec{x},E,\hat{\Omega}) = \int dE' \int d\hat{\Omega}'\sigma_s(\vec{x};E',\hat{\Omega}'\rightarrow E,\hat{\Omega})\psi(\vec{x},E',\hat{\Omega}')+q(\vec{x},E,\hat{\Omega}), \tag{2.3}$$

where $\psi(\vec{x},E,\hat{\Omega})$ is the angular flux of particles $[particles/cm^2\text{-}s]$ defined over the spatial domain

$x \in V$, $\hat{\Omega} \in 4\pi$, $E \in (0,\infty)$,

and with explicit boundary conditions

$\psi(\vec{x},E,\hat{\Omega}) = \psi_0(\vec{x},E,\hat{\Omega})$ for $\vec{x} \in \partial V$ and $\hat{\Omega}\cdot\hat{n} < 0$.

$\hat{\Omega}$ is the unit directional vector along which particles are traveling, $\hat{n}$ is the unit vector normal to the boundary surface ∂V at the point $\vec{x}$, and $\sigma(\vec{x},E)$ the total particle interaction macroscopic cross-section $[cm^{-1}]$. Also, $\sigma_s(\vec{x};E',\hat{\Omega}'\rightarrow E,\hat{\Omega})$ is the macroscopic scattering cross-section of particles from one direction $(\hat{\Omega}')$ and energy (E') to the direction and energy range $d\hat{\Omega}'$, dE' about the direction and energy of interest $(\hat{\Omega},E)$, and $q(\vec{x},E,\hat{\Omega})$ is the external source of radiation particles in the configuration of interest [in $particles/cm^3\text{-}s$]. In DIMP the geometric configuration and material composition of all objects in the problem domain are considered known, hence the cross

sections are retrieved and calculated for nuclide mixtures by MAVRIC [13]. Next, it is useful to define the scalar flux $\phi(\vec{x},E)$ as

$$\phi(\vec{x},E)=\int_{4\pi} d\hat{\Omega}\psi(\vec{x},E,\hat{\Omega})\,. \tag{2.4}$$

Reaction rates are key components to many radiation problems, such as dose and fission rates. In this case, the reaction rate definition can be used to define a detector response, r, as

$$r(E')=\int_0^\infty dE\int_V d\vec{x}\sigma_d(\vec{x},E',E)\phi(\vec{x},E)\,, \tag{2.5}$$

where $\sigma_d(\vec{x},E',E)$ is the detector response function (DRF). There are several ways to model and define DRFs, and this will be explored further in the full dissertation. In Eq. 2.5, $\sigma_d(\vec{x},E',E)$ is the probability per unit path length that a particle at $\vec{x}$ incident with energy E registers a response in the detector's channel dedicated to energy E'. With this definition in mind, one could use the inverse of the forward transport equation, Eq. 2.3 as the mapping function for the inverse problem. However, direct inverses are often numerically unstable and computationally expensive. Equation 2.5 requires a solution of the transport equation for every potential source distribution in order to determine the corresponding $\phi(\vec{x},E)$ then compute r and compare it to the measured values. Alternatively, the problem can be reformulated using the adjoint of the transport equation [1]. The adjoint identity can be stated as

$$\langle Ap,h\rangle=\langle p,A^\dagger h\rangle, \tag{2.6}$$

where $\langle,\rangle$ denotes an inner product, A is an operator, p and h are any pair of functions in the domain of A, and $A^\dagger$ is the adjoint operator. Furthermore, in this application we define the inner product as follows

$$\langle p,h\rangle=\int_{4\pi} d\hat{\Omega}\int_0^\infty dE\int_V dV\,p(\vec{x},E,\hat{\Omega})h(\vec{x},E,\hat{\Omega})\,. \tag{2.7}$$

Now, consider the fixed source linear transport equation in operator form

$$L\psi=q, \tag{2.8}$$

where L is the transport operator (for all angular fluxes, ψ), and q is the external source. Next, take the inner product of Eq. 2.8 with the adjoint angular flux $\psi^\dagger$

$$\langle L\psi,\psi^\dagger\rangle=\langle q,\psi^\dagger\rangle\,. \tag{2.9}$$

Applying the adjoint identity (Eq. 2.6) to the above equation yields [10]

$$\langle L\psi,\zeta\rangle=\langle\psi,L^\dagger\zeta\rangle+P[\psi,\zeta]\,, \tag{2.10}$$

where ζ is an arbitrary function ($\zeta = \psi^\dagger$ in our case) and $P[\psi,\zeta]$ is the bilinear concomitant, evaluated on the external surface of volume V,

$$P[\psi,\zeta] = \int_{4\pi} d\hat{\Omega} \int_0^\infty dE \int_{\partial V} dS\hat{\Omega}\cdot\hat{n}\psi(\vec{x},E,\hat{\Omega})\zeta(\vec{x},E,\hat{\Omega})\,. \tag{2.11}$$

Substituting Eq. 2.10 into Eq. 2.9 yields

$$\langle\psi, L^\dagger\psi^\dagger\rangle = \langle q,\psi^\dagger\rangle - P[\psi,\psi^\dagger]\,. \tag{2.12}$$

Next we set the adjoint source to the detector response function, DRF, namely $q^\dagger = \sigma_d$, implying

$$L^\dagger\psi^\dagger = \sigma_d\,. \tag{2.13}$$

Substituting this relationship into Eq. 2.12 yields

$$\langle\psi,\sigma_d\rangle = \langle q,\psi^\dagger\rangle - P[\psi,\psi^\dagger]. \tag{2.14}$$

Now, applying the following vacuum boundary conditions

$$\psi(\vec{x},E,\hat{\Omega}) = 0\,;\ for\ \vec{x}\in\partial V\ and\ \hat{\Omega}\cdot\hat{n} < 0, \tag{2.15}$$

$$\psi^\dagger(\vec{x},E,\hat{\Omega}) = 0\ for\ \vec{x}\in\partial V\ and\ \hat{\Omega}\cdot\hat{n} > 0, \tag{2.16}$$

will cause the bilinear concomitant term to vanish thus producing

$$\langle\psi,\sigma_d\rangle = \langle q,\psi^\dagger\rangle. \tag{2.17}$$

Finally, recalling the reaction rate Eq. 2.5 and substituting it in Eq. 2.17 leads to

$$\vec{r}_p(E) = \int_0^\infty dE \int_V dV\phi^\dagger(\vec{x},E)q(\vec{x},E) \tag{2.18}$$

where $\phi^\dagger(\vec{x},E)$ is the adjoint scalar flux, or importance, and $\vec{r}_p(E)$ is the predicted response. The advantage of the formulation in Eq. 2.18 over the one in Eq. 2.5 is the computationally inexpensive evaluation of the former once $\phi^\dagger$ is known for a set of detectors. During the search for optimal source distribution Eq. 2.18 comprises an inner product of the precomputed adjoint fluxes and a guess of the source distribution. In contrast, Eq. 2.5 requires a full forward transport solution for every attempted source distribution. The set of discretized importance values are calculated by the discrete ordinates package DENOVO [13], and folded with the predicted source distribution ($q(\vec{x},E)$) during the search for the best match between the resulting responses and the measurement

responses $\vec{r}_m$. The optimal source distribution is found through an optimization process that if successfully converged, yields $\vec{r}_p(E) \cong \vec{r}_m(E)$, and in this case we call the corresponding $q(\vec{x}, E)$ a solution to the inverse problem.

Currently, only the peak responses are compared for both predicted and measured responses. A full response comparison was attempted in previous work [1] including the continuum and peak responses, but the continuum response was very difficult to calculate. Accurate representation of the continuum response requires a fairly sophisticated DRF. Some research has been invested in the area of DRFs for unshielded detectors [11], but more development of the DRF is required to apply it to collimated detector responses as shown in Ref. [12].

2.3.2 Local Nonlinear Optimization

In order to optimize the predicted source distribution, the posterior probability is maximized by minimizing the residual ($Q(\vec{z})$) of the difference vector ($\vec{z}$) which contains the absolute differences in the model parameters from the initial guess and those between the measured and predicted responses. The optimization method implemented in this work is the gradient based Quasi-Newton method with the best estimate covariance as described in Ref. [8]. The method works by minimizing $Q(\vec{z})$ according to nonlinear least squares using the following Newton update step for the k^{th} iteration

$$\vec{\alpha}_{k+1} = \vec{\alpha}_k - \lambda_k \left(\nabla_\alpha^2 Q(\vec{z}_k) \right)^{-1} \vec{\nabla}_\alpha Q(\vec{z}_k). \tag{2.19}$$

where $\lambda_k \in [0,1]$ is the line search parameter which controls the search step size. α_k is the source spatial distribution written in vector form (model parameters) for all peak energies at iteration k, and α_0 is the priori or initial guess. The gradient of Q is

$$\vec{\nabla}_\alpha Q(\vec{z}) = C_\alpha^{-1} \vec{z}_\alpha + S^T C_m^{-1} \vec{z}_r \tag{2.20}$$

where C_α, C_m, and S are the source distribution and measurement covariance matrices, and the collective matrix of adjoint sensitivies ($\phi^\dagger(E)$), respectively as defined in Ref. [10]. Under the Gauss-Newton approximation, the Hessian is defined as

$$\nabla_\alpha^2 Q(\vec{z}) \approx C_\alpha^{-1} + S^T C_m^{-1} S \tag{2.21}$$

where the inverses of the covariance matrices are replaced by the appropriate linear systems of equations (consult Ref. [10]) and solved for efficiently using standard linear methods (e.g. Gaussian Partial Pivoting). Finally, the functional of the difference vector, $Q(\vec{z})$ is then defined as

$$Q(\vec{z}) = \vec{z}^T C^{-1} \vec{z}, \tag{2.22}$$

and the inverse of the covariance, C^{-1}, is

$$C^{-1} = \begin{bmatrix} C_\alpha^{-1} & 0 \\ 0 & C_m^{-1} \end{bmatrix}. \tag{2.23}$$

The difference vector, $\vec{z}$ is

$$\vec{z} \equiv \begin{bmatrix} \vec{\alpha} - \vec{\alpha}^0 \\ \vec{r}_p - \vec{r}_m \end{bmatrix} = \begin{bmatrix} \vec{z}_\alpha \\ \vec{z}_r \end{bmatrix} \tag{2.24}$$

where $\vec{r}_p$ is the response calculated with the attempted source distribution and $\vec{r}_m$ is the measured response.

2.3.3 Global Nonlinear Optimization

The gradient based Quasi-Newton method is useful for taking the shortest path to a local minimum solution for problems with many variables, i.e. with many degrees of freedom; however, there is no guarantee that the optimal state achieved is the global minimum. To improve DIMP's chances of finding the global minimum, the basin-hopping method [14] [15] was incorporated in addition to the original Quasi-Newton local search.

The basin-hopping method randomly perturbs the coordinates of the local minimum and then reapplies the local search optimization method to find a potentially new local minimum. Finally, the algorithm determines the fitness of one local minimum over the other according to Metropolis-Hastings [16] (MH) principles. For example, new local minimum candidates are accepted probability $\beta = min(1, r)$ where r is the ratio of their likelihoods, L

$$r(q^*|q^{k-1}) = \frac{L(q^*|v)\alpha_0^* J(q^{k-1}|q^*)}{L(v|q^{k-1})\alpha_0^{k-1} J(q*|q^{k-1})}, \tag{2.25}$$

where

$$J(q^*|q^{k-1}) = \frac{1}{\pi[1+(q^*)^2]}, \tag{2.26}$$

$$L(v|q) = \frac{1}{(2\pi\sigma^2)^{n/2}} e^{-\sum_{i=1}^{n}[v_i - f_i(q)]^2}. \tag{2.27}$$

α_0^* is the perturbed priori of the candidate local minimum (q^*) and α_0^{k-1} is the priori of the is the previous minimum (q^{k-1}) for k=1,m iterations. σ^2 is the measured variance, $v_i - f_i(q)$ is the error between measurements and the model evaluated at q, and n is the total number of measurements. Minima that have a lower sum of square errors have a higher probability of being accepted. Thus, out of a cluster of local minima in the solution space, the solution with minimal error is likely to be selected by the global optimizer.

A search governed by pure MH probability would only accept a new local minimum during the

global search if the sum of the square errors was reduced (or a negative, downward gradient direction was chosen) relative to the previous minimum found. In order to allow the search more freedom to wander between wide local minima wells, the Monte Carlo acceptance criterion is modified by a temperature parameter in the basin-hopping method in a way analogous to simulated annealing [17].

$$h(\Delta r) \approx exp(-\Delta r / T) \tag{2.28}$$

where Δr is the response function gradient to be minimized and $h(\Delta r)$ is the modified Monte Carlo acceptance probability. In other words, the modified MH likelihood for the basin-hopping method can be represented by Equation 2.29

$$L'(v|q) = \frac{1}{(2\pi\sigma^2)^{n/2}} e^{\frac{-\Sigma_{i=1}^{n}[v_i - f_i(q)]^2}{T}}. \tag{2.29}$$

Using a well calibrated temperature parameter, the DIMP optimizer can perturb the solution between local searches to escape local minima and select the lowest chi-squared solution from among several minima. In other words, after a local minimum (q^{k-1}) is found by a local line search optimization step at iteration $k-1$, the local minimum is perturbed and used as the new priori (α_0^*), and another local line search is performed to find the candidate minimum (q^*). If the sum of the square errors for the candidate local minimum is smaller than the sum of the square errors of the old minimum it will automatically be accepted as r will be greater than 1. If the minima is worse, it has a probability equal to r of being accepted randomly when compared against a sampled number between 0 and 1. If the candidate minima is accepted, q^* becomes q^k. Otherwise, the old minima (q^{k-1}) becomes q^k, and then another perturbation and local search step commences. All local minima (rejected or accepted) are recorded, and the minimum with the lowest chi-squared value distribution is reported after k iterations.

2.4 DIMP Structure and Outline

DIMP is a system of modules assembled from various existing, production-level computer codes where the system-level control is implemented in a Python command structure. The input to DIMP comprises all prior information such as system object dimensions, material composition and corresponding radiation interaction cross-sections, source energy information, etc., that the DIMP system overlays in a 3-D adjoint photon transport model to calculate response information for comparison with measured responses. Finally, the optimization algorithm calculates the best estimate of the source distribution from the minimization of the response error.

A general outline of DIMP's procedure is shown in Figure 2.1

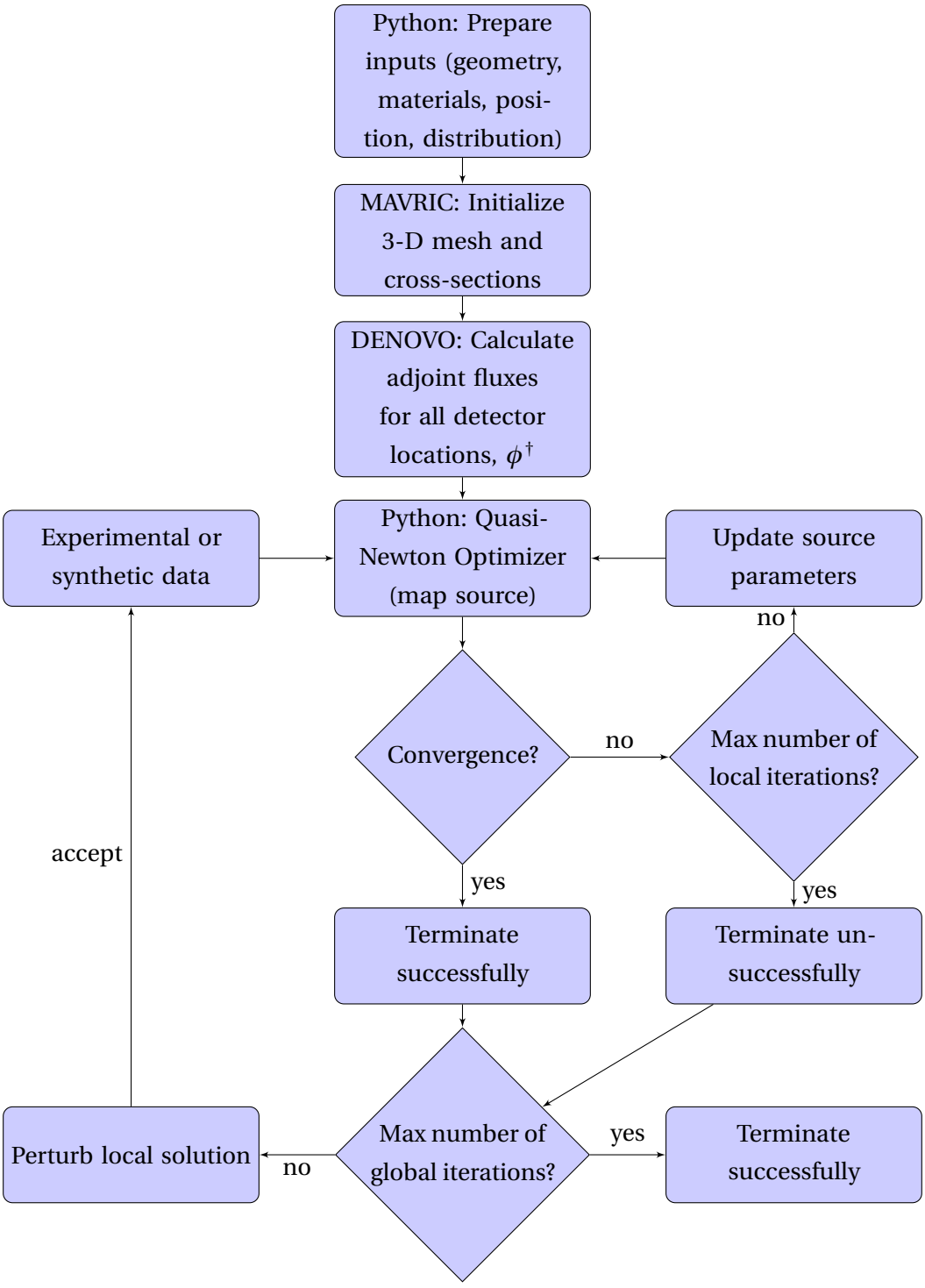

Figure 2.1 DIMP Algorithm Flowchart

First, numerous model parameters such as detector specifications, object dimensions, material

compositions, and locations, and expected source energy peak ranges are initialized as inputs by Python for use by MAVRIC. MAVRIC calculates cross-sections for all materials appearing in the problem configuration after retrieving the basic elemental cross-sections from the Evaluated Nuclear Data Files (ENDF) tables. Next, MAVRIC generates the 3-D mesh for the adjoint transport problem and passes this information along with the cross-sections to DENOVO. DENOVO calculates the importances or adjoint fluxes, $\phi^{\dagger}(E)$ in each computational cell across the entire mesh. The importances from DENOVO are then folded with an iterate of the source parameters vector, α, yielding the set of detector responses that correspond to that particular source distribution. These are passed to the Python based gradient optimizer program.

The local Quasi-Newton optimizer compares the predicted responses from DENOVO's adjoint flux to the measured responses. Measured responses are normally taken by field detector measurements, but in this proof-of-principle stage and in support of debugging activities we exercised the option of calculating synthetic responses by MCNP tallies, except in Chapter 5 where we utilize both synthetic and measured detector responses. With each iterative step, the optimizer attempts to reduce the difference between the predicted and measured responses by nonlinear least squares operations, until a local minimum in the error is found. The source distribution that has the least error is called the best estimate source distribution and is considered the solution of the inverse problem in a PDF sense. The distribution that minimizes the sum of the errors squared has the inverse property of maximizing the likelihood distribution from the original Bayes equation, Eq. 2.1. The source distribution that maximizes the likelihood distribution has the highest probability of matching the true source distribution. Note, there is no guarantee that this distribution is the global minimum; however, a good initial guess will often yield a result that is sufficiently close to the global minimum.

After the local optimizer terminates (successfully or not) the global optimizer evaluates the solution against possible perturbations of the solution until a new starting point is accepted according to Eq. 2.28. Once accepted, the basin-hopping algorithm executes another Quasi-Newton local search to find a new minimum. The process repeats until the desired number of minima are found, then the one with the lowest chi-squared value is selected as the predicted solution.

CHAPTER

3

NUMERICAL STUDIES

In order to prepare for quantifying the uncertainty introduced by changing many variables in the realistic holdup experiments conducted for the purpose of validating the DIMP methodology, numerical convergence studies were performed. In this study, a previous source configuration benchmarked in Ref. [1] (a Cs-137 point source and five Co-60 point sources arranged along a straight line) was simulated using synthetic MCNP detector responses and the results used to verify DIMP's convergence to the known source distributions while varying selected features or parameters. The choice to employ synthetic responses as opposed to experimentally measured responses is dictated by the large number of cases needed to test the desired dependencies. Also, the ability to repeat certain "experiments" either exactly or with tweaks to the setup, to facilitate debugging a certain feature of the code or limitations of the model demand such simulated measurement environments. Convergence of DIMP was measured by the accuracy of the predicted source's position, strength, and spatial distribution compared with the true source used in generating the synthetic responses. An additional measure of DIMP convergence is provided by the level of agreement of the predicted and synthetic responses as quantified by the reduced chi-squared. To test the convergence behavior, DIMP source maps over the spatial extent of the room were computed as a sequence of increasing number of detectors starting with one detector all the way up to 24 detector points. DIMP showed stable convergence towards the true point source configuration with a minimum of 5 detectors to produce a reasonable approximation of the true source configuration.

The original study that employed this setup [1] involved synthetic and experimental measurements of calibration radioisotope sources placed in room 2144 in Burlington Engineering Laboratories at North Carolina State University. A stack of Cs-137 sources was placed at one of the room's corners on the floor, and a string of five Co-60 sources were placed in a straight line on a counter in the middle of the room. The first source was meant to represent a point source and the second approximates a line source. See Ref. [10] for a detailed description and photos of the room, placement of the radiation sources, and the experimental setup.

In the original work, source maps predicted by the optimization of detector responses would often yield configurations with multiple source cells even for a single point source in the true source setup. This is because DIMP makes no prior assumptions about the spatial distribution of a source (unlike other methods such as GGH) and bases its source predictions solely on prior information (room geometry, energy of source peaks, etc.) and measured responses. So, it is quite likely in a given DIMP source map mesh that many cells will have non-zero values due, among other reasons, to noise in the measured (or synthetic) responses and numerical errors in the computational model. Therefore, a cut-off criterion is normally chosen to exclude from the solution to the inverse problem sources that are too small in magnitude and improbable (since DIMP's predicted source maps also represent a measure of the probability of a source being present).

3.1 DIMP Results and trends for a Synthetic Mono-energetic Point Source

The first test involves only a simulated Cs-137 point source considered in the original setup [1]. Synthetic responses for nine detector locations were computed with MCNP using the true source strength and location, then these responses were fed into DIMP in incremental sets to predict the optimal source distribution. The resulting DIMP-predicted source distribution is then compared to the true source distribution used in MCNP as the number of detection points was increased one by one from three to nine. DENOVO solves the inverse problem using a deterministic discrete ordinates particle transport method, whereas MCNP uses a stochastic particle transport model, so in the sense described in Ref. [10] this presents an "inverse misdemeanor" not an "inverse crime". The two codes produce non-identical numerical errors that prevent the exact true source distribution from being predicted by DIMP. Each detector point's set of simulated responses comprised one unshielded measurement and six directional measurements along positive and negative coordinate axes in three dimensions.

3.1.1 Source Map Results

DIMP source map predictions were conducted for 3-9 detector locations on solely the Cs-137 point source located at (440, 5, 1) cm with a source strength of 107.685 kBq.. The resulting source map for 3 detector locations is shown in Figure 3.1.

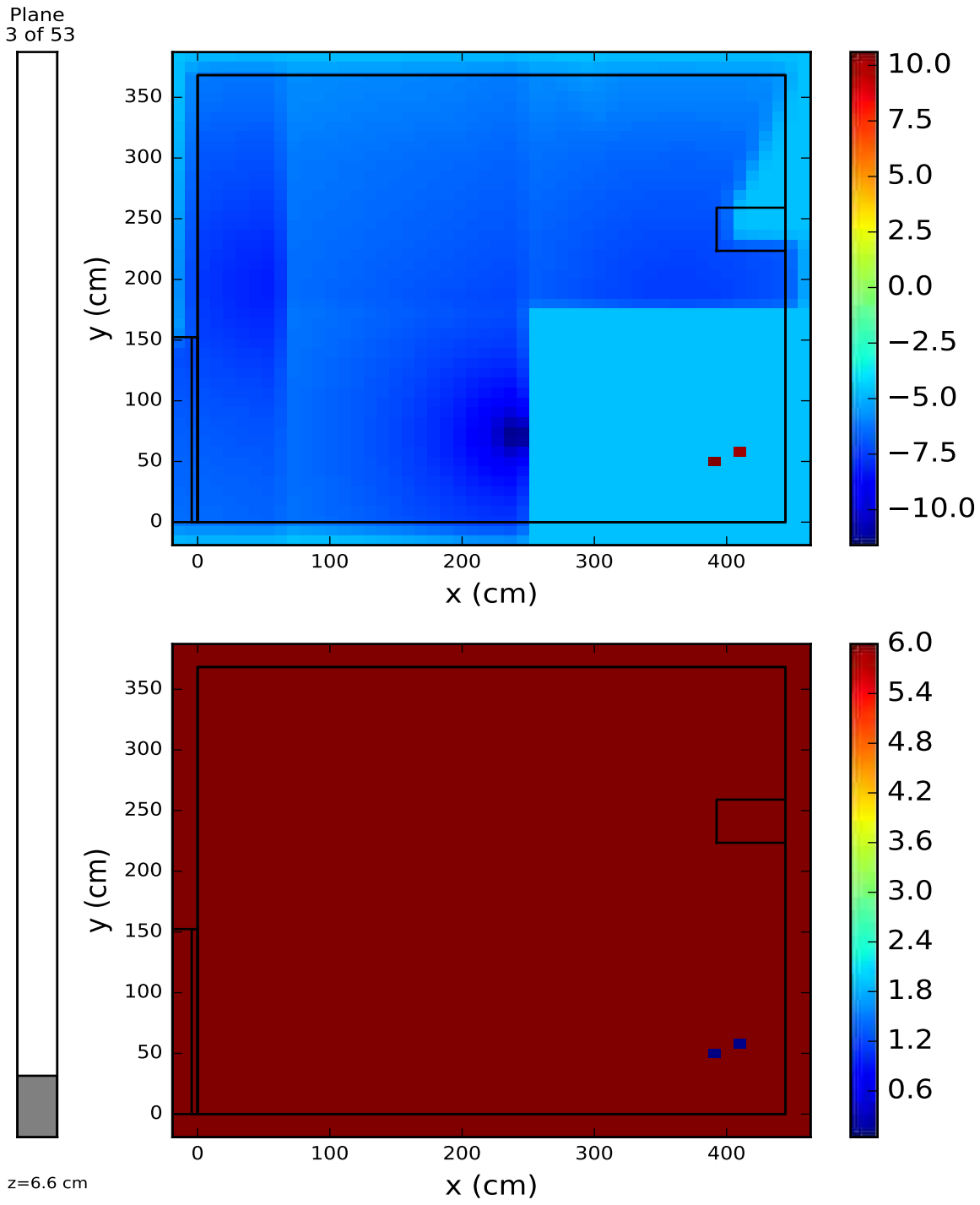

Figure 3.1 DIMP predicted source map (above) for 3 detector locations in Burlington room 2144 (search area confined to the walls) for the Cs-137 point source, and the corresponding uncertainty (below).

DIMP did not perform very well, as the predicted source cells are located (391.2, 50, 3.3; 410.5, 58.2, 3.3; and 72.6, 172, -6.2-not shown) more than half a meter away from the true source location. Collectively the sources contained only 57.6% of the true source strength and the chi-squared per detector value of 3.919E5 was quite high. It is likely that DIMP did not have enough detector response information to make an accurate prediction.

Consider the source map for 5 detector locations, Figure 3.2.

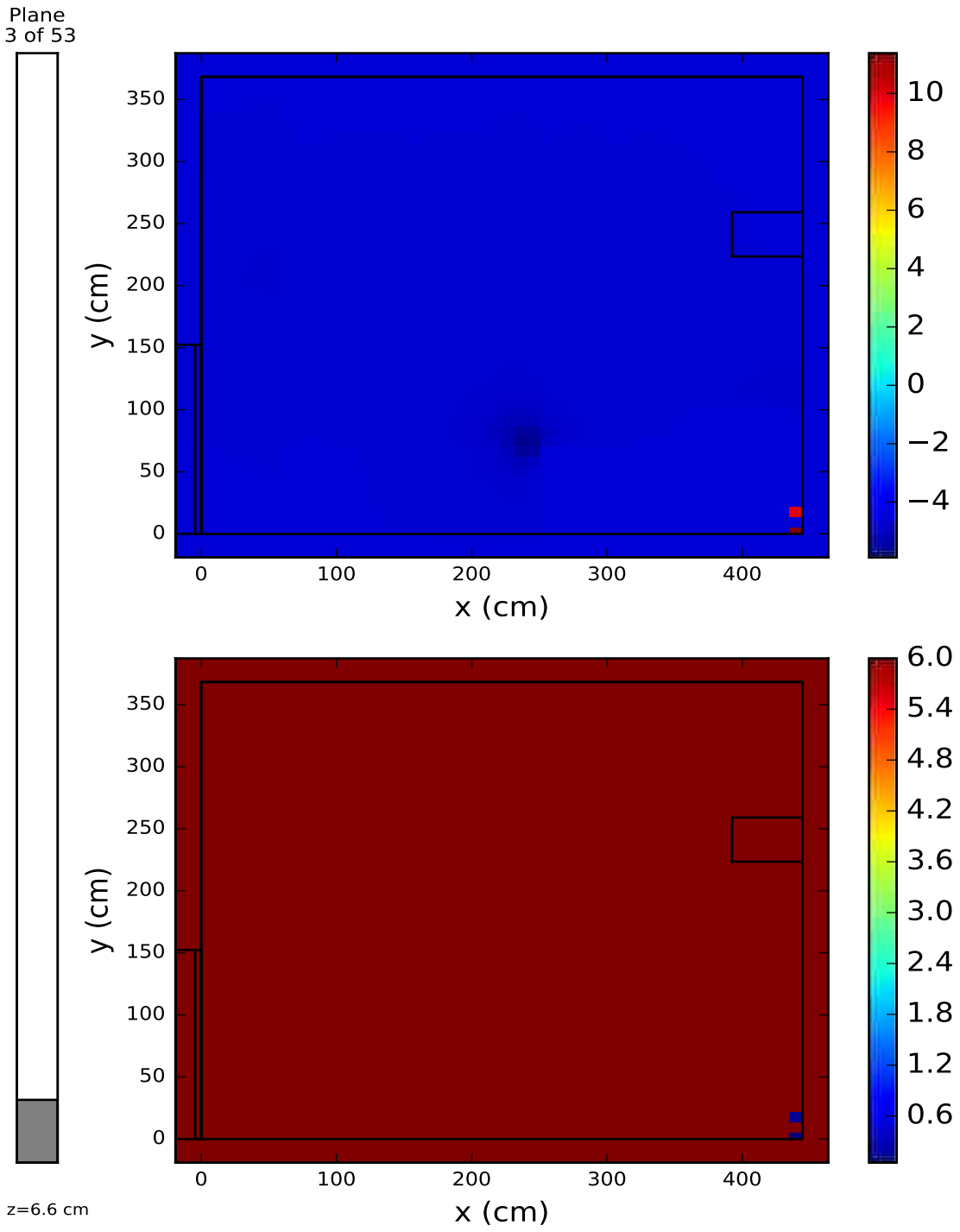

Figure 3.2 DIMP predicted source map (above) for 5 detector locations in Burlington room 2144 (search area confined to the walls) for the Cs-137 point source, and the corresponding uncertainty (below).

With only two more detector locations, DIMPs performance improves greatly. DIMP predicted two source cells at (440, 2.7, 3.3 and 440, 17.5, 3.3) collectively containing 99.9% of the true source strength and a low uncertainty. The first location is the correct cell and the second is two cells away. The chi-squared value per detector is 72.34 and much lower than the 3 detector case.

Lastly, consider the source map for 9 detector locations shown in Figure 3.3.

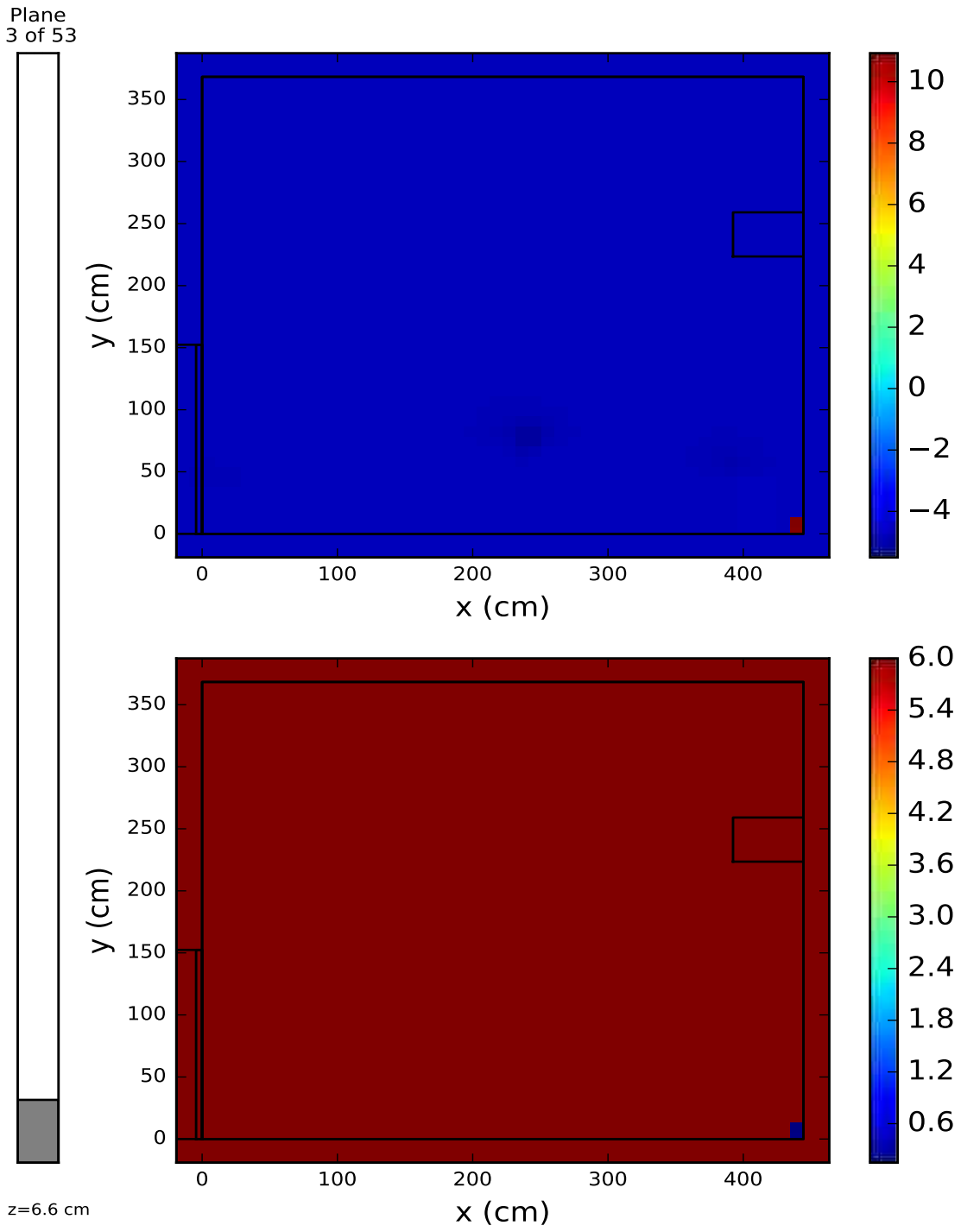

Figure 3.3 DIMP predicted source map (above) for 9 detector locations in Burlington room 2144 (search area confined to the walls) for the Cs-137 point source, and the corresponding uncertainty (below).

At 9 detectors, DIMP reaches its maximum performance for this case. DIMP predicted two source cells at (440, 2.7, 3.3 and 440, 9.4, 3.3) collectively containing 99.4% of the true source strength and a consistently low uncertainty. The chi-squared value per detector reached its lowest value of 17.78. While DIMP did not fully collect the source into the correct cell (some was in the neighboring cell to the north), it is still a very good result. Some of the values from the other detector results are shown graphically in the next section.

3.1.2 Convergence Trends

The overall convergence trends for source strength, distance from the true source location, and chi-squared value for 3-9 detector locations are displayed in Figures 3.4-3.6.

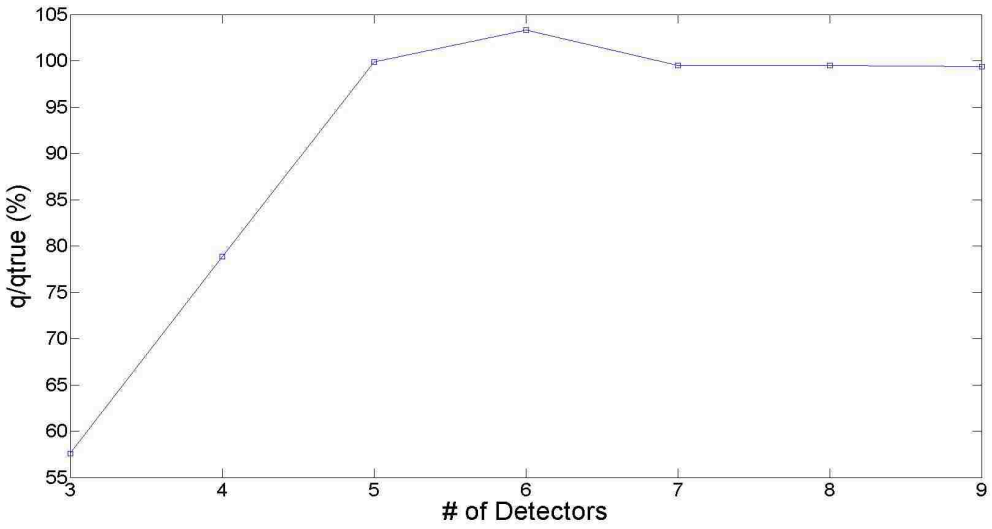

Figure 3.4 Total source strength relative to the true source strength for the Cs-137 point source using synthetic data from 3-9 detectors.

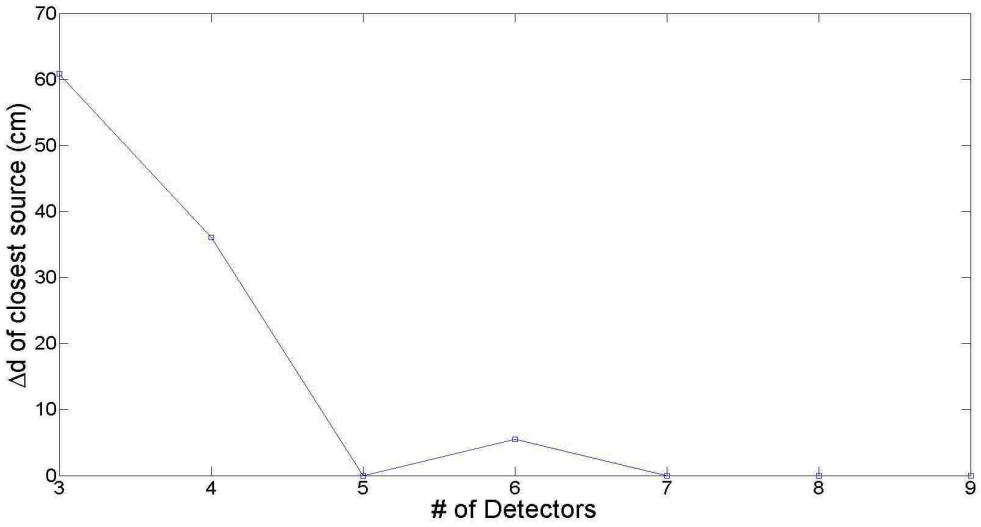

Figure 3.5 The absolute distance from the true source location of the DIMP predicted solution for the Cs-137 point source using synthetic data from 3-9 detectors. Note: Each DIMP mesh cell is approximately 5 cm x 5 cm x 5 cm.

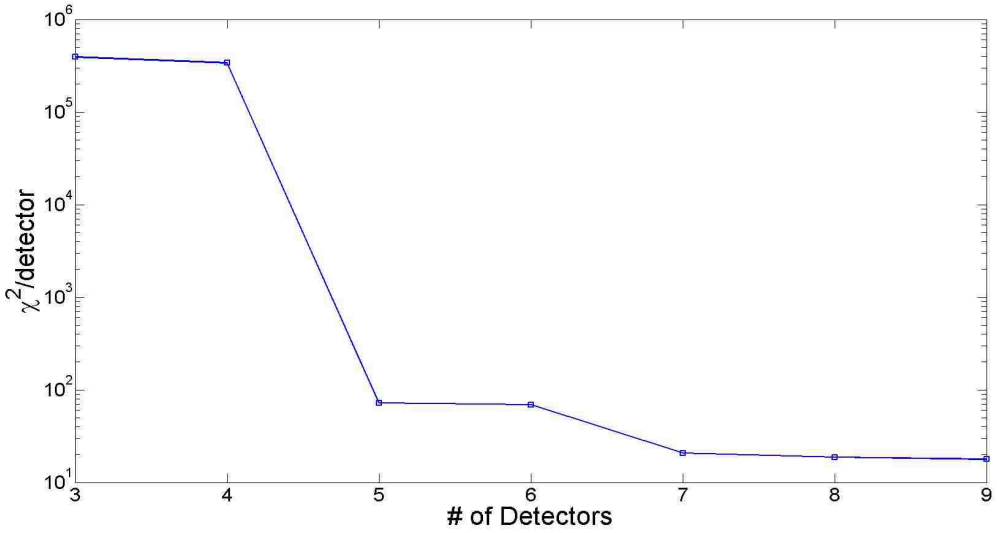

Figure 3.6 Chi-squared per detector of the DIMP predicted solution for the Cs-137 point source using synthetic data from 3-9 detectors.

Figure 3.4 shows the collective sum of all source cells in which the predicted source strength used to generate the synthetic data exceeded 1% of the true source's strength. Figure 3.5 shows the distance between the true source location (Δd) and the predicted mesh cell center of the closest source. Also shown in Figure 3.6 is the reduced chi-squared value per detector of the detector responses computed from the predicted source configuration computed via

$$\chi_R^2 = \frac{1}{\nu}\sum_{i=1}^{n}\frac{(r_{m,i}-r_{p,i})^2}{\sigma_i^2} \tag{3.1}$$

where $\nu = n-p$ is the number of degrees of freedom or the difference between the number of measurements, n, and the number of parameters, p. σ_i^2 is the variance (Poisson for experimental data or MCNP for synthetic data variance) in the measurements, $r_{m,i}$, and $r_{p,i}$ are the modeled responses. The reduced chi-squared is then further normalized per detector in order to screen out the expected modeling error between DENOVO adjoint-based responses and MCNP responses that accumulate with each additional detector. As evidenced by the large error in the predicted source locations, weak strengths, and the resulting very large chi-squared-per-detector values, DIMP does not perform adequately with fewer than 5 detectors for this source configuration. With so few detectors, the code places the source near to one of the detectors. From 5 detection points upwards to 9 detectors, DIMP converges on a 50/50 split between two very probable source cells in the corner near to where the true source is in fact located. While it does not converge to a single cell that contains the true source, it remains stable and converges to the true source cell and its neighbor as a consequence of inconsistent numerical errors in the MCNP and DENOVO models of the radiation transport process.

3.2 Synthetic Poly-energetic Multiple Point Sources Results

The second DIMP convergence test involves the full original source setup with the Cs-137 point source in the corner and the five Co-60 point sources along the center of the southern wall of Burlington Room 2144 in Hykes's problem. Again, purely synthetic measurements generated with MCNP were used as detector responses where the number of detection points was increased from 3 to 24 points total, each comprising one bare detector and six directional responses as described earlier.

3.2.1 Source Map Results

Next, DIMP source map predictions were performed for 3-24 detector locations on both the Cs-137 point source and the Co-60 line source. The true location and strength of the Cs-137 point source remains the same as stated in Sec. 3.1, while the true location of the Co-60 line source is centered at

approximately (120, 9.525, 90.17) cm. The individual x coordinates of the five point sources that compose the line source are x=96.52, 107.95, 119.38, 130.175, and 143.764 cm, and their strengths are 0.525, 2.218, 5.767, 31.793, and 3.845 kBq respectively. The distance between predicted source and the true source location was calculated for the closest source cell as the absolute distance between the true source cell's center and the predicted source cell's center. For the line source, the center cell of the line at (120, 9.4, 92.9) cm was used.

Note, DIMP treats the two coincident photons from Co-60 as independent sources with no correlation in their spatial location. Therefore, each Co source cell mapped by DIMP from one of these two energies may or may not coincide with source cells from the other energy. Also, since the Cs-137 source was analyzed separately in Section 3.1, focus will be on the Co-60 source results. Only major deviations in location or source intensity will be observed for the Cs-137 point source. The resulting source maps for 9 detector locations is shown for Cs-137 in Figure 3.7, the 1173 keV Co-60 peak in Figure 3.8 and the 1333 keV Co-60 peak in Figure 3.9

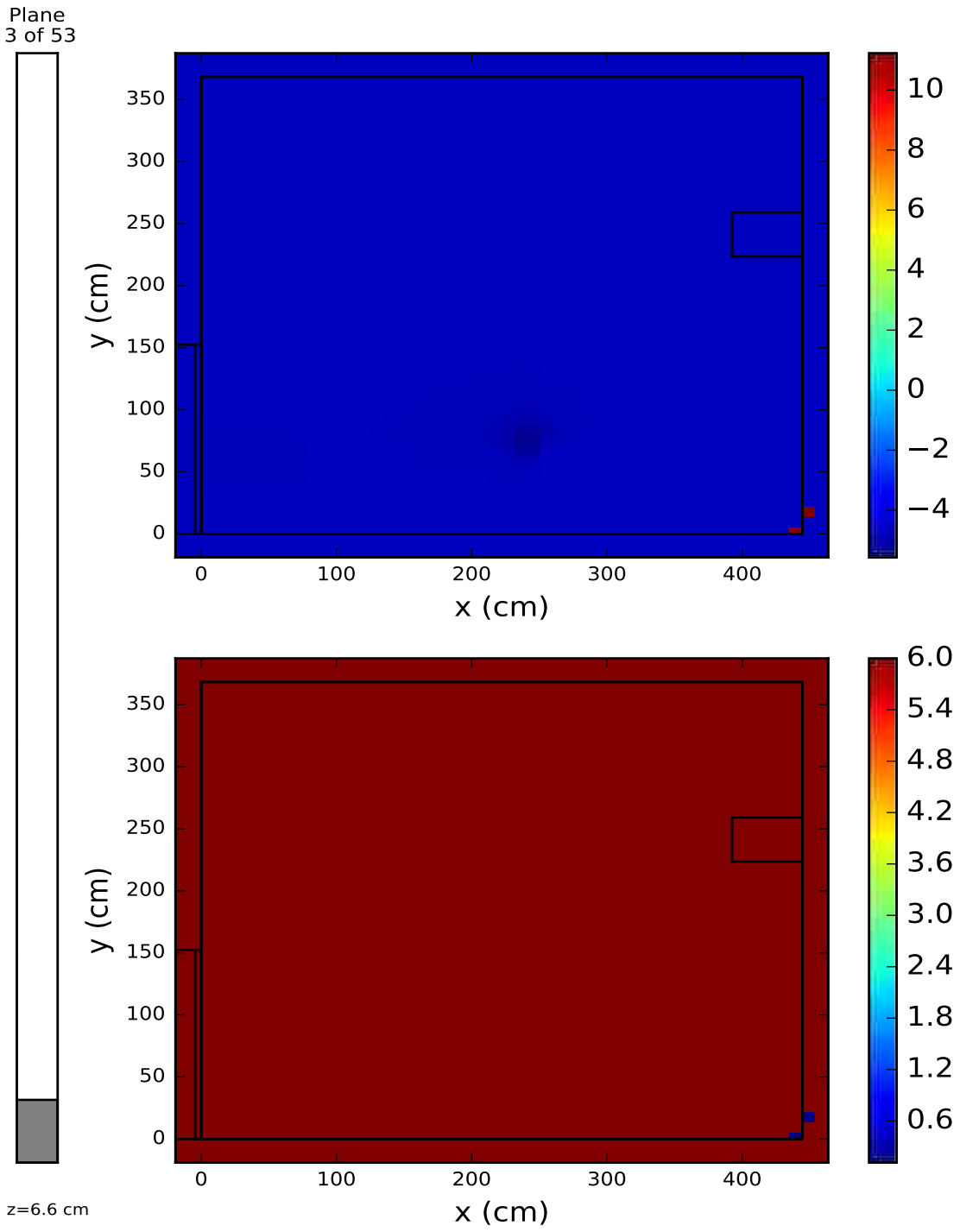

Figure 3.7 DIMP predicted source map (above) for 9 detector locations in Burlington room 2144 (search area confined to the walls) for the Cs-137 point source, and the corresponding uncertainty (below).

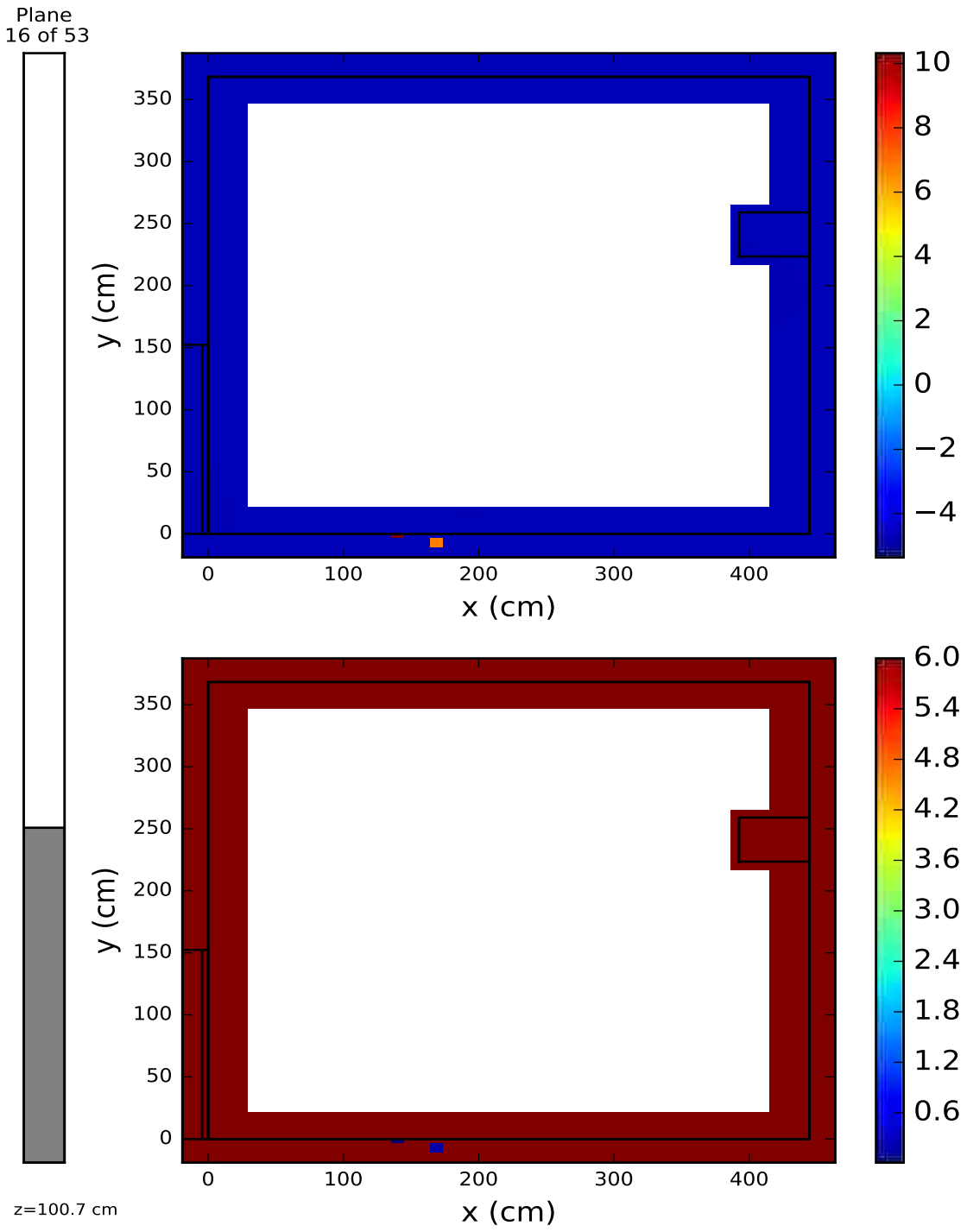

Figure 3.8 DIMP predicted source map (above) for 9 detector locations in Burlington room 2144 (search area confined to the walls) for the Co-60 line source (1173 keV peak), and the corresponding uncertainty (below).

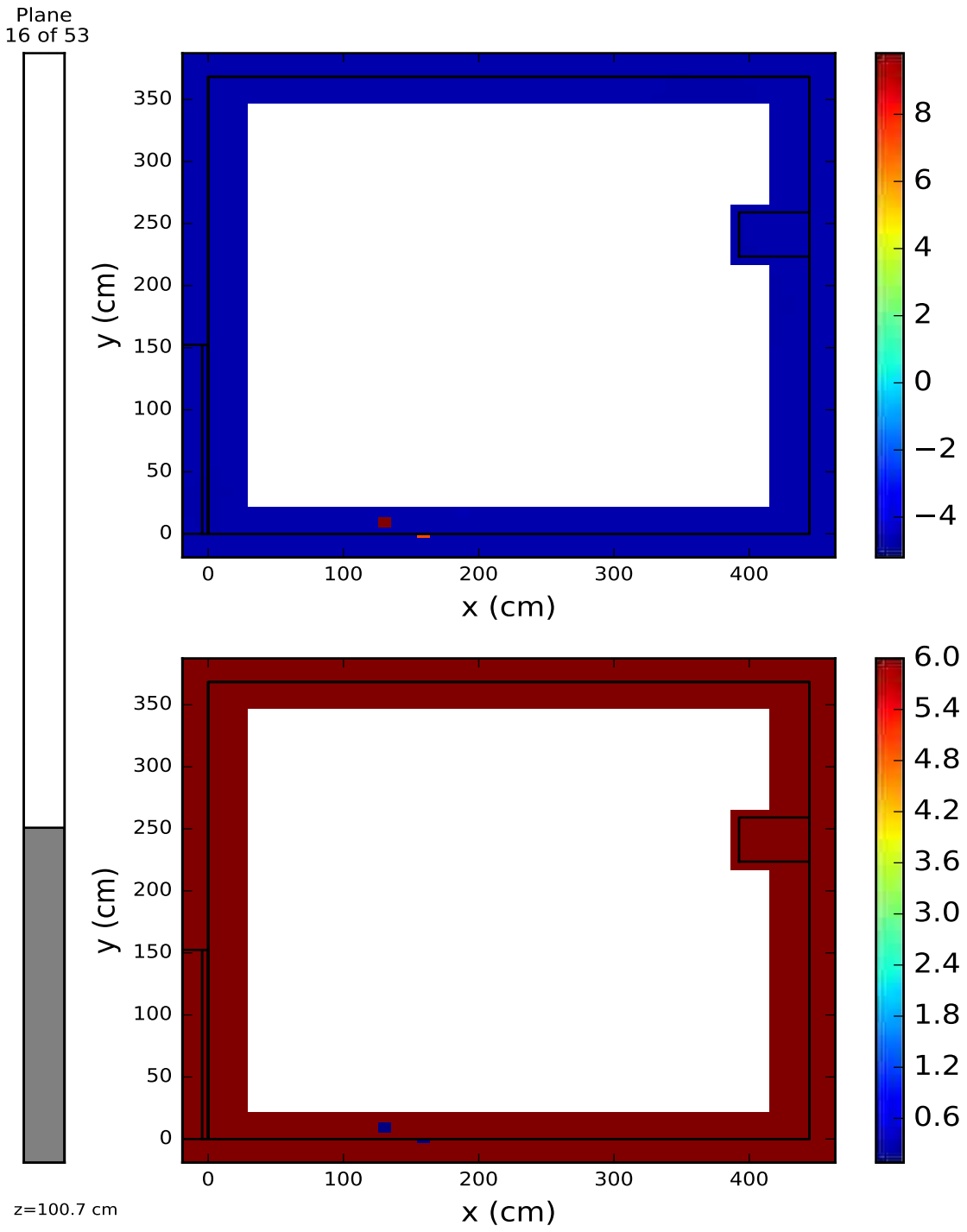

Figure 3.9 DIMP predicted source map (above) for 9 detector locations in Burlington room 2144 (search area confined to the walls) for the Co-60 source (1333 keV peak), and the corresponding uncertainty (below).

DIMP showed mediocre performance overall for 9 detectors for both sources. The Cs-137 source prediction worsened slightly (compared to Cs alone in Section 3.1.1) as one source cell strengthened slightly and shifted into the wall. The Co-60 source prediction located two source cells at (140.2, -1.4, 97.2 and 169.2, -6.9, 97.2) collectively containing 141.7% of the true source strength for the 1173 keV peak and three source cells at (130.6, 9.4, 97.2; 140.2, 9.4, 92.9-not shown; and 159.5, -1.4, 97.2) collectively containing 100.6% of the true source strength for the 1333 keV peak. The total chi-squared value per detector was 75.84. Many source strengths are larger to compensate for the attenuation of the wall, and two sources are more than 20 cm away from the true source location (one in each Co-60 energy group).

Next, consider the source maps of the Cs-137 and Co-60 sources for 15 detector locations shown in Figures 3.10-3.12.

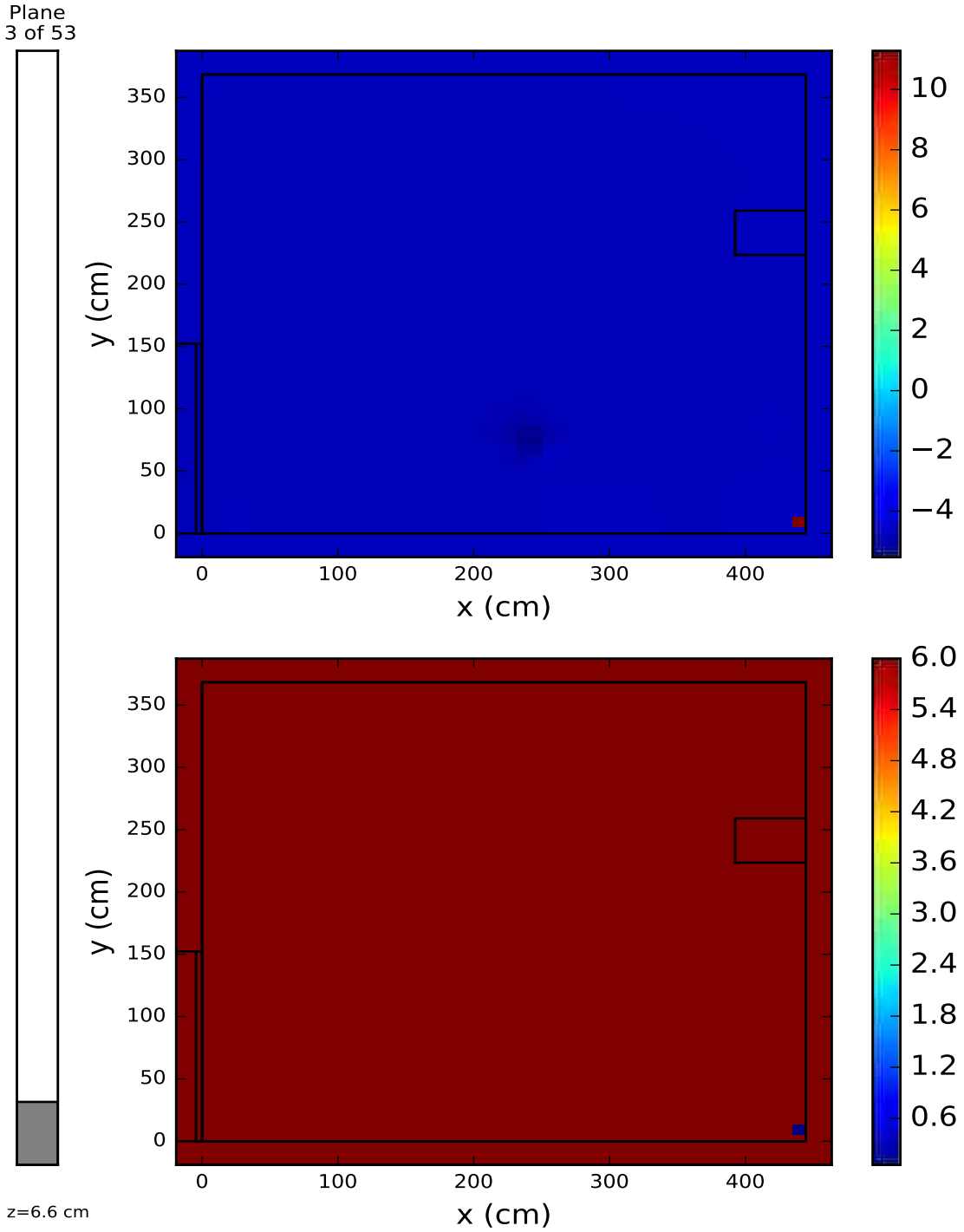

Figure 3.10 DIMP predicted source map (above) for 15 detector locations in Burlington room 2144 (search area confined to the walls) for the Cs-137 point source, and the corresponding uncertainty (below).

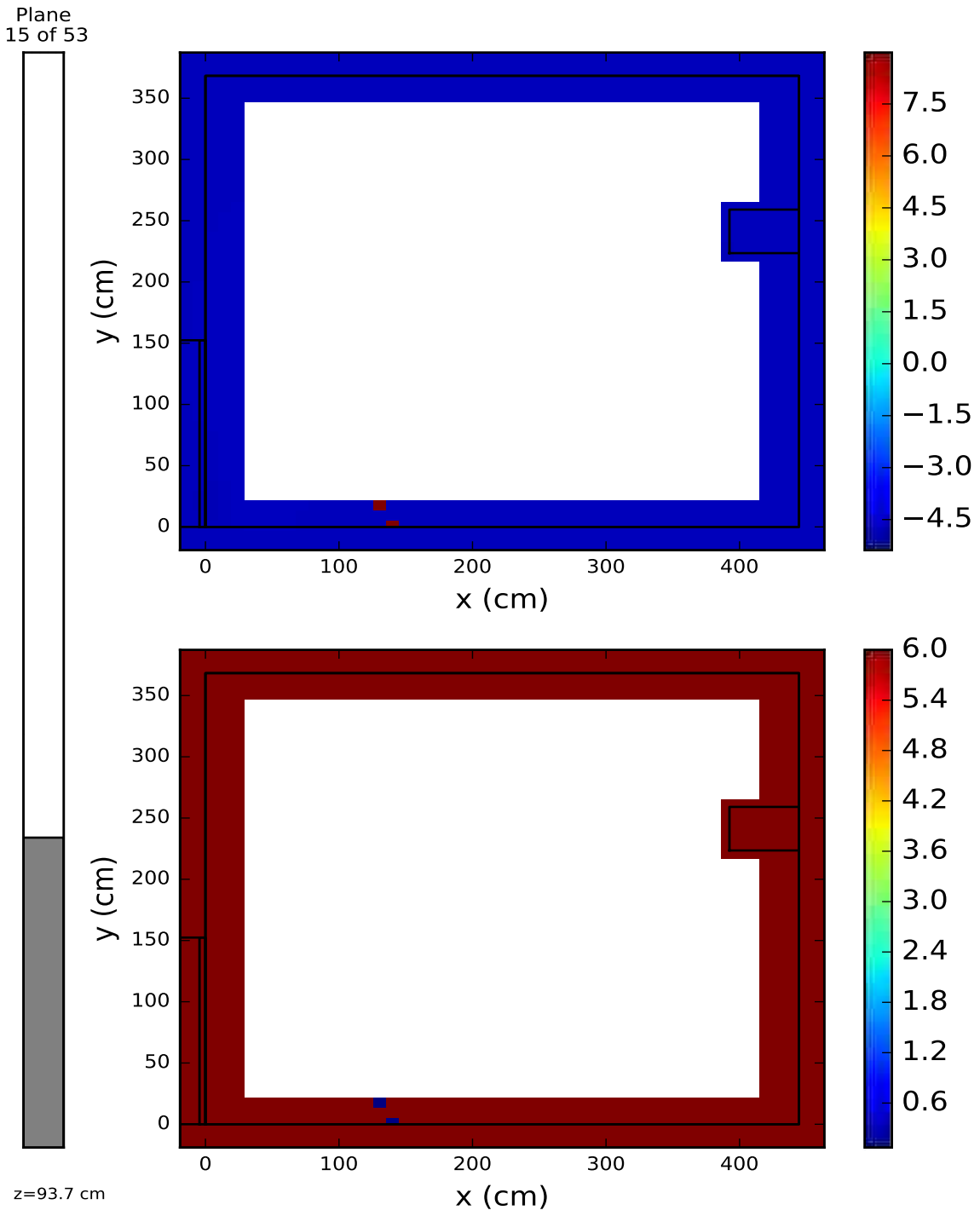

Figure 3.11 DIMP predicted source map (above) for 15 detector locations in Burlington room 2144 (search area confined to the walls) for the Co-60 line source (1173 keV peak), and the corresponding uncertainty (below).

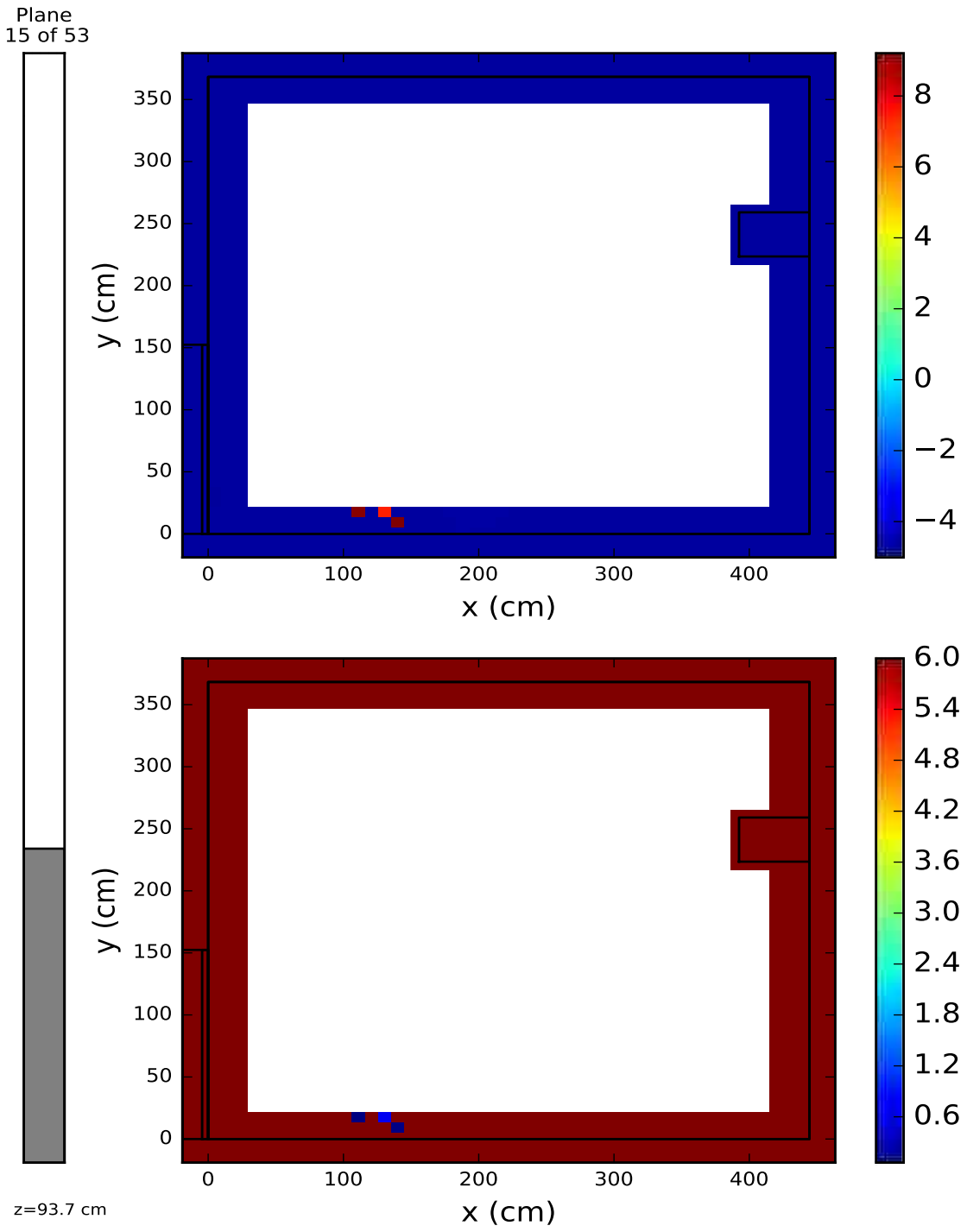

Figure 3.12 DIMP predicted source map (above) for 15 detector locations in Burlington room 2144 (search area confined to the walls) for the Co-60 source (1333 keV peak), and the corresponding uncertainty (below).

DIMP's performance improved for the 15 detector case for both sources. The Cs-137 point source stabilized back to its best prediction configuration. DIMP mapped more Co-60 source cells in the correct area with a slightly better source strength prediction. DIMP predicted source cells located at (130.5, 17.5, 92.9; 140.2, 2.7, 92.9; 101.6, 17.5, 97.2-not shown; and 140.2, 17.5, 105-not shown) collectively containing 96.6% of the true source strength for the 1173 keV peak and source cells located at (140.2, 9.4, 92.9; 111.3, 17.5, 92.9; 130.6, 17.5, 92.9; and 140.2, 17.5, 105-not shown) collectively containing 72.1% of the true source strength for the 1333 keV peak. The total chi-squared value per detector decreased to 64.60.

Finally, consider the source maps of the Cs-137 and Co-60 sources for 24 detector locations shown in Figures 3.13-3.15.

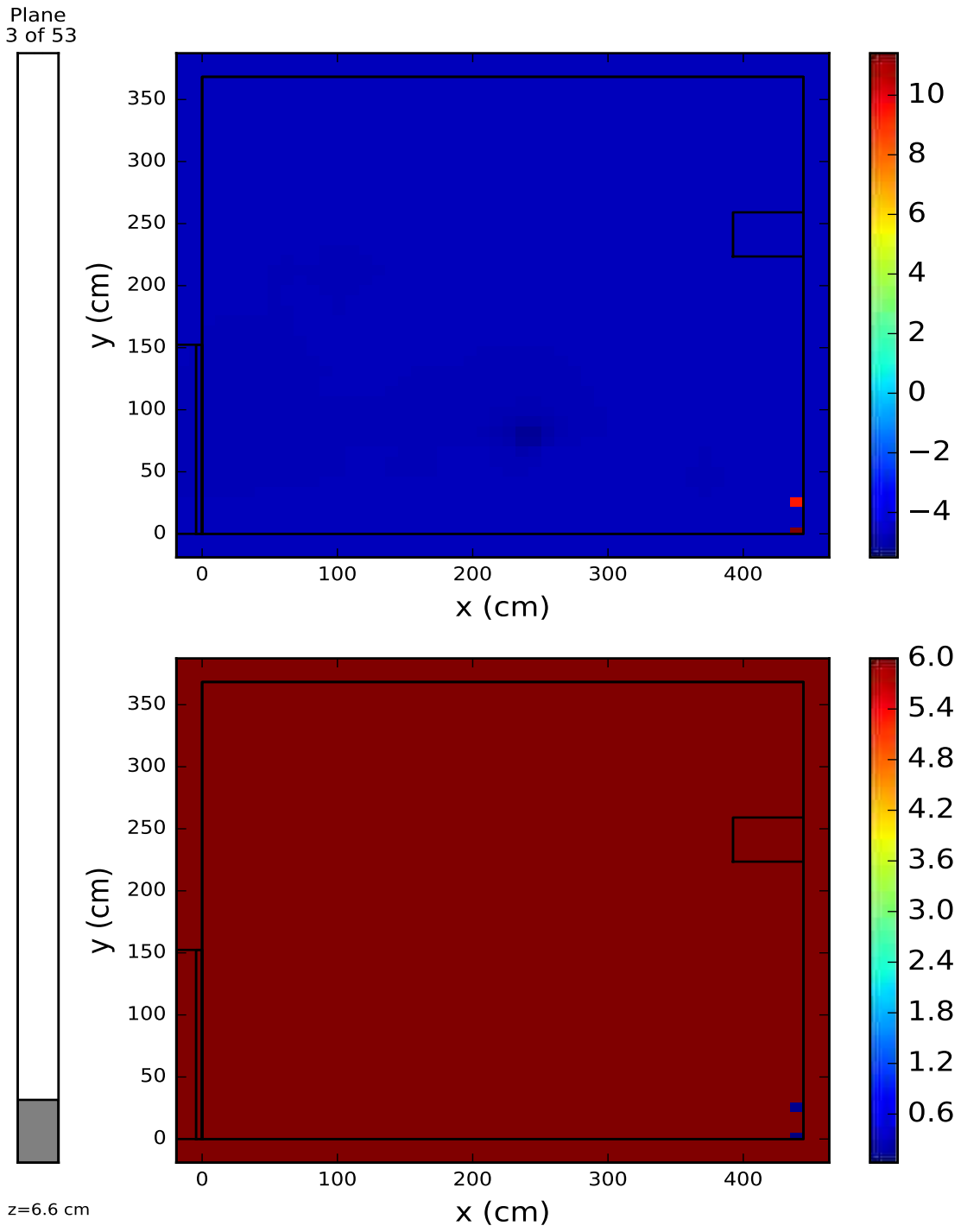

Figure 3.13 DIMP predicted source map (above) for 24 detector locations in Burlington room 2144 (search area confined to the walls) for the Cs-137 point source, and the corresponding uncertainty (below).

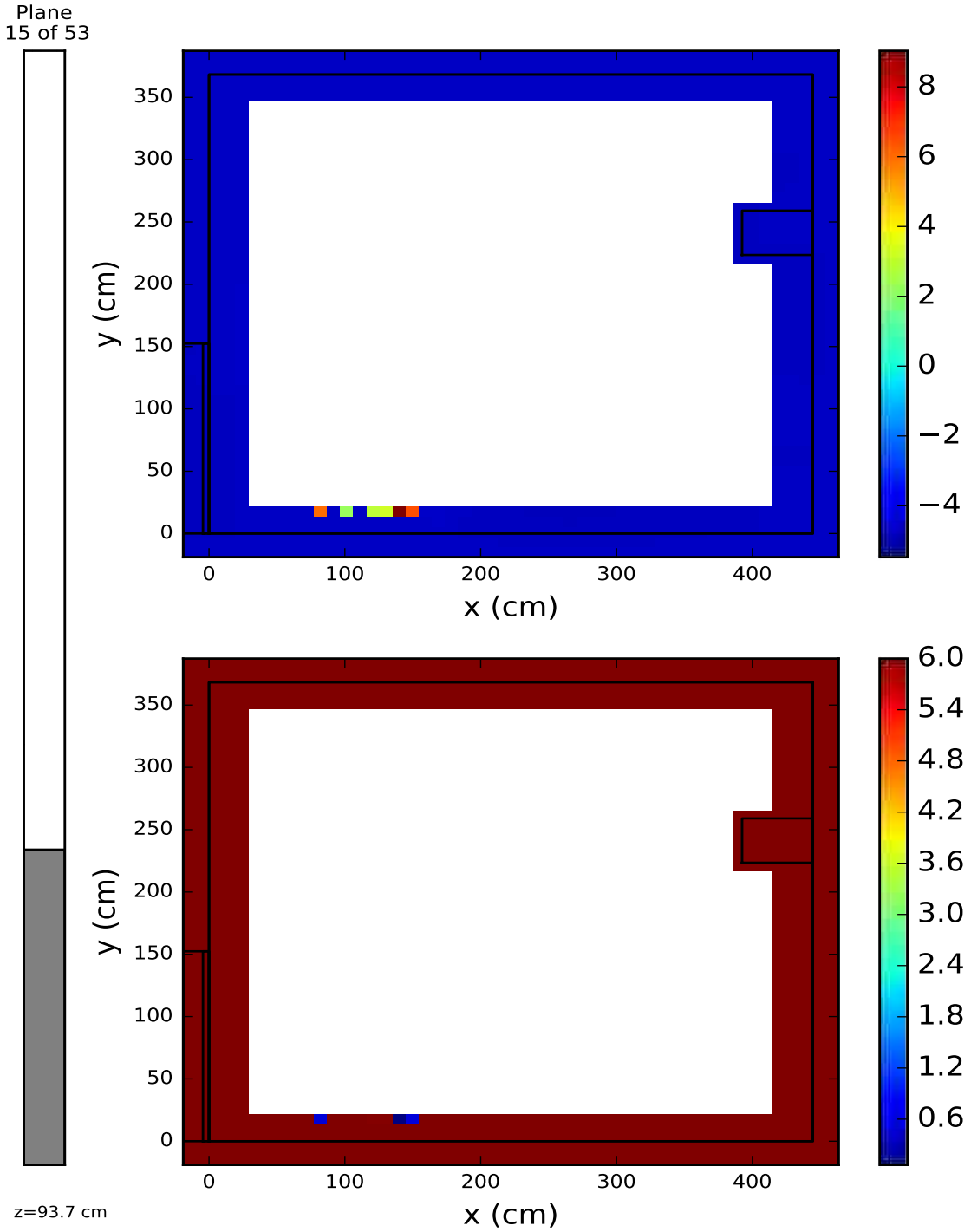

Figure 3.14 DIMP predicted source map (above) for 24 detector locations in Burlington room 2144 (search area confined to the walls) for the Co-60 line source (1173 keV peak), and the corresponding uncertainty (below).

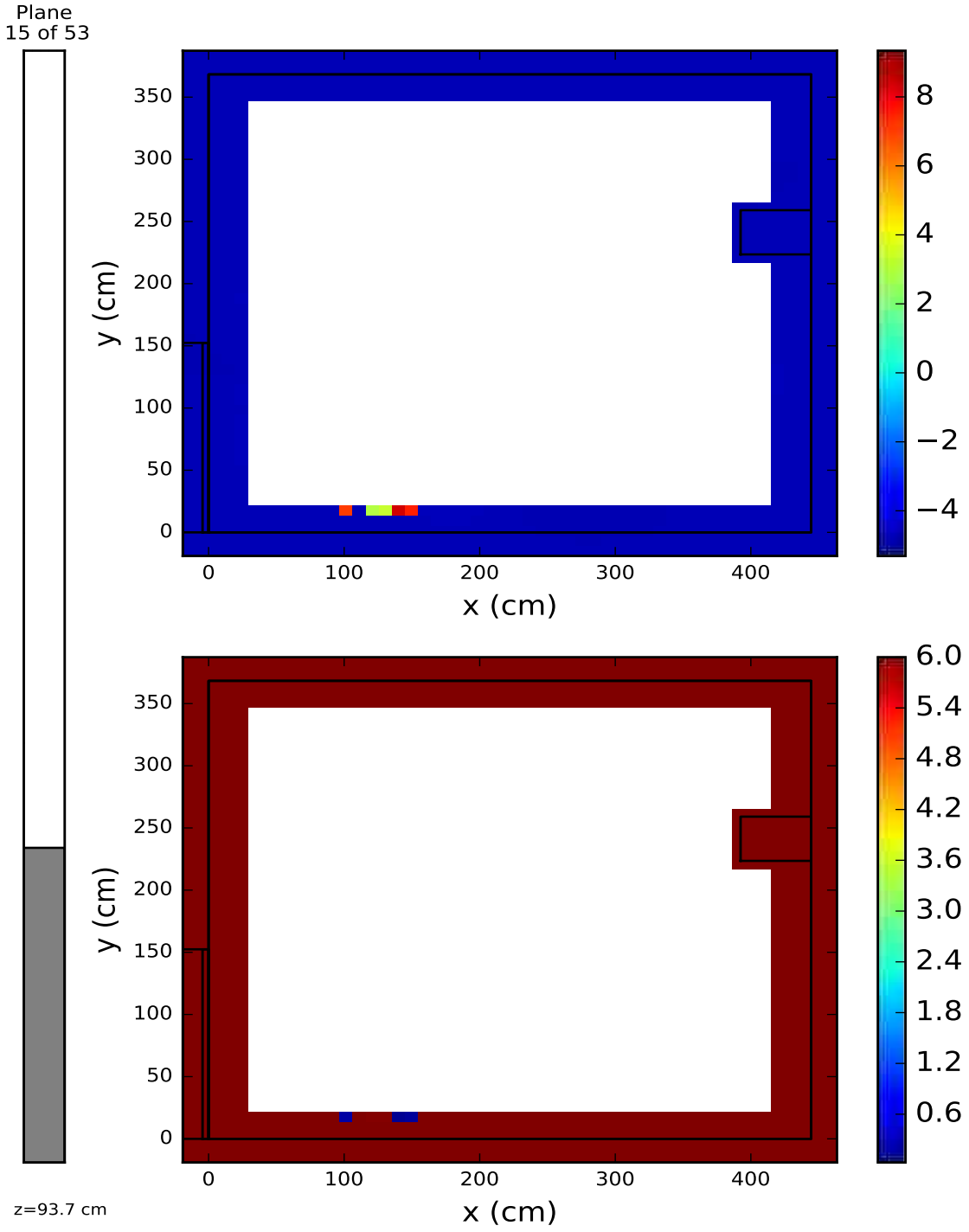

Figure 3.15 DIMP predicted source map (above) for 24 detector locations in Burlington room 2144 (search area confined to the walls) for the Co-60 source (1333 keV peak), and the corresponding uncertainty (below).

Unfortunately, DIMP's performance actually worsens for 24 detector locations due to a higher error detector response location carried over from the original Hykes's locations (further discussed in Section 3.2.2). Part of the Cs-137 source drifts slightly from the true source location, and the Co-60 locations spread apart slightly in the z-direction (upwards of 20 cm or 4 cells). DIMP predicted source cells located at (140.2, 17.5, 92.9; 120.9, 9.39, 87.9-not shown; 91.9, 17.5, 79.3-not shown; and 149.9, 17.5, 92.9) collectively containing 79.9% of the true source strength for the 1173 keV peak and source cells located at (120.9, 17.5, 87.9-not shown; 140.2, 17.6, 92.9; 149.9, 17.5, 92.9; and 101.6, 17.5, 92.9) collectively containing 86.7% of the true source strength for the 1333 keV peak. The total chi-squared value per detector actually increased to 298.8 as a result of the noisey response.

3.2.2 Convergence Trends

The overall convergence trends for chi-squared value, source strength, and distance from the true source location for 9-24 detector locations are displayed in Figures 3.16-3.18.

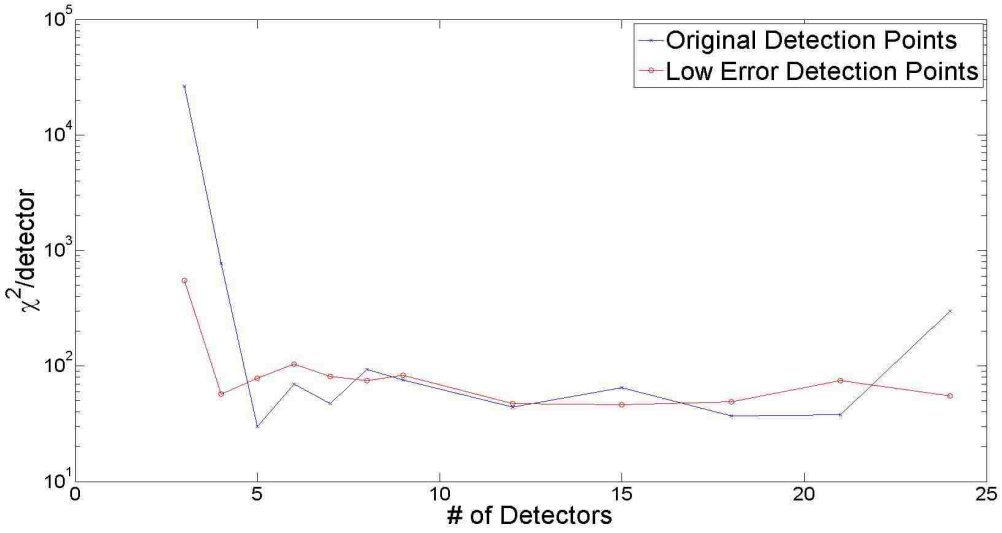

Figure 3.16 Chi-squared per detector of the DIMP predicted solution for the Cs-137 point source and Co-60 line source using synthetic data from 3-24 detectors.

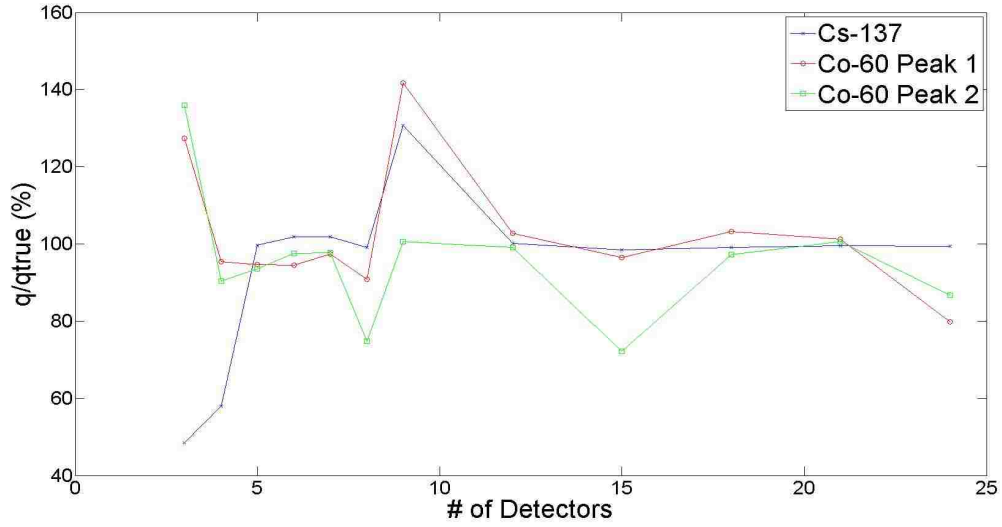

Figure 3.17 Total source strength relative to the true source strength for the Cs-137 point source and Co-60 line source using synthetic data from 3-24 detectors.

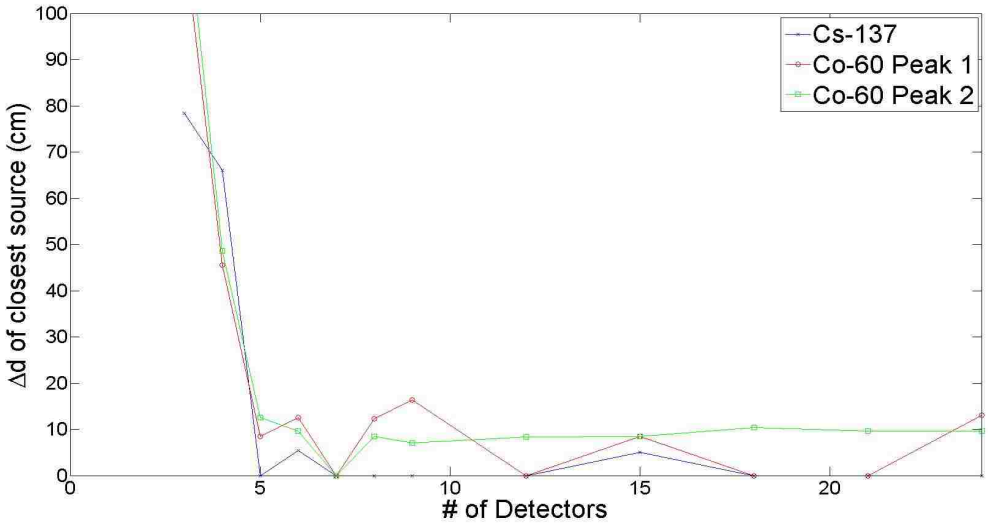

Figure 3.18 The absolute distance from the true source location of the DIMP predicted solution for the Cs-137 point source and Co-60 line source using synthetic data from 3-24 detectors. Note: Each DIMP mesh cell is approximately 5 cm x 5 cm x 5 cm.

Figures 3.16-3.18 show similar types of information as the previous convergence study, but reveal a more interesting feature. Again, DIMP does not converge with fewer than 5 detectors for this source configuration comprising a six-point distribution with three distinct energies. From 5-7 detectors the point source is well resolved, merely wavering between two configurations: a 50/50 split of the source with the correct cell and a neighboring cell and most of the source strength (>70%) concentrated in one of these two cells with the majority of the remainder present in the other cell. The Co-60 line source however, is only resolved as one- or two-cell sources. The predicted Co-60 point sources match approximately in total strength and location with the stronger sources on the true line source.

From 8-21 detectors, more points on the predicted Co-60 line source are resolved. However, DIMP never maps all five source points of the true Co-60 line source, and typically smears the locations of the stronger points on the line between the correct cell and a neighbor. Unfortunately, at 24 detectors, DIMP begins to diverge by predicting source points beyond the boundaries of the true Co-60 line source. The new detector information creates more source configurations than it eliminates as the total error between the transport model and the synthetic responses increases with the addition of each new detector. This failure was found to be the result of two detector locations that had high error responses due to being coplanar (in either x, y, or z) with the source, which causes the MCNP model to vary significantly from the value of the DENOVO responses

calculated by the point DRF (discussed further in Section 3.2.2). Removing the high error detectors yielded an improved source map result shown in Figures 3.19-3.21

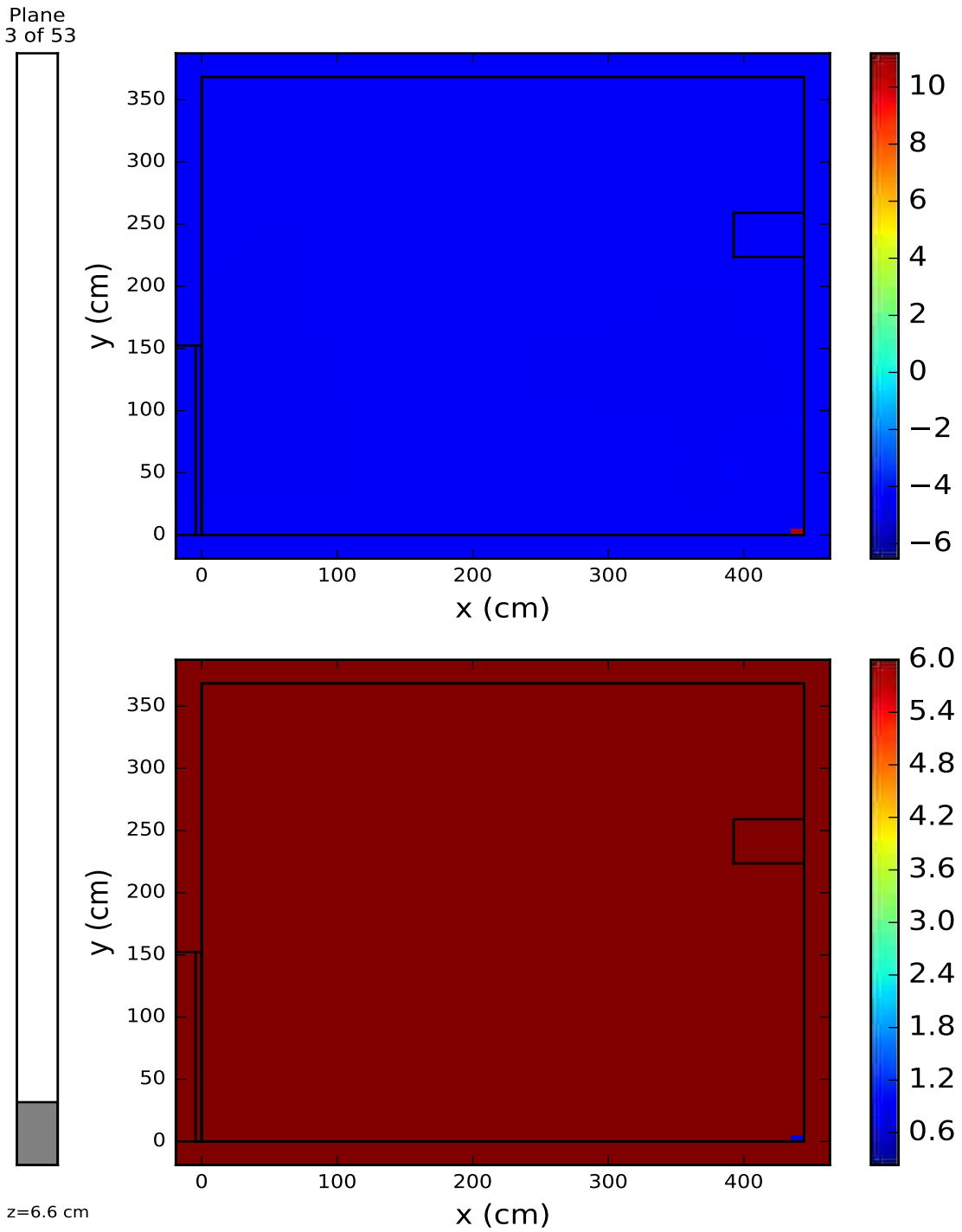

Figure 3.19 DIMP predicted source map (above) for 24 detector locations in Burlington room 2144 (search area confined to the walls) for the Cs-137 point source, and the corresponding uncertainty (below).

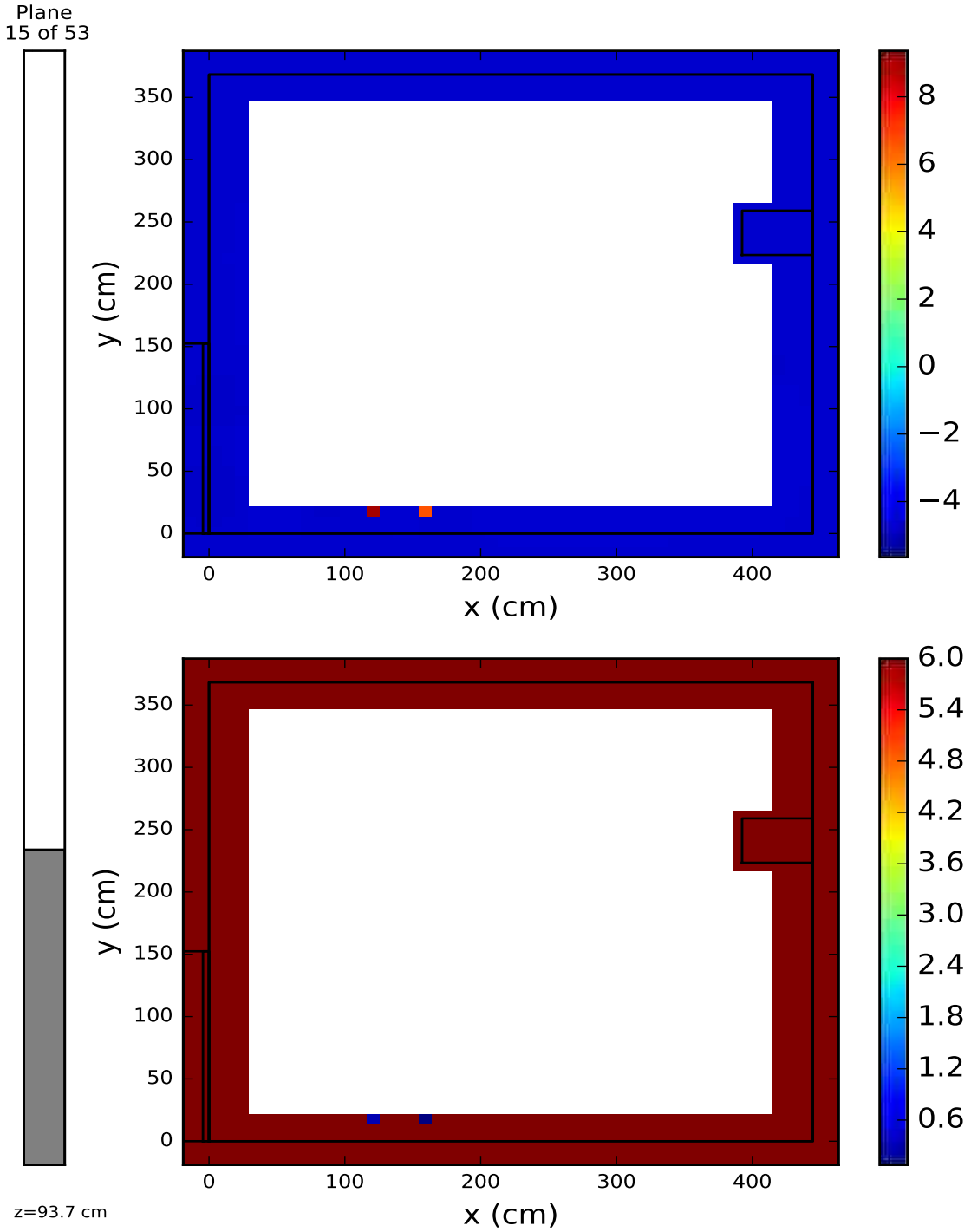

Figure 3.20 DIMP predicted source map (above) for 24 detector locations in Burlington room 2144 (search area confined to the walls) for the Co-60 line source (1173 keV peak), and the corresponding uncertainty (below).

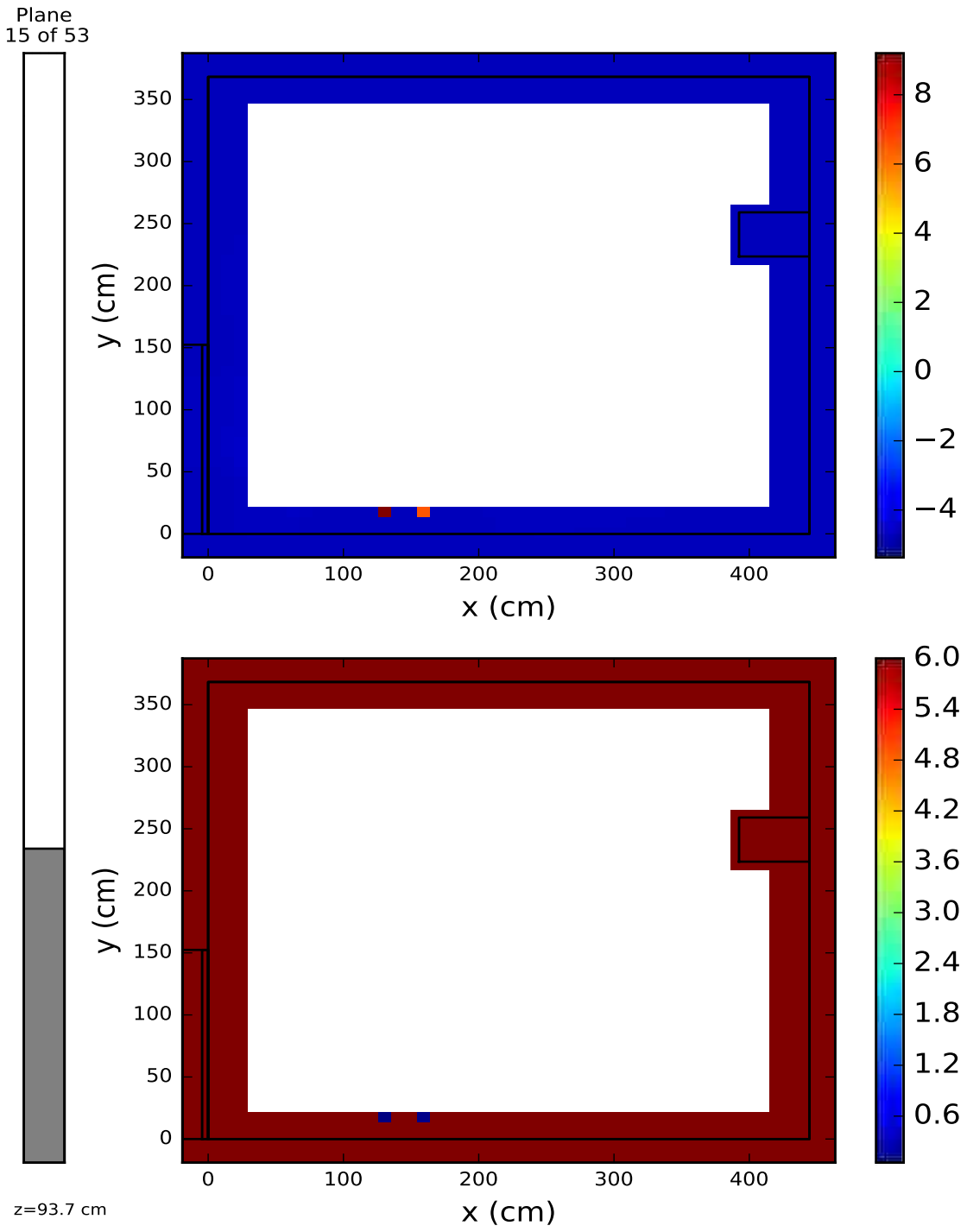

Figure 3.21 DIMP predicted source map (above) for 24 detector locations in Burlington room 2144 (search area confined to the walls) for the Co-60 source (1333 keV peak), and the corresponding uncertainty (below).

First, chi-squared per detector value decreased to 54.8, well below the 15 detector value as a result of removing the noisy response. Next, the Cs-137 line source returned to its normal configuration and the Co-60 line source stabilized in the z-plane only showing a maximum differential of two cells difference (or approximately 10 cm) from the true source location. Furthermore, these results stabilized the overall convergence trend as shown by Figures 3.22 and 3.23. Lastly, DIMP predicted source cells located at (120.9, 17.5, 87.9-not shown; 120.9, 17.5, 92.9; and 159.5, 17.5, 92.9) collectively containing 87.8% of the true source strength for the 1173 keV peak and source cells located at (130.6, 17.5, 92.9; 120.9, 17.5, 87.9-not shown; and 159.5, 17.5, 92.9) collectively containing 86.8% of the true source strength for the 1333 keV peak. Overall, it appears that DIMP can only converge 2-3 points of the line source. Part of this may be due to the large spread in source strengths, as one is 10 times stronger than the next strongest source.

Now consider the improved convergence trends shown in Figures 3.22 and 3.23

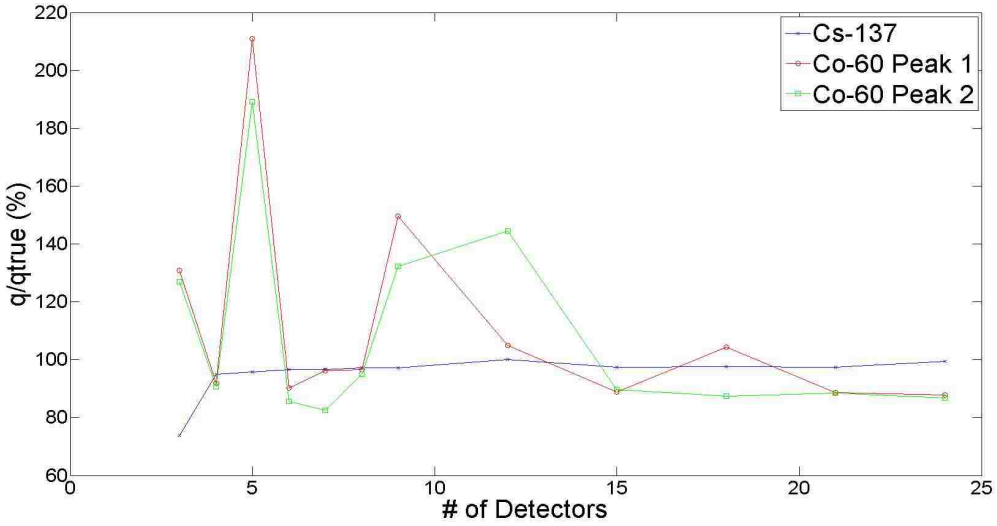

Figure 3.22 Cumulative % relative value of the true source strength for the Cs-137 point source and Co-60 line source using synthetic data from 3-24 detectors.

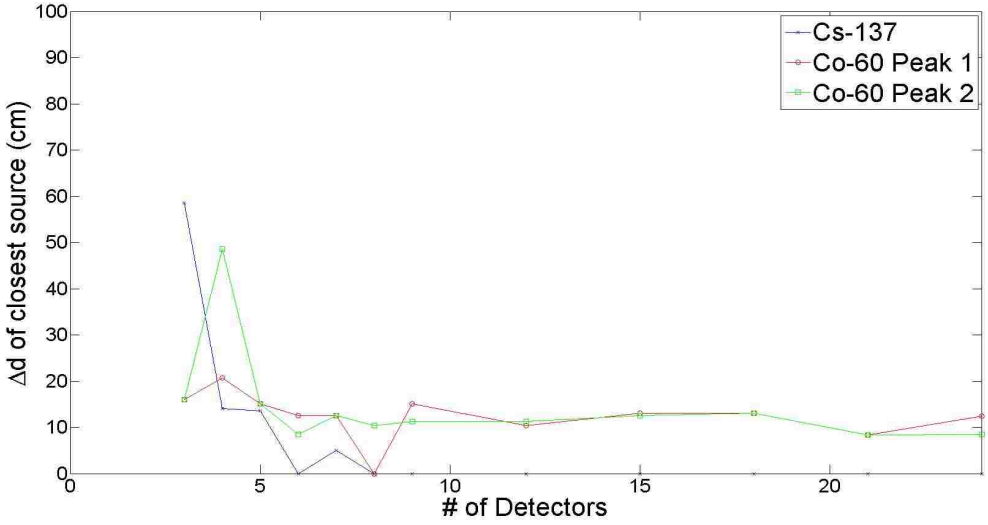

Figure 3.23 The absolute distance from the true source location of the DIMP predicted solution for the Cs-137 point source and Co-60 line source using synthetic data from 3-24 detectors. Note: Each DIMP mesh cell is approximately 5 cm x 5 cm x 5 cm.

As can be seen, the delta distance and % of the true source strength remain stable between 21 and 24 detectors after replacing the high error responses with better detector locations. Therefore, it is reasonable to conclude that DIMP is stable and converges to a solution with an increasing number of detector measurements even in the presence of multiple energies and multiple point sources.

3.2.3 Convergence of DIMP Using Unshielded Detector Responses Only

Verifying the necessity and contribution of directional responses to the performance of DIMP's source prediction is of high interest for future work. Collimated detectors require more complex DRFs in order to calculate full response spectra [12], so it would be easier and more efficient to run DIMP with only unshielded detection points (where the detector is bare, possessing neither a collimator on the front nor any shielding on the sides or rear of the detector). In order to determine DIMP's dependence on directional responses, a convergence study was conducted with only unshielded responses. This numerical simulation involved only the Cs-137 point source, as described in Section 3.1. Purely synthetic measurements generated with MCNP were used as unshielded detector responses where the number of detection points was increased from 3 to 42 points total, in order to provide an equivalent number of data points to the base six detection points case with seven responses per detection point. The results of this convergence study are shown in Figs. 3.24-3.26.

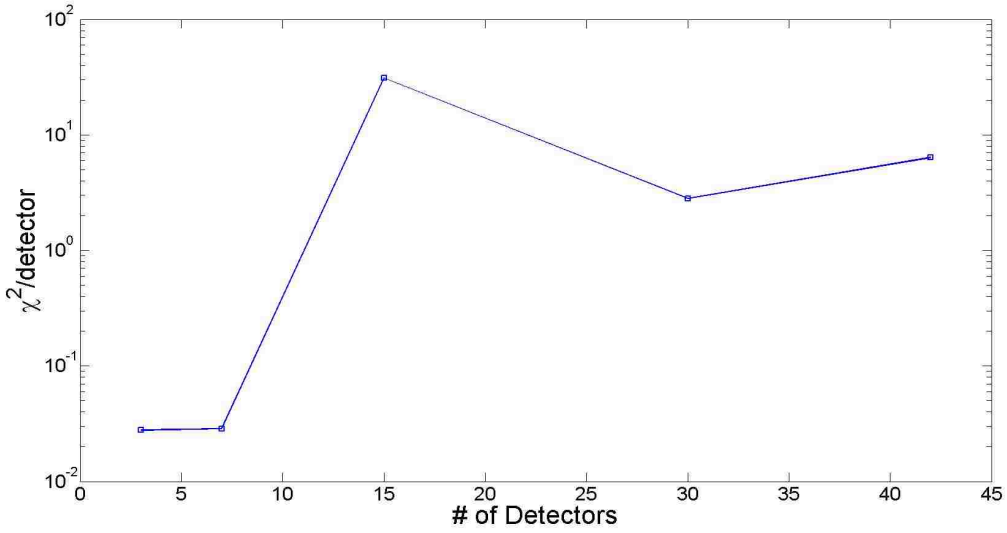

Figure 3.24 Chi-squared per detector of the DIMP predicted solution for the Cs-137 point source using purely unshielded synthetic response data from 3-42 detectors.

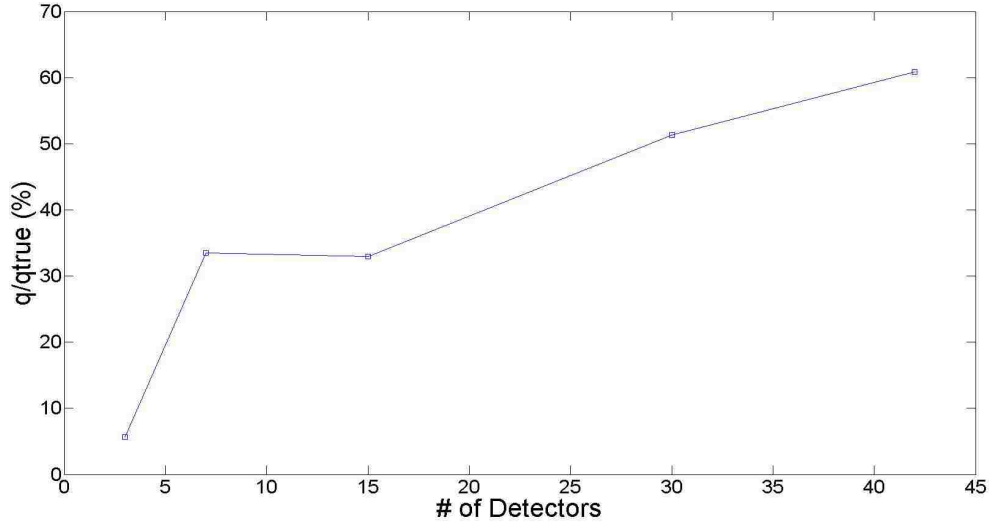

Figure 3.25 Total source strength relative to the true source strength for the Cs-137 point source using purely unshielded synthetic response data from 3-42 detectors.

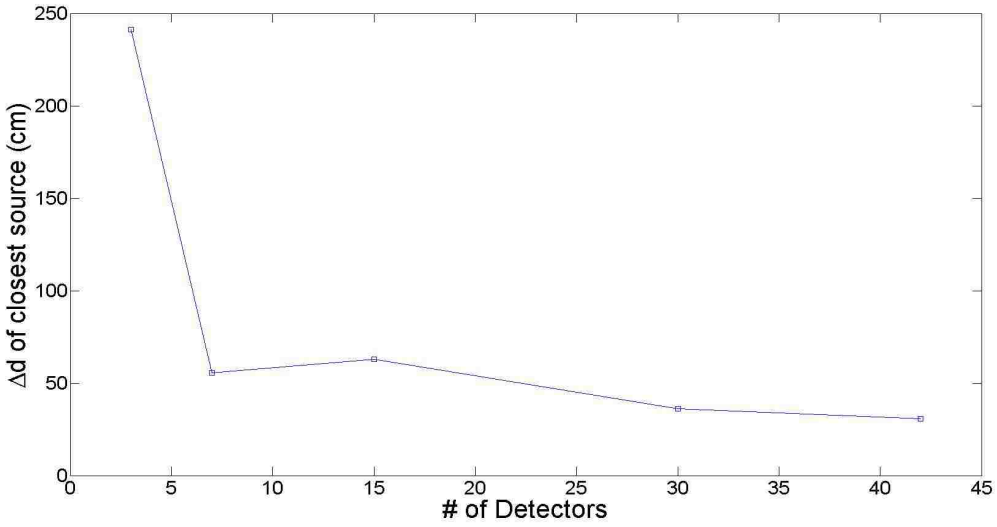

Figure 3.26 The absolute distance from the true source location of the DIMP predicted solution for the Cs-137 point source using purely unshielded synthetic response data from 3-42 detectors. Note: Each DIMP mesh cell is approximately 5 cm x 5 cm x 5 cm.

Unfortunately, DIMP did not perform well in this case. In all of the simulations, the Cs-137 point source was predicted broadly distributed throughout the mesh with the closest cells (not always the highest activity cells) being at least 5 cells (30 cm) away from the true source cell. None of the sources were above 18% of the true source strength, and the reduced chi-squared values were lower or comparable to DIMP's predictions with directional responses (Figure **??**). Usually, when DIMP predicts an incorrect source distribution, it places weak sources near prominent detector points. The possibility of DIMP being stuck in a local minimum was also investigated by using the true source distribution as an initial guess and rerunning several simulations with global DIMP. Local DIMP predicted the true solution using the true source guess; however, global DIMP yielded similarly poor source distributions with better chi-squared values. Although, local DIMP may have been stuck in a local minimum, it is very unlikely to have found the true solution as the differences in responses were high enough to keep the true solution from being the global solution of this system.

Further investigation was performed using uncollided responses only for the synthetic HEU line case study presented later in Section 5.3. These performed well with global DIMP, but it was found that neither local nor global DIMP can distinguish attenuated from unattenuated solutions. It is conjectured that this limitation may have increased the spread of possible source cells inside the walls in combination with limitations presented by the walls and corners themselves. Walls act as boundaries that inhibit detector measurements from several angles and limit the overlap of detection fields for several detectors. The Cs-137 point source in the corner would experience the

greatest difficulty in attaining detection field overlaps for localization because measurements could only occur from a 90^o spread of angles. So, sources appear to be more difficult to localize when the detector measurement locations are restricted from certain directions (e.g. sources against corners and walls).

3.2.4 Limitations of the DIMP algorithm and Assumptions for synthetic responses

While in the process of testing the convergence properties of DIMP for the original test case, two limitations of the model and model assumptions were discovered. These limitations include the alignment of sources and detection points in plane with one another and close proximity of a source to a detector. The issue arises from an assumption (involving the lead brick collimator model) made in the computation of MCNP directional responses as synthetic measurements which causes significant disagreement with the predicted responses from DENOVO under the prescribed conditions. DENOVO calculates the adjoint flux, and subsequently we compute the detector response from the adjoint flux and the source configuration at the center of the detector coordinates, whereas MCNP calculates responses at the face of the brick about five centimeters off of the detector face along the axis in the intended measurement direction. This difference between the MCNP and DENOVO models that was originally designed to simplify computation of the synthetic directional responses caused the two abovementioned limitations that produced discrepancies between the responses computed with the two models as elaborated below.

3.2.4.1 In-plane Sources and Detectors

The first limitation was discovered after poor convergence was observed for an earlier 12 detector simulation where 6 detection points were kept the same as the previous work [1], and 6 new, distinct points were chosen within the room enclosure in cells whose material assignment is air but without preference of specific locations or alignment with other mesh or room features. The resulting poorly converged results are shown in Table 3.1.

Table 3.1 Spatial distribution of the Cs-137 point source and the Co-60 line source computed with DIMP from synthetic responses of 12 detectors that include three coplanar detectors with sources.

Energy (MeV)	x (cm) Δx (cells)	y (cm) Δy (cells)	z (cm) Δz (cells)	Δd (cm)	q (Bq)	$\frac{q(E)}{q_{true(E)}}$ (%)	$\chi^2_R/det.$
1.332	140.21	17.53	97.18	14.62	3.87E3	8.76	1551
	1	1	2				
1.173	140.21	17.53	97.18	14.62	1.488E3	3.34	
	0	1	0				
1.173	130.56	17.53	97.18	10.64	1.33E3	3.02	
	3	1	3				
0.662	391.16	41.91	-0.97	61.25	7.56E3	7.02	
	-5	5	-1				
0.662	439.42	98.81	19.44	95.60	3.05E3	2.84	
	0	12	0				

Clearly, DIMP did not converge well for this early 12 detector case as evidenced by the poor agreement of strength and location with the true source and also by the large reduced chi-squared value especially in comparison with the 12 detector case shown in Figures 3.16, 3.22 and 3.23 where none of the detection points suffered the poor placement conditions under investigation in this section. This discrepancy was very puzzling considering the good agreement reported previously [1] with six detectors that are a subset of the 12 detectors employed to generate the results reported in Table 3.1. Convergent behavior of DIMP would have improved the agreement between the true and predicted source distribution with increasing number of detection points. All of the predicted source cells are excessively weak in strength and placed away from the walls at least a few cells closer to the detectors. While the Co-60 prediction was only a few cells off in location from the center of the true line source, it spans cells in the z direction instead of the x direction. The Cs-137 predicted point source is more than a few cells off from the corner of the room where the true source was located. Furthermore, the large value of the reduced chi-square per detector indicated a significant disagreement between predicted responses and the measured responses especially in view of the much smaller value of 69.73 achieved with the first six detectors [1]. Figure 3.27 compares the synthetic responses computed by MCNP with those predicted by the inner product of the true source configuration with DENOVO's adjoint fluxes. The logarithmic scale shows the overall differences in responses, while the linear scale emphasizes those in the higher intensity Co-60 responses.

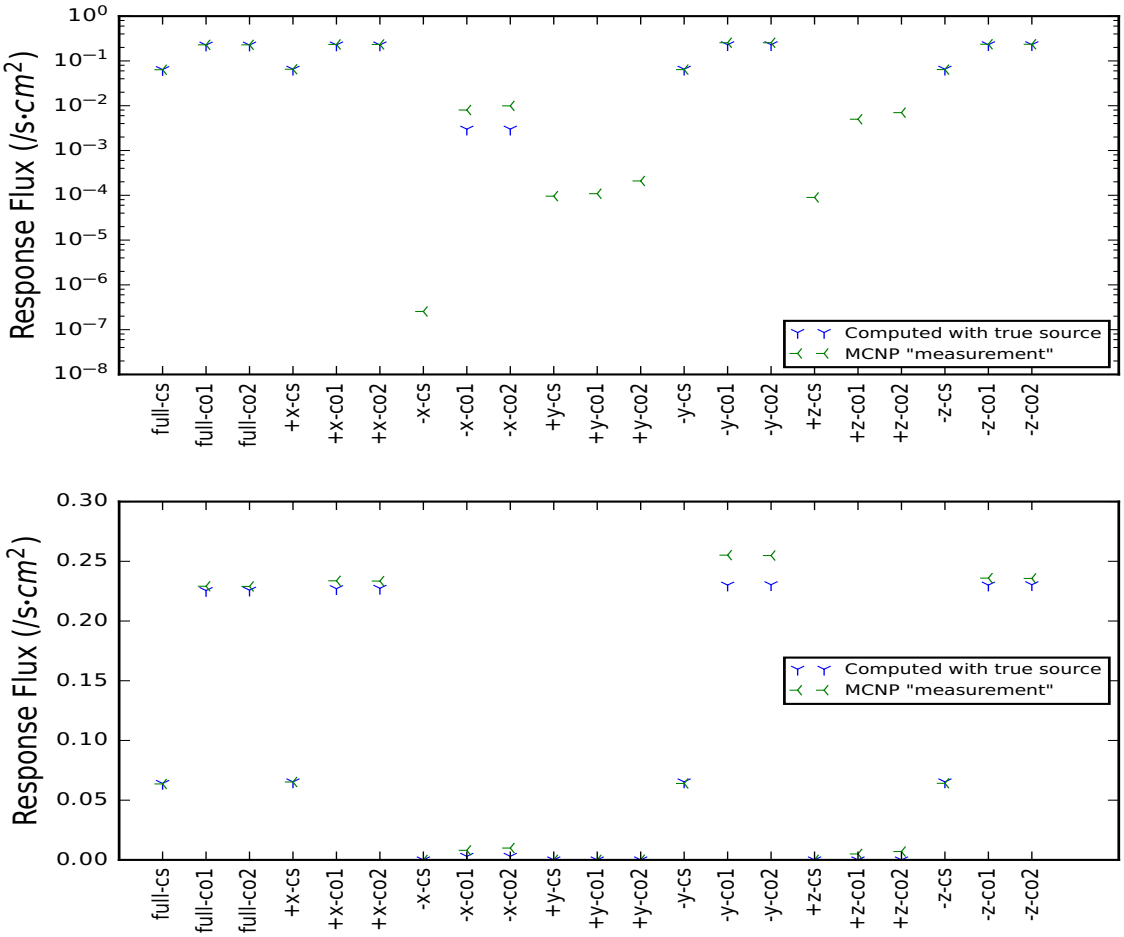

Figure 3.27 DENOVO Responses computed with the true source configuration ($\vec{r}_t$) and the MCNP synthetic responses ($\vec{r}_m$) for a detector that is in-plane with a source, and located at x=101.6 cm, y=88.9 cm, z=114.3 cm on logarithmic (top) and linear (bottom) scales. The horizontal axis indicates the type of response (collimated or uncollimated), the response's energy, and the axis of alignment if it is a collimated response.

Upon comparison of the two sets of responses, differences were observed in most of the responses (some larger than others) except for the unshielded or "full" responses. Again, the true Co-60 line source is located at approximately x=96.5-143.8 cm, y=9.5 cm, and z=90.2 cm.

Since the full responses agreed rather well, this pointed to the lead block collimator as the reason for the discrepancy. In DENOVO, the detector response is computed at a single cell, namely the cell containing the coordinates of the center point of the detector's face, and a point DRF function determines the level of attenuation for the flux at that point by the collimator. Some of the differences can be attributed to when the DRF in the DENOVO adjoint transport calculations

causes an uncollided flux to be zero, while a nonzero heavily attenuated flux is computed by MCNP. In MCNP, the lead block's center point is chosen to be the original center point of the detector face and the tally is moved approximately five centimeters along the detector's measurement axis to the corresponding face of the lead block for each directional response tally; refer to sketch in Fig. 3.28.

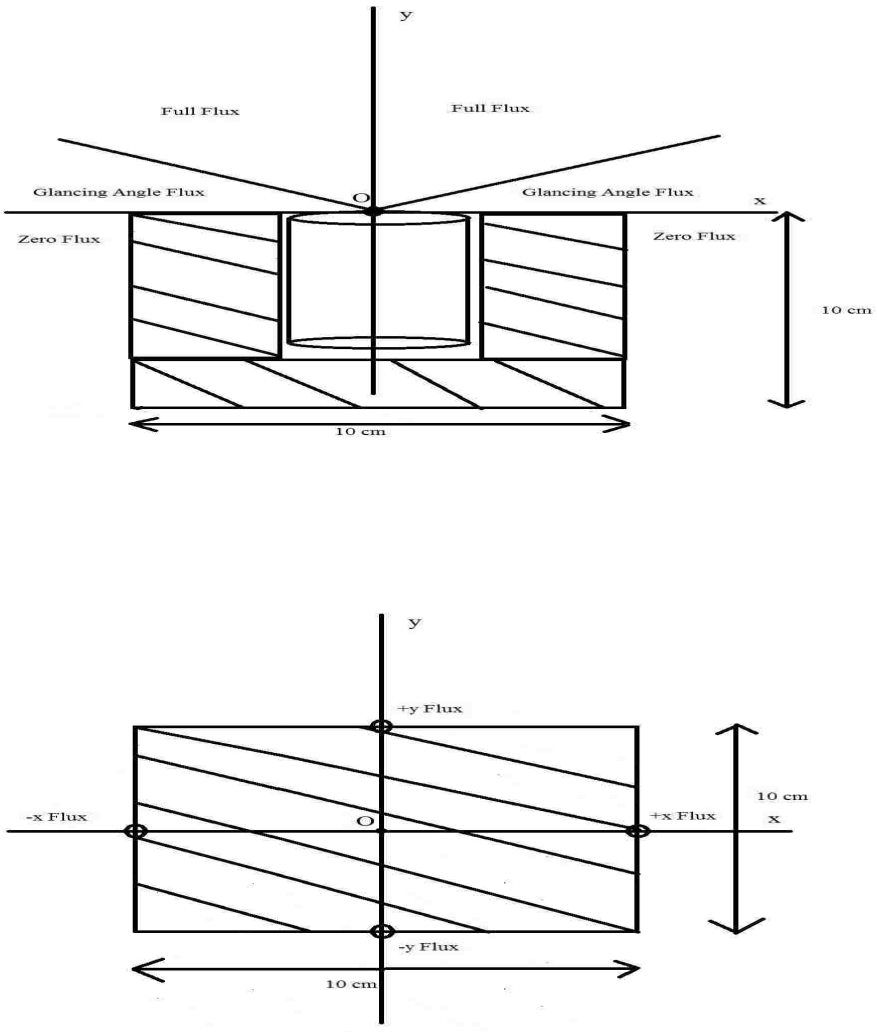

Figure 3.28 Representation of the synthetic response calculation for DENOVO (above) and MCNP (below) for an arbitrary detection point.

As seen above, the origin is shifted from the original coordinates in DENOVO by five centimeters for each directional response. In MCNP, the whole setup is replaced with a single 10 cm^3 lead cube, and the tally is shifted by five centimeters from the original origin to the face of the lead cube for

the directional response of interest. This changes the angle of incidence as well as the distance between source and detector slightly from the original geometry at the detector's face coordinates. When detector and source are co-planar, this can affect the synthetic response greatly, causing false positive or negative responses for point sources and noticeable variation in intensity for line sources. To resolve this discrepancy in the MCNP model, future synthetic collimated responses will be generated separately on a direction by direction basis (further separation may be required to prevent the tally interference effects mentioned above).

3.2.4.2 Proximity Between Sources and Detectors

A similar discrepancy in the responses was observed when all of the in-plane detectors were moved a necessary distance out of alignment with source cells, and yet, the source map was only slightly improved. The DIMP predicted source distribution yielded source distributions whose level of agreement with the true source for this 12 detector arrangement that had no coplanar sources and detectors were evaluated as displayed in Table 3.2.

Table 3.2 Spatial distribution of the Cs-137 point source and the Co-60 line source computed with DIMP from synthetic responses of 12 detectors with some detectors and sources in close proximity.

Energy (MeV)	x (cm) Δx (cells)	y (cm) Δy (cells)	z (cm) Δz (cells)	Δd (cm)	q (Bq)	$\frac{q(E)}{q_{true(E)}}$ (%)	$\chi^2_R/det.$
1.332	140.21	17.53	87.87	13.04	6.34E3	28.72	109.3
	1	1	0				
1.332	149.86	9.40	87.87	19.82	5.98E3	27.10	
	2	0	0				
1.332	149.86	17.53	79.31	23.86	5.16E2	2.34	
	2	1	-1				
1.173	140.21	17.53	87.87	13.04	6.49E3	29.42	
	1	1	0				
1.173	149.86	9.40	87.87	19.82	6.29E3	28.48	
	2	0	0				
0.662	439.42	2.67	3.31	3.33	9.63E4	89.46	
	0	0	0				
0.662	439.42	17.53	3.31	12.75	1.29E4	12.02	
	0	2	0				

In this case, DIMP's prediction is much improved, but the results were still worse than the 6 detector case reported earlier [1]. The reduced chi-squared per detector is nearly double the six detector value, and the predicted Co-60 source only reached half of its true strength. Again, comparison of the synthetic and predicted responses reveals a few discrepancies as seen for one such detector that was placed too close to the source (within 35 cm or about nine cells) in Figure 3.29 for all seven directions. The detector is closest in proximity to the true location of the Cs-137 point source (x=440 cm, y=5 cm, z=1cm).

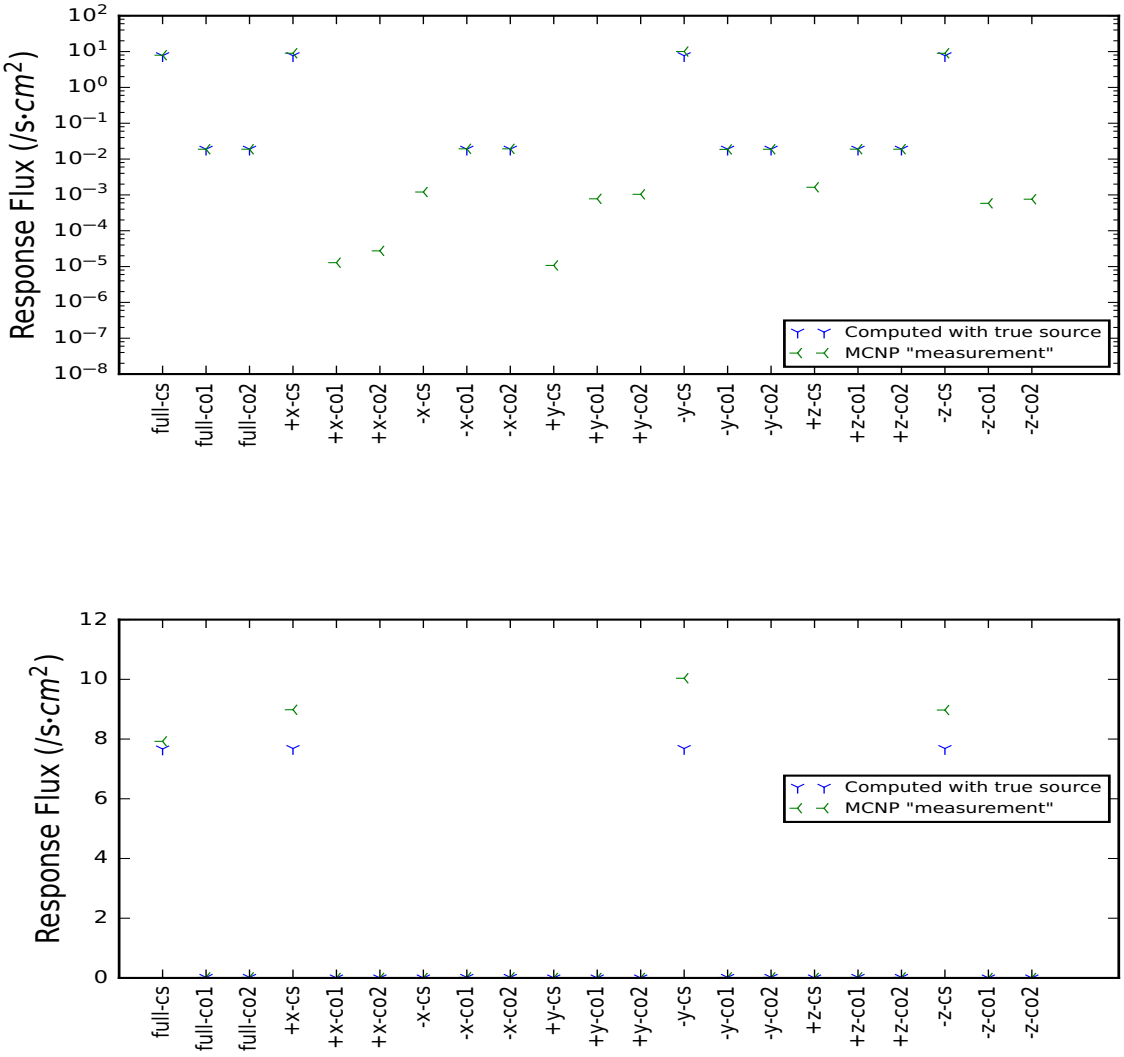

Figure 3.29 Responses for a detector in close proximity to the Cs-137 source, and located at x=424.9 cm, y=30.0 cm, z=16.0 cm on logarithmic (top) and linear (bottom) scales.

Oddly, even the unshielded responses show a slight discrepancy between the synthetic and true response values this time. The linear scale of Fig. 3.29 highlights this and illustrates the differences in the large magnitude Cs-137 responses. There is still a problem with the MCNP $+x$, $-y$, and $-z$ directional responses, since a directional response should never significantly exceed the unshielded response in magnitude as is the case for the $-y$-cs value. Here too, the cause for the discrepancy is the MCNP lead block face tally assumption. While the angular collimation-based attenuation may remain small, the geometric attenuation differences incurred by moving the detection point 5 cm closer to the source can be significant on a relative scale when the detector-source separation distance is of comparable length. The detctor locations in Section 3.1 did not suffer from these limitations and the one location that affected the results in Section 3.2 was removed improving DIMP's convergence trends.

3.3 Detector Location Parameter Study

The convergence study proved that increasing numbers of detector locations yielded better source predictions until saturation of information is reached and no further improvement is achieved by increasing the number of detectors. However, the quality of information obtained by those detector locations may yield better predictions with fewer detectors. A parametric study was performed to correlate the effects of detector location with the quality of source predictions made by both local and global DIMP. Knowing the sensitivity of DIMP source predictions to detector location will allow users to better optimize detector locations into an efficient network.

In order to determine the correlation between detector location and source prediction accuracy, 100 random detector locations were chosen for study using both local and global DIMP and stored in a database. Adjoint fluxes and MCNP measured responses were calculated for all 100 locations and all directions at each detector location using DENOVO. From the flux and measured response database made of100 detector locations, random sets of detector locations grouped from 7-24 detectors were chosen. 100 optimizations were then performed with local DIMP and 10 optimizations were performed with global DIMP on Hykes's original simulated Cs-137 point source problem. [1] Note: each global DIMP optimization requires 10 local search iterations, so the results are still relatively comparable in spite of obtaining fewer source distributions from global DIMPl. The types of detector locations referenced in the Section 3.2.4 that produced modeling inaccuracies were avoided.

3.3.1 Local DIMP

The correlated spread of local DIMP source predictions for distance from the true source location versus the fractional source strength for 7 detector groupings (Figure 3.30), 15 detector groupings (Figure 3.31), and 24 detector groupings (Figure 3.32). Each point in the figures represents a source

cell prediction in strength and distance from the true source cell location (again cell center to center). Note the source cell prediction cell may be one of several in a distribution. Each Figure has been filtered of sources under 20% of the true source strength to better display significant source trends in the tests described below. About 10-15% of smaller strength and probability sources were eliminated by the filter.

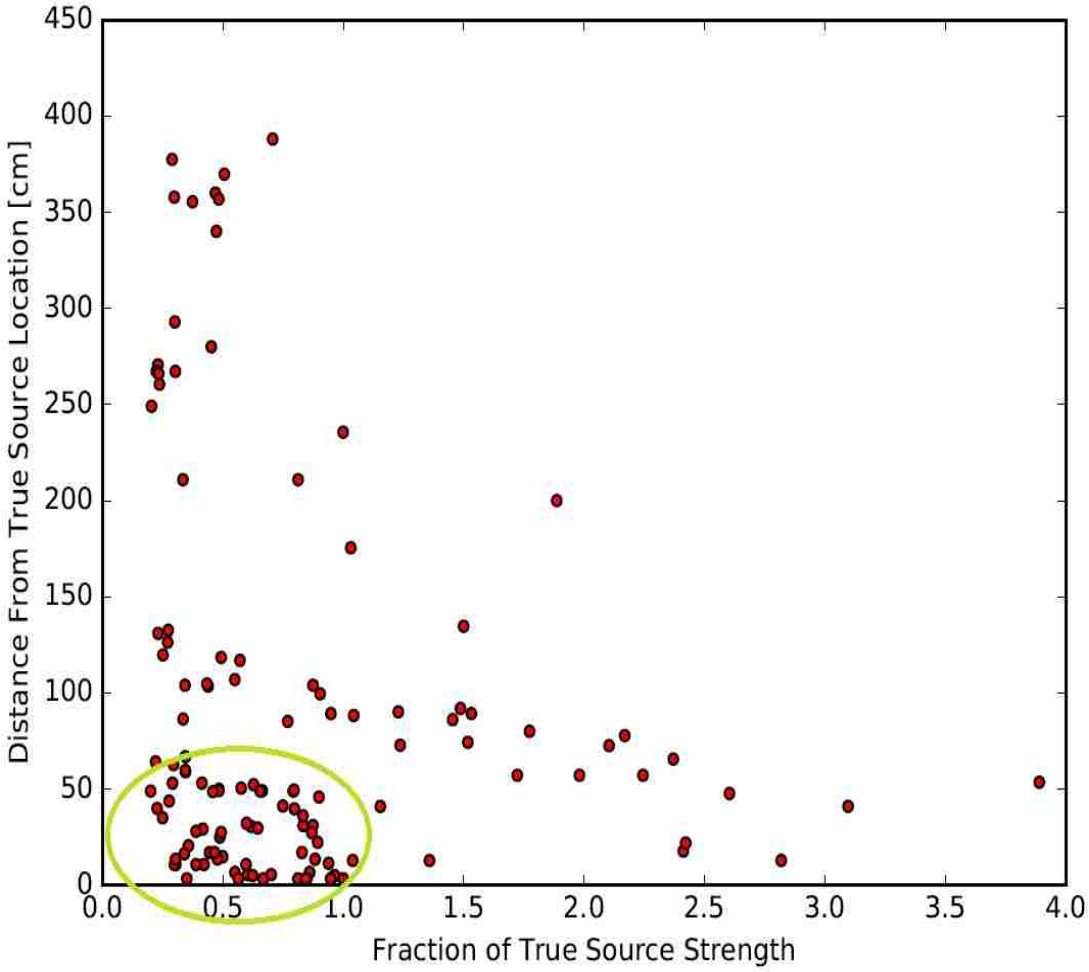

Figure 3.30 Distance from the true source location vs. the fraction of true source strength for 100 local DIMP realizations of the 7 simulated detectors, Cs-137 point source case.

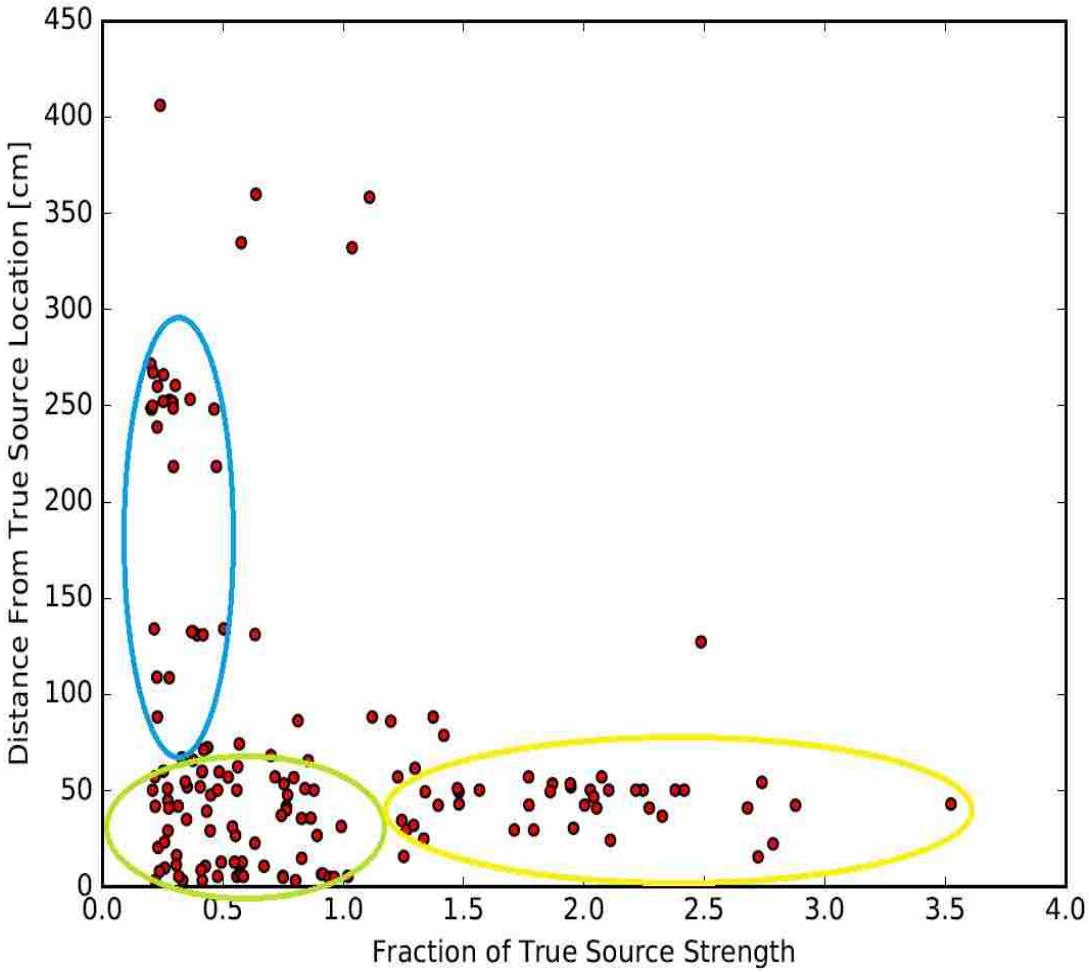

Figure 3.31 Distance from the true source location vs. the fraction of true source strength for 100 local DIMP realizations of the 15 simulated detectors, Cs-137 point source case.

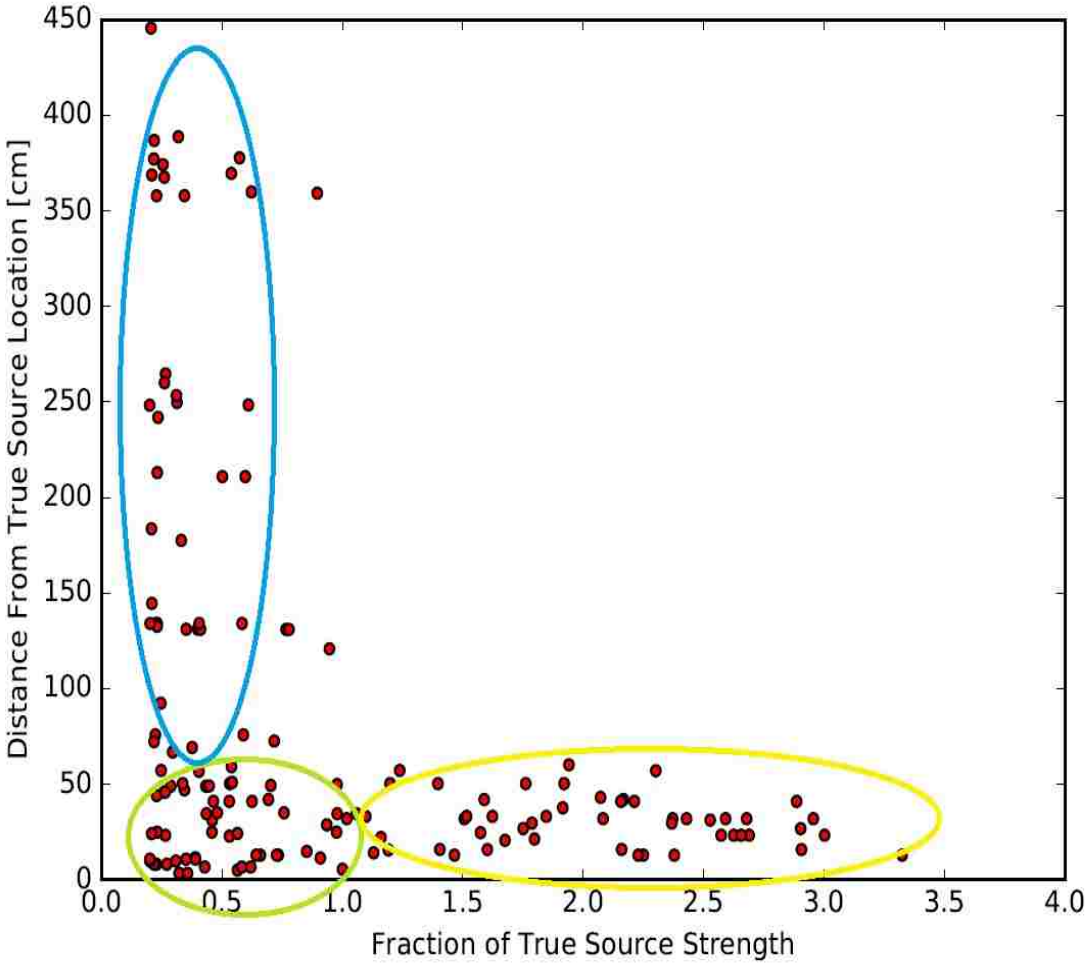

Figure 3.32 Distance from the true source location vs. the fraction of true source strength for 100 local DIMP realizations of the 24 simulated detectors, Cs-137 point source case.

The 7 detector spread shows a dense cluster (green) around the true source location, i.e. the horizontal axis, with strengths less than the true source strength and a diverse spread elsewhere. The 15 and 24 detector spread has one large cluster and two smaller clusters with tighter groupings overall. The larger cluster has low source strength and is at a small distance from true source (green), and the two small clusters are at low distance with high source strength (yellow) and the vice versa (blue). The first and second clusters consist mainly of approximately correct solutions and nearby solutions which are embedded in the walls or the floor (which increases the source strength to compensate for the attenuation). The second solution is the failure case in local DIMP where the source is placed near the floor under one or a group of detectors. Analysis indicates that increasing the number of detectors decreases the probability of poor solution predictions with diminishing

returns after 20 detectors.

3.3.2 Global DIMP

The correlated spread of global DIMP source predictions for distance from the true source location versus the fractional source strength for 7 detector groupings (Figure 3.33), 15 detector groupings (Figure 3.34), and 24 detector groupings (Figure 3.35). Again, sources under 20% of the true source strength were filtered out.

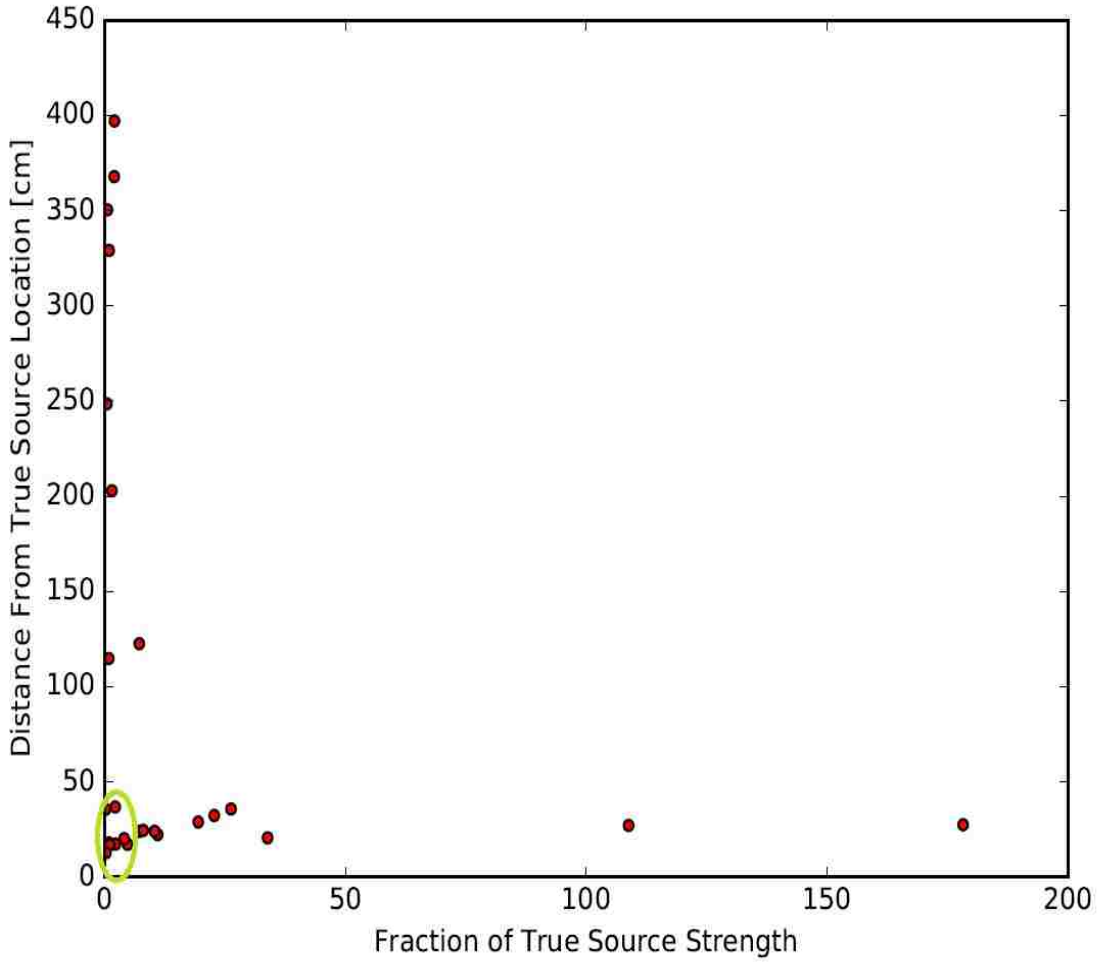

Figure 3.33 Distance from the true source location vs. the fraction of true source strength for 10 global DIMP realizations of the 7 simulated detectors, Cs-137 point source case.

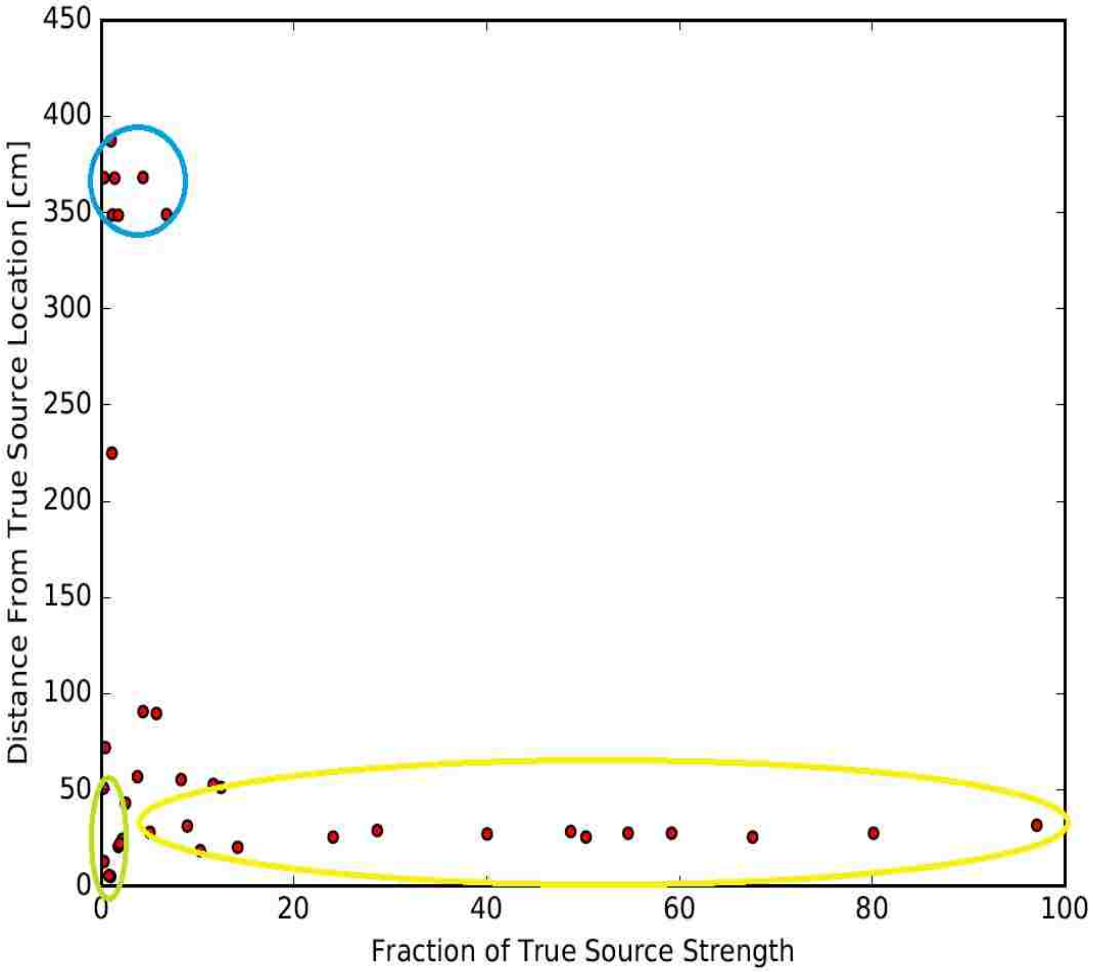

Figure 3.34 Distance from the true source location vs. the fraction of true source strength for 10 global DIMP realizations of the 15 simulated detectors, Cs-137 point source case.

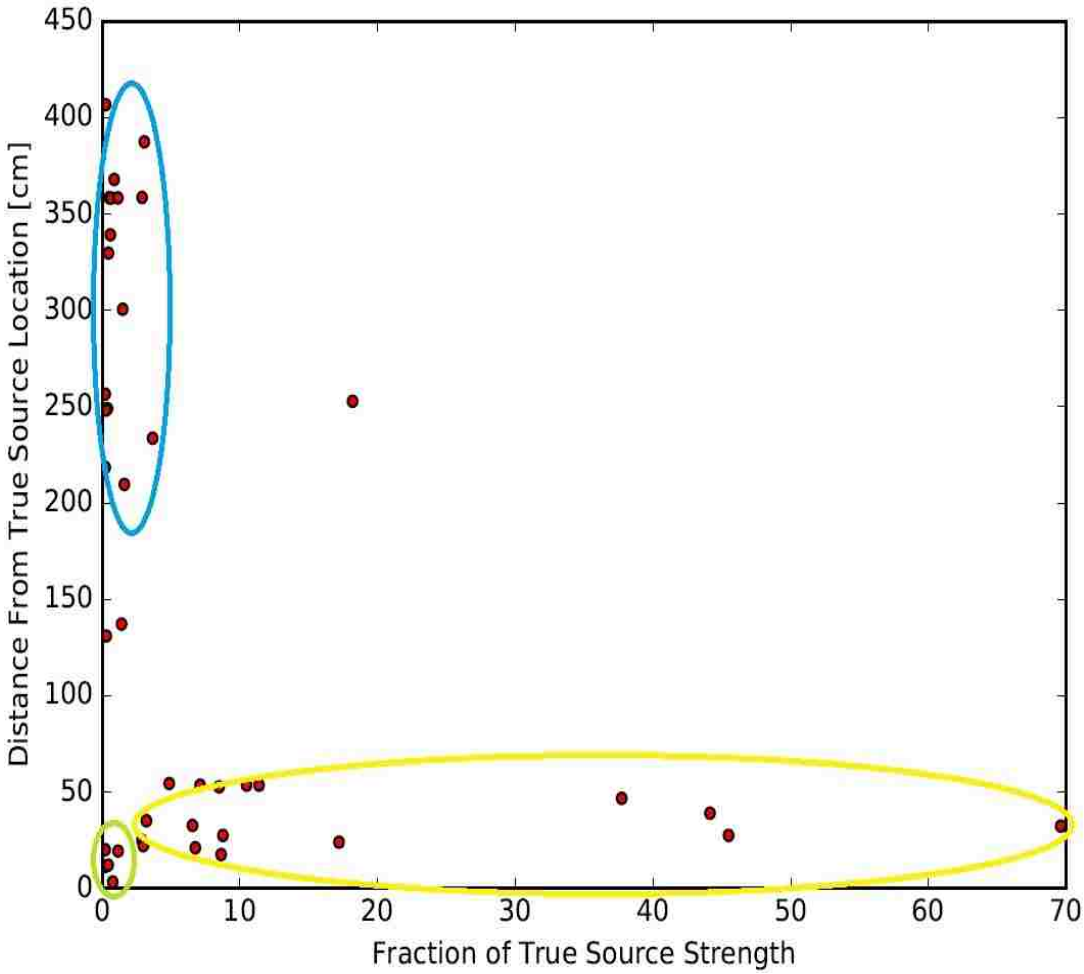

Figure 3.35 Distance from the true source location vs. the fraction of true source strength for 10 global DIMP realizations of the 24 simulated detectors, Cs-137 point source case.

Global DIMP appears to have tightened the vertical spread (source distance; blue cluster) excluding a small cluster around 400 cm in all cases but the 24 detector case following the trend of diminishing returns argument inferred from the local analysis. However, the horizontal spread was increased (yellow cluster), meaning that more sources were placed deeper into the wall. This again points to DIMP's difficulty in distinguishing uncollided sources from attenuated sources.

For both local and global DIMP, poorer prediction cases were based on a choice of a few detectors that were very far away (over 4 meters away from the true source location), close to one of the room boundaries, or had a set of detector locations that were not all distinct, i.e. some of the detector locations selected from the 100 random locations were identical. Each type of poor detector selection may have increased the overall response error. The first two cases could represent interaction of the

detector with the wall directly or just a set of weak responses due to unfavorable solid angles and distance from the source. The third case (double selected detectors), essentially reduces the detector count by one, which would reduce system information available to prediction. It is reasonable to conclude that detectors that are too close to one another (within 20 cm) would produce similar effects and adversely affect the accuracy of DIMP's source prediction. Note, that poorer sources were also generally only part of the solution, where more accurate solutions were still obtained. This means that poor detector choices do not completely sabotage DIMP but do make accurate source prediction more difficult.

CHAPTER

4

HOLDUP EXPERIMENTAL SETUP

Four measurement experimental campaigns were conducted at the Safeguards Laboratory at Oak Ridge National Laboratory (ORNL) using a calibration button point source, a high-enriched uranium (HEU) disk calibration source, a set of HEU line sources tied together within a small round duct structure, and a case with multiple HEU sources and fixtures. All HEU sources werel approximately 93% U-235. Each measurement campaign was designed to test and validate source prediction results calculated by the DIMP code system in a specific configuration relevant to the validation of the fundamental methodology or the holdup application. Each campaign's measured results (except for the first one) were also compared to the current holdup model used in practice at ORNL, HMS-4 (Holdup Measurement System). This chapter will discuss the experimental setup including source location, structure, dimensions and composition, and detector location choice rationale.

The activities and active source dimensions of the calibration source are included with all of the sources used in the measurement campaign in a consolidated table (Table 4.1). Note that only the active volume of these sources was simulated in DIMP and not their containers, since attenuation was deemed to be negligible with one exception, the HEU disk, which was encased in a 0.159cm thick stainless-steel casing instead of the typical plastic and cardboard casings.

Table 4.1 Dimensions and activities of all sources used for experimental measurements conducted in the Safeguards Laboratory at ORNL.

Point/Disk Sources						
Source	Active Radius (cm)	Thickness (cm)	Activity (μCi)	Manufactured	Measured	Activity Measured (μCi)
Cs-137*	0.25	0.318	5.01	9/28/2005	5/14/2015	4.04 ± 0.61
HEU Disk	2.381	0.0701	23.5	12/5/2004	5/19/2015	23.5 ± 0.24
Line Sources						
Source	Active Line (cm)	Diameter (cm)	Activity (μCi)	Manufactured	Measured	Activity Measured (μCi)
HEU Rod 1	28.5	0.5	3.335	5/2004	5/27/2015	3.335 ± 0.003
HEU Rod 2	28.5	0.5	3.357	5/2004	5/27/2015	3.357 ± 0.003
HEU Rod 3	28.5	0.5	3.285	5/2004	5/27/2015	3.285 ± 0.003
HEU Rod 4	28.5	0.5	3.257	5/2004	5/27/2015	3.257 ± 0.003
HEU Rod 5	28.5	0.5	3.372	5/2004	5/27/2015	3.372 ± 0.003
HEU Rod 6	28.5	0.5	3.214	5/2004	5/27/2015	3.214 ± 0.003
Area Sources						
Source	Active Area (cm)	Thickness (cm)	Activity (μCi)	Manufactured	Measured	Activity Measured (μCi)
HEU Card 1	1058	0.1	23.99	5/2004	6/29/2015	23.99 ± 0.022
HEU Card 2	1058	0.1	24.01	5/2004	6/29/2015	23.99 ± 0.022
HEU Card 3	1058	0.1	28.01	5/2004	6/29/2015	23.99 ± 0.022
HEU Card 4	1058	0.1	24.13	5/2004	6/29/2015	23.99 ± 0.022

*Note: The calibration sources used in this work were created by Eckert and Ziegler, and the active source dimensions (active radius, A.R., and thickness) used in the MCNP model were taken from the Type D disc model in the catalog. Furthermore, according to the supplier "Sources are manufactured with contained activity (Act.) values of ±15% of the requested activity value unless otherwise noted in the catalog." [18]

The HEU source record maintained at ORNL reports each source's mass. The uncertainties in the activity were calculated from the mass measurement uncertainty to be about 0.1 %. The emission energies and relative intensities of the gamma-rays of interest for each source used are listed in Table 4.2.

Table 4.2 Gamma ray energies and relative intensities with their uncertainties listed in parentheses, of all sources measured were taken from Brookhaven National Laboratory's Nudat2.6 database. [19] Unlisted uncertainties in Ref. [19] were assumed to be one in the last digit.

Source	Peak No.	Energy (keV)	Relative Intensity (%)
Am-241	1	59.5409(1)	35.9(4)
U-235	1	105.0(1)	2.00(3)*
U-235	2	109.0(1)	2.16(13)*
U-235	3	143.76(2)	10.96(14)
U-235	4	163.356(3)	5.08(6)
U-235	5	185.715(5)	57.0(6)
U-235	6	202.12(1)	1.080(23)
U-235	7	205.316(10)	5.02(6)
Ba-133	1	80.9979(11)	35.6(3)*
Ba-133	2	356.0129(7)	62.05(1)
Cs-137	1	661.657(3)	85.10(20)
Co-60	1	1173.228(3)	99.85(3)
Co-60	2	1332.492(4)	99.9825(6)

*Note: gamma-rays from the same source that were within 1 keV of each other were assigned their average energy and their intensities summed together.

4.1 Unshielded Cs-137 Button

The first measurement involved only one Cs-137 point source (calibration button source) held above the origin in the selected coordinate system for the computational models by a clamp on a ring stand. This simple experiment was performed to confirm previous results presented by Hykes [1]. It was surmised that some of the inconsistency in the previous results could be attributed to weakness of the employed sources. Although the Cs-137 button source is only slightly stronger than the source used by Hykes, it will make a good initial source configuration for the calibration of DIMP to the ORNL field detector.

In order to minimize the influence of gamma ray scattering by various objects in the lab a 5m x 5m floor space was marked with tape and cleared of all objects deemed non-essential for the experimental measurement. For the vast majority of the measurement time, this remained true. Occasionally, a chair or stool was moved within the measurement boundaries to hold the MCA, or a staff member might have walked through the marked zone inadvertently. However, the effect of these infractions on the precision of the measured response is considered negligible as no foreign object (including the chair carrying the MCA) remained in the field of view of the detector for any significant length of the measurement time.

The equipment deployed in conducting the experiment included two ring stands, a 2"x1" NaI detector, and a Cs-137 calibration source. The stands each had a pole approximately 1.5m tall and a diameter of 2cm and a rectangular base (0.27m x 0.16m). The list of coordinate locations of the center-point of the face of the detector for each detector measurement and the source location are shown in Table 4.3.

Table 4.3 Coordinate locations of the center point of the detector face for each measurement of the Cs-137 point source. The origin is located on the floor at the very center of the cleared square. The uncertainty in each measurement coordinate is 1 mm.

Measurement #	Location (cm)	Total Distance	Detector Orientation
Source	(0,0,87)	0	
1	(51,140,87)	149.0	$-y$
2	(120,32,77)	124.6	$-x$
3	(100,-20,96)	102.4	$-x$
4	(10,-74,81)	74.9	$+y$
5	(-5,-60,93)	60.5	$+y$
6	(-50,0,97)	51.0	$+x$
7	(-40,16,84)	43.2	$+x$
8	(-7,20,89)	21.3	$-y$
9	(3,10,87)	10.4	$-y$
10	(2,0.3,87)	2.02	$-x$

4.2 HEU Disc

The next validation experiment involved measuring a larger HEU source that could either be treated as an area source (multiple cells in a block) or a single cell source depending on mesh resolution. This source again was held above the origin of the measurement area by a clamp on a ring stand. This allowed for measuring a more relevant radiation source to holdup and calibrating DIMP to HEU sources without significantly increasing the complexity of the source geometry. The detector measurement coordinates and the coordinates of the center of the HEU disk source are shown in Table 4.4. A photograph of the experimental setup is presented in Fig. 4.1.

Figure 4.1 Photograph of the HEU Disk source measurement experimental setup.

Table 4.4 Coordinate locations of the detector face for each measurement of the HEU Disk source. The uncertainty in each measurement coordinate is 1 mm.

Measurement #	Location (cm)	Total Distance to	Detector Orientation
Source	(0,0,91)	0	
1	(100,-20,100)	102.4	$-x$
2	(16,-40,88)	43.2	$+y$
3	(5,-50,95)	50.4	$+y$
4	(-60,-5,97)	60.5	$+x$
5	(-74,10,85)	74.9	$+x$
6	(-7,20,93)	21.3	$-y$
7	(3,10,91)	10.4	$-y$
8	(2,0.3,91)	2.02	$-x$
9	(40,0,91)	40.0	$-x$
10	(6,-1,91)	6.08	$-x$

4.3 HEU Line Source in the Small Round Duct

The next set of experiments involved the arrangement of various HEU sources chosen from Table 4.1 within three steel fixtures to simulate realistic holdup in a facility environment. The three fixtures were: a small round duct, an L-duct, and a pipe array. The coordinate locations and the dimensions of the fixtures and their respective carts are displayed in Table 4.5. Each cart is a metal dolly with wheels and steel strut supports to hold the fixture in place. Detailed drawings of the small round duct and the L-duct are included in Figs. 4.2 and 4.3. The pipe array is not included because it was never filled with a source.

Table 4.5 Coordinate locations and dimensions of the holdup equipment structures.

Fixture	Dim. 1 (cm)	Dim. 2 (cm)	Dim. 3 (cm)	Dim. 4	Obj. Center Loc. (cm)
SRD Cart	x=57	y=122	z=2.54	Th.≈0.25	(0,0,8)
L-duct Cart	x=122	y=57	z=2.54	Th.≈0.25	(140,140.5,8.27)*
Pipe Ar. Cart	x=122	7=57	z=2.54	Th.≈0.25	(-131,-152.5,8.27)
SRD	L=189	R_{out}=7.5		Th.≈0.45	(0,-1,123.5)
L-duct	x=175	y=38	z=91/76/61	Th.≈0.5	(118,141,106.5/99/91.5)
Pipe Array	L=130	R_{out}=2		Th.≈0.55	(-129,-152.5,95)

*Note: The height dimensions are variable along three sections of the L-duct.

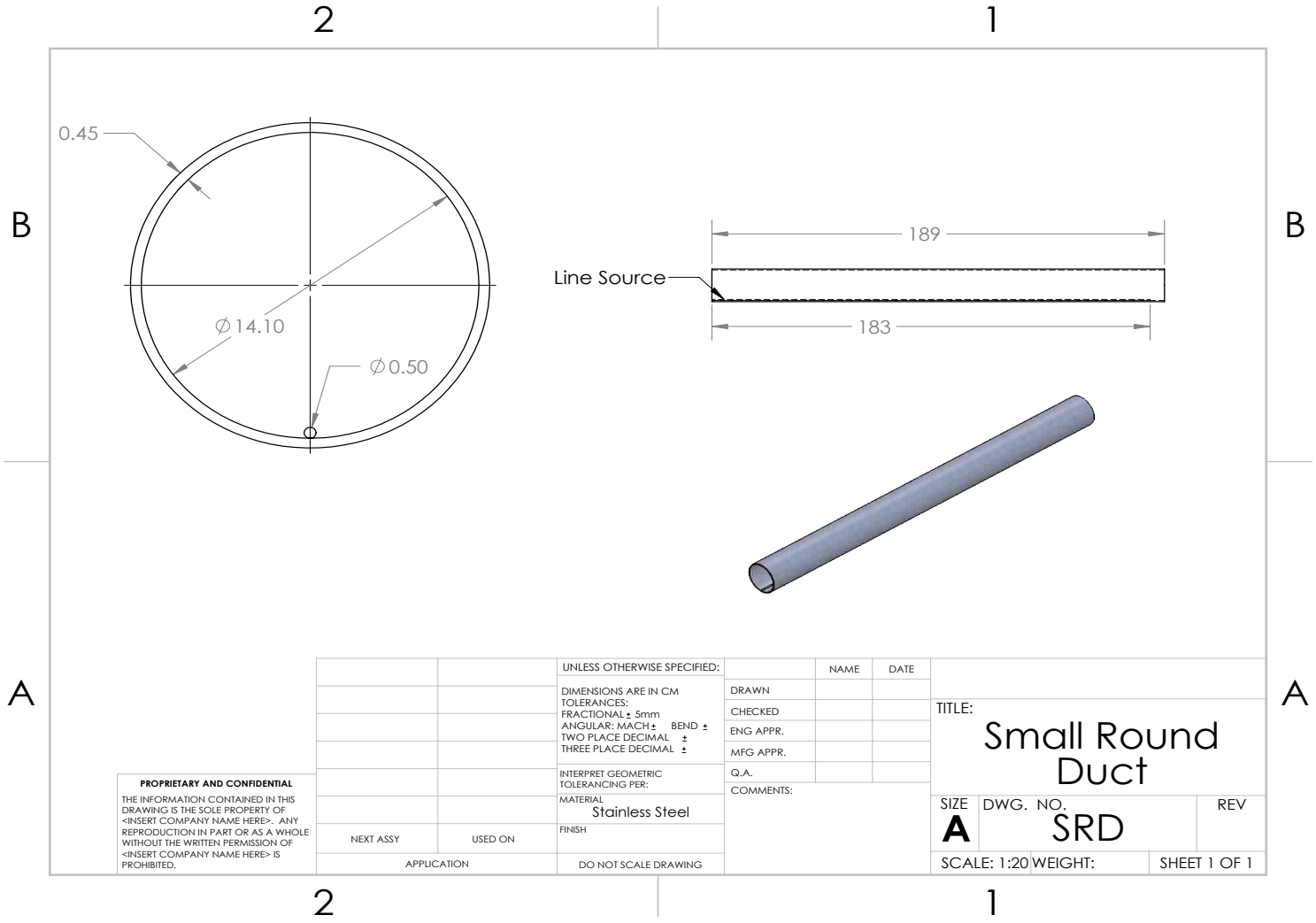

Figure 4.2 Drawing of the small round duct fixture with the appropriate dimensions.

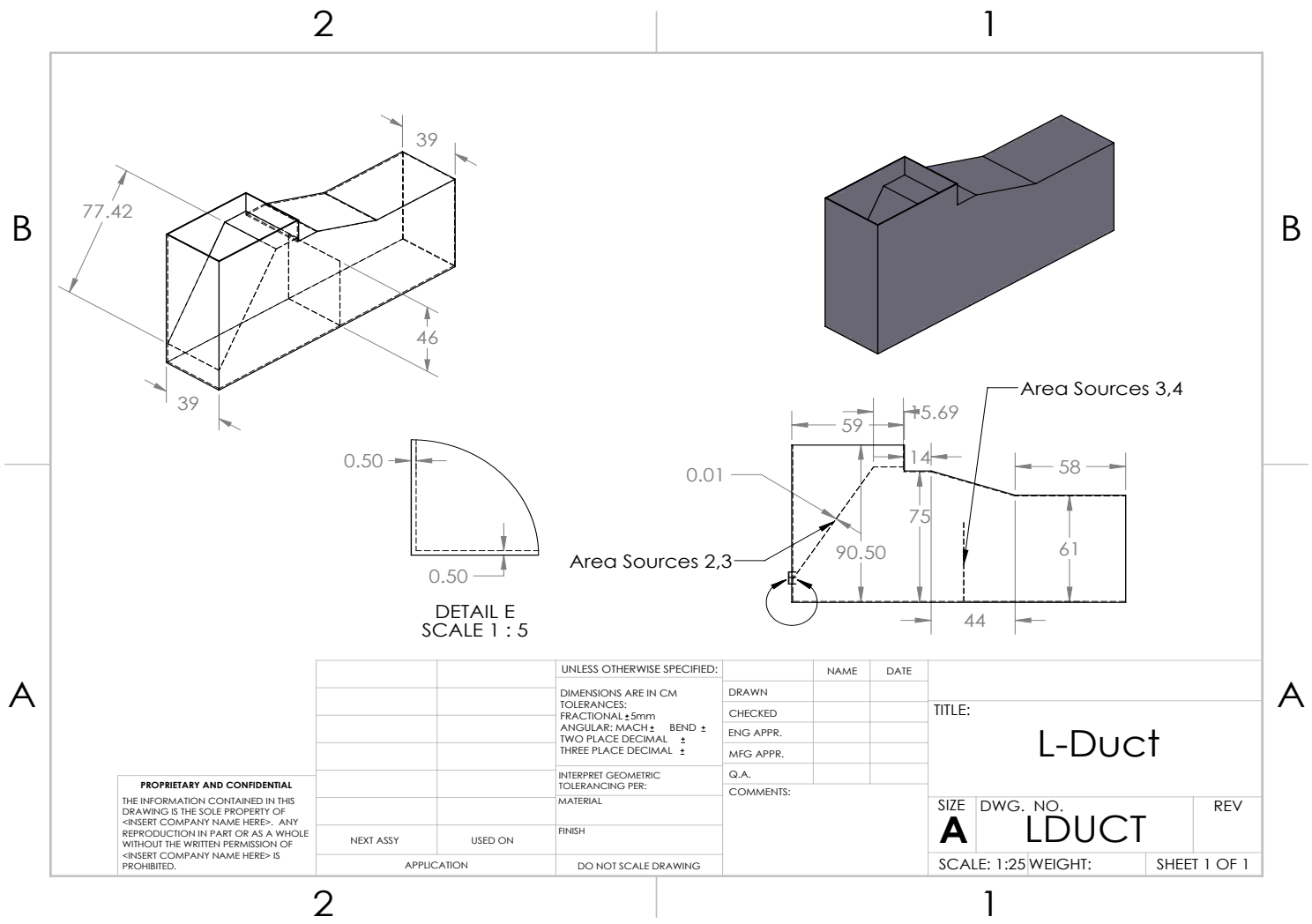

Figure 4.3 Drawing of the L-duct fixture with the appropriate dimensions.

For the first case, the small round duct was loaded with a set of six line sources taped end to end across the majority of the length of the pipe (the source did not span the last six centimeters of the southern end of the pipe). The pipe was enclosed on both ends with steel end caps. The coordinate locations for each detector measurement and the center of the line source are displayed in Table 4.6. A photograph of the general experimental setup is included for perspective in Fig. 4.4

Table 4.6 Coordinate locations of the detector face for each measurement of the line sources in the small round duct. The uncertainty in each measurement coordinate is 1 mm.

Measurement #	Location (cm)	Total Distance to Midpoint of the Source	Detector Orientation
Source	(0,1.5,116.5)	0	
1	(36,-74.2,115)	36	$-x$
2	(36,-43,115)	36	$-x$
3	(36,-12.8,115)	36	$-x$
4	(36,17.8,115)	36	$-x$
5	(36,48.5,115)	36	$-x$
6	(36,79.2,115)	36	$-x$
7	(-10,-50,120)	10.6	$+x$
8	(-20-,-25,112)	20.5	$+x$
9	(-50,10,107)	50.9	$+x$
10	(-60,40,123)	60.4	$+x$
11	(0,114,117)	20.5	$-y$
12	(0,-104,119)	13.7	$+y$
13	(0,1.5, 81)	35.5	$+z$

Figure 4.4 Photograph of the general holdup-like source measurement experimental setup.

4.4 HEU Line Source in the Small Round Duct & HEU Area Sources in the L-Duct

For the final case, the small round duct was left loaded with the same source as in the previous case, and then the L-duct was loaded with four rectangular area sources (also known as "card" sources). The first two were taped together vertically across the diameter of the duct at the eastern section. The other two card sources were taped diagonally across a filter in L section at the western end. This geometry was chosen as a difficult geometry for traditional holdup measurements. The coordinate locations of the center of each card source and those of the detector measurements are shown in Table 4.7. Although the additional sources in the final case were measured, this case was left as a simulation case for future work due to measurement discrepancies discovered in the detector responses for the HEU cases.

Table 4.7 Coordinate locations of the detector face for each measurement of the line sources in the small round duct and the area sources in the L-duct. The uncertainty in each measurement coordinate is 1 mm.

Measurement #	Location (cm)	Total Distance to Source Center	Detector Orientation
Source 1	(0,1.5,116.5)	0	
Source 2	(46.5,141.5,83.28)	0	
Source 3	(78.28,141,123.5)	0	
Source 4	(120.5,133.5,86.4)	0	
Source 5	(121,148.5,86.4)	0	
1	(36,-74.2,115)	36	$-x$
2	(36,-43,115)	36	$-x$
3	(36,-12.8,115)	36	$-x$
4	(36,17.8,115)	36	$-x$
5	(36,48.5,115)	36	$-x$
6	(36,79.2,115)	36	$-x$
7	(-10,-50,120)	10.6	$+x$
8	(-20-,-25,112)	20.5	$+x$
9	(-50,10,107)	50.9	$+x$
10	(-60,40,123)	60.4	$+x$
11	(0,114,117)	20.5	$-y$
12	(0,-104,119)	13.7	$+y$
13	(36,27.8,116.5)	113	$+y$
14	(36, 79.2,116.5)	62	$+y$
15	(22.5,141,83.3)	24	$+x$
16	(30.5,141,123.5)	47.8	$+x$
17	(116.8,184.1,84.4)	35.9	$-y$
18	(108,230,92.4)	82.6	$-y$
19	(122.8,97.9,90.4)	38.8	$+y$
20	(135.8,32,80.4)	102.7	$+y$
21	(78.3,180,123.5)	39	$-y$
22	(126,210,86.4)	61.7	$-y$
23	(62.3,62,83)	80.6	$+y$
24	(80,22,94.9)	122.4	$+y$
25	(215.5,141,86.4)	94.8	$-x$

4.5 Simulation Experimental Geometry

The base simulation geometry for all experiments includes a main void cell on top of a floor cell composed of a standard tile and concrete mixture across a 5m x 5m square area. The cells are contained between −2.5 m on the west boundary to +2.5 m on the east boundary. The same is true for −2.5 m from the south boundary and ending at +2.5m at the north boundary. The origin is in the center, just above the upper floor surface boundary. The z axis is defined from −10 cm (the underside of the floor) to 3 m above the floor. For DENOVO, each cell (e.g. floor, steel fixtures, ring stand, etc.) is simulated with parallelepipeds to approximate all of the necessary surfaces in Cartesian geometry since DENOVO does not permit curved surfaces. However, curved surfaces were employed in the synthetic response simulations to model the detector and the geometric arrangement executed by MCNP.

Though the physical geometry of the detector is simulated in MCNP, it is not simulated in DENOVO. Instead, the response values are taken at the center face of the detector after multiplying the adjoint source by a point DRF factor to approximate the effects of the shielding and collimator. The current point DRF formulation used by DIMP is described in Ref. [10].

4.6 Experimental Measurement Equipment

The field equipment used to take measurements for all experimental campaigns included a detector with a preamplifier and a multichannel analyzer with full pulse processing integration. Both pieces of equipment were essential for HMS-4 and DIMP holdup measurements.

The detector was a 1 inch diameter by 2 inches height right cylinder EFC Model 1X2P collimated NaI scintillation detector. This is a standard field detector for HMS-4 measurements. [4] The detector is well shielded with lead except on the front face where the collimator aperture allows radiation into the detector from a limited extent of directions, i.e. fixed solid angle. Hence, the detector has approximately a 23 degree in-axial-plane angle of vision from the axis normal to its circular front face.

The MCA is a GBS Elektronik GmbH MCA-166 Rossendorf model [20] that has a self-contained set of pulse processing equipment. The MCA receives a preamplified signal directly from the detector through a coaxial cable, which it amplifies and counts across a spectrum of energies. The number of counts is divided into channels (proportional to energy) and sent directly to the computer for recording and post-processing.

4.7 Holdup Measurement System (HMS-4) Methodology

HMS-4 is a code created at Oak Ridge National Laboratories to predict the amount (in grams) of material in a Uranium holdup deposit. This is done using the Generalized Geometry Holdup (GGH) model [21]. There are four core requirements of GGH methods. One, heavy metal shielding must be placed on the sides and back of the radiation detector to limit detection to forward facing radiation sources. Two, a cylindrical collimator must be used to define the field of view to a symmetric solid angle. Three, every holdup source must be assumed to be either a point, line, or area source with respect to the detector's two dimensional field of view. Four, each measurement must be performed from a relatively well qualified known distance from the radiation source of interest.

Furthermore, a strict calibration with a known source is used to measure the angular response of the detector by incrementally moving the calibration source away from the central axis of the detector along a perpendicular vector (similar to the measurements performed in [12]). Several other correction factors such as finite source dimensions, equipment attenuation, infinite thickness, etc. [21] are needed as well to perform measurements with HMS-4, which requires a lot of upfront knowledge by the operator. Typically, such information is obtained by survey crews with scanning radiation detectors and process knowledge. Once a holdup deposit is found, it can be quantified by HMS-4. The advantage of DIMP is to find radioactive sources passively without the need for prior knowledge of the holdup source or restrictive source distribution assumptions.

For the comparative measurements, some measurement locations were chosen to optimize HMS-4 requirements. For example, the first six small round duct line source measurement locations were chosen at equal spacing along the side of the pipe to optimize the amount of the line source measured by detector field of view and low measurement time (similar to field measurements). Most HMS-4 measurements locations were also used in DIMP for convenience.

CHAPTER

5

FINAL EXPERIMENTAL AND SYNTHETIC VALIDATION RESULTS

DIMP performed fairly well for the first ORNL experiment involving the Cs-137 point source after some adjustments. Under the standard initial guess ($\alpha = 10^{-4}$, the baseline static low source cell probability), DIMP failed to predict any source cells with magnitude larger than 1% of the true source strength, however using the true source configuration as the initial guess yielded a very good result alluding to DIMP becoming trapped in a local minimum during the first source search. The usual initial guess is chosen with a flat low source probability in every mesh cell allowing feedback with the measured responses to increase the source probability in the appropriate cells. Also, a correction factor had to be applied to the measured responses to account for the effects observed as a result of the special collimator geometry for ORNL's 1" x 2" NaI field holdup detector that were not featured in the previous detector design used in Ref [1] and utilized in the synthetic data presented in previous chapters of this work. Furthermore, two measurement points had higher than expected flux values for both the Cs-137 point source and the subsequent HEU disk source measured in a similar manner. One point was merely measured too close to the source and was made to equal the measured value (for the true source configuration), thereby minimizing its impact on the DIMP optimization.

5.1 Cs Point Source Validation

5.1.1 Development of the Collimation Correction Factor

The detector used in [1] was a 2" x 2" NaI detector, collimated by the placement of lead bricks (as in sketched Fig. 3.28) above and to the sides of the detector to produce a forward facing hemisphere FOV. The 1" x 2" NaI field holdup detector provided by ORNL to conduct the measurement campaigns has a more complex collimator that narrows the FOV to roughly 23 degrees and partially obscures the crystal face.

The front of the lead collimator touches the crystal face and covers about 12% the face reducing the detector's solid angle FOV. Since the previous configuration [1] did not suffer such a reduction in solid angle, DIMP requires a collimation correction factor to adjust the detector efficiency for the effect of this collimation on the directional responses. The reduction in solid angle is illustrated by Fig. 5.1

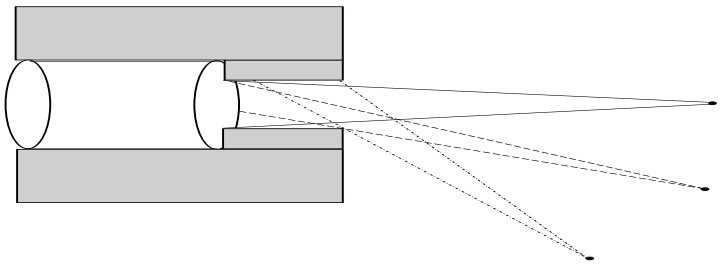

Figure 5.1 Sketch of the detector collimator shadowing effect on the detector crystal (reducing the effective solid angle).

A fairly simple way to compute such a factor, is to simulate the detector with and without the collimator geometry (just the detector crystal) in MCNP and compare the results to the analytical solid angle calculations. Using the ratio of the two fluxes (with and without the collimator) as the

collimation correction factor, the measured responses can be corrected by this factor to better match the responses predicted by the true source distribution folded with DENOVO adjoint fluxes. Thus, the collimation correction factor ($S_{col}(\vec{r},E)$) can be calculated as follows

$$S_{col}(\vec{r},E)=\frac{\phi_{col}^{syn}(\vec{r},E)}{\phi_{unc}^{syn}(\vec{r},E)} \tag{5.1}$$

where $\phi_{col}^{syn}(\vec{r},E)$ and $\phi_{unc}^{syn}(\vec{r},E)$ are the collimated and uncollimated synthetic responses calculated from the true source configuration in MCNP. Dividing the measured responses by $S_{col}(\vec{r},E)$ will produce an approximate value of the response that would have been measured with a 2 π FOV detector that is assumed in the current version of DIMP. A more appropriate way to account for the collimator's effect is to determine a directionally dependent DRF.

5.1.2 Local DIMP Result

The correction factor was used to adjust each of the measured responses from the Cs-137 point source campaign before initializing both local and global DIMP's source search algorithm. The experiment involved ten detection points measured within the experimental area in a spiral pattern around the 4 μ Ci point source held by a clamp on the ring stand (similar to the HEU setup in Fig. 4.1). The distance between the source and detection points ranged from 0.02-1.25 m as discussed in the previous chapter, and the coordinates of the true Cs-137 point source are (0,0,87) cm.

Consider the local DIMP predicted source map shown in Figure 5.2.

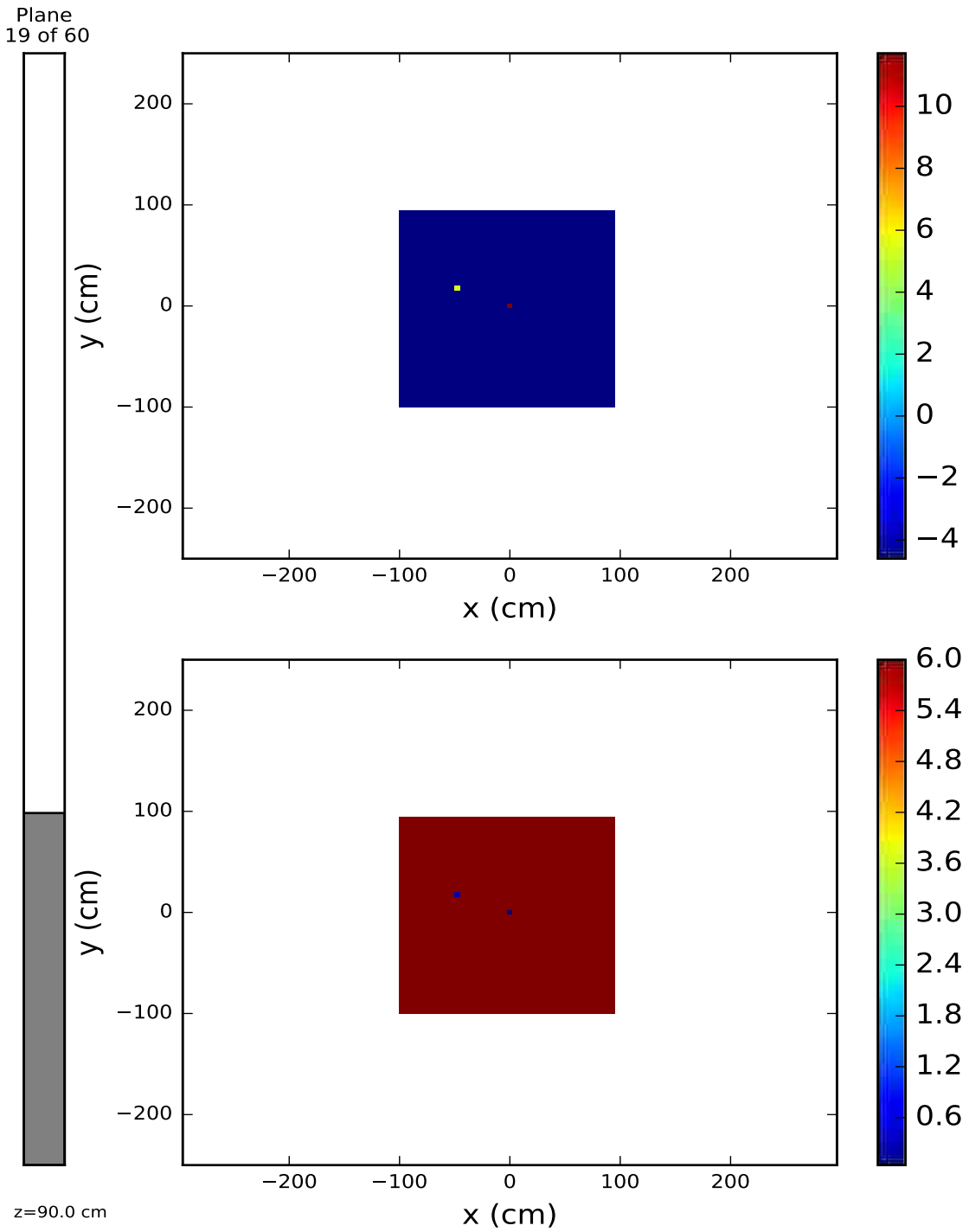

Figure 5.2 Local DIMP predicted source map (top) for a 5m x 5m square space (reduced to a 2m x 2m search area) with a Cs-137 point source suspended by clamps on a ring stand, and the corresponding uncertainty (bottom).

As seen in this figure, local search DIMP (local optimizer only) performed well predicting the source in the correct cell (0,0,90) cm with 80% of the true source activity with fairly low uncertainty and a chi-squared value of only 9.83. Since the number of detector measurements per location is not kept consistent with the convergence study (Section 3), only the absolute chi-squared values will be reported for comparison in this section. Only 80% of the true source strength was obtained because the corrected measured responses still had a margin of error when compared with those calculated by DENOVO. This is a promising result for the first of four experimental measurements, but there are two issues with this result. The first, is that as in [1] the source search space had to be narrowed to a smaller number of mesh cells in order for DIMP to find a reasonably accurate source distribution. Otherwise, the gradient source search algorithm often becomes stuck in local minima and predicts weak distributed sources. Secondly, two of the detection point fluxes computed by DENOVO did not match up with MCNP synthetic fluxes, so for the time being they were adjusted to the synthetic values artificially. More than likely the MCNP point source approximation of the source geometry was invalid for those points, since both points were measured with the detector placed fairly close to the source location.

5.1.3 Global DIMP Result

Now consider the global DIMP predicted source maps shown in Figures 5.3 and 5.4

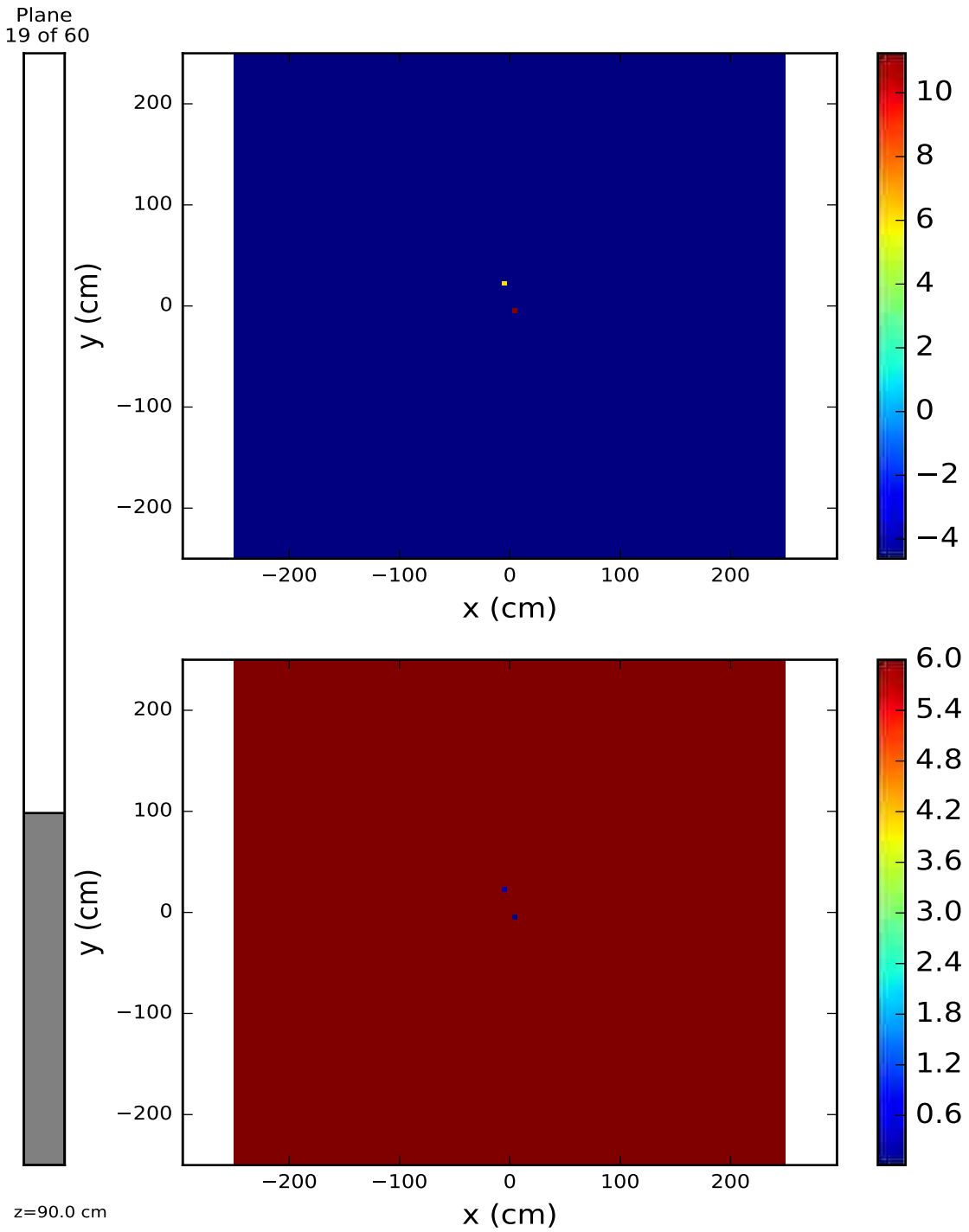

Figure 5.3 Global DIMP predicted source map (top) for a 5m x 5m square space (reduced to a 2m x 2m search area) with a Cs-137 point source suspended by clamps on a ring stand, and the corresponding uncertainty (bottom).

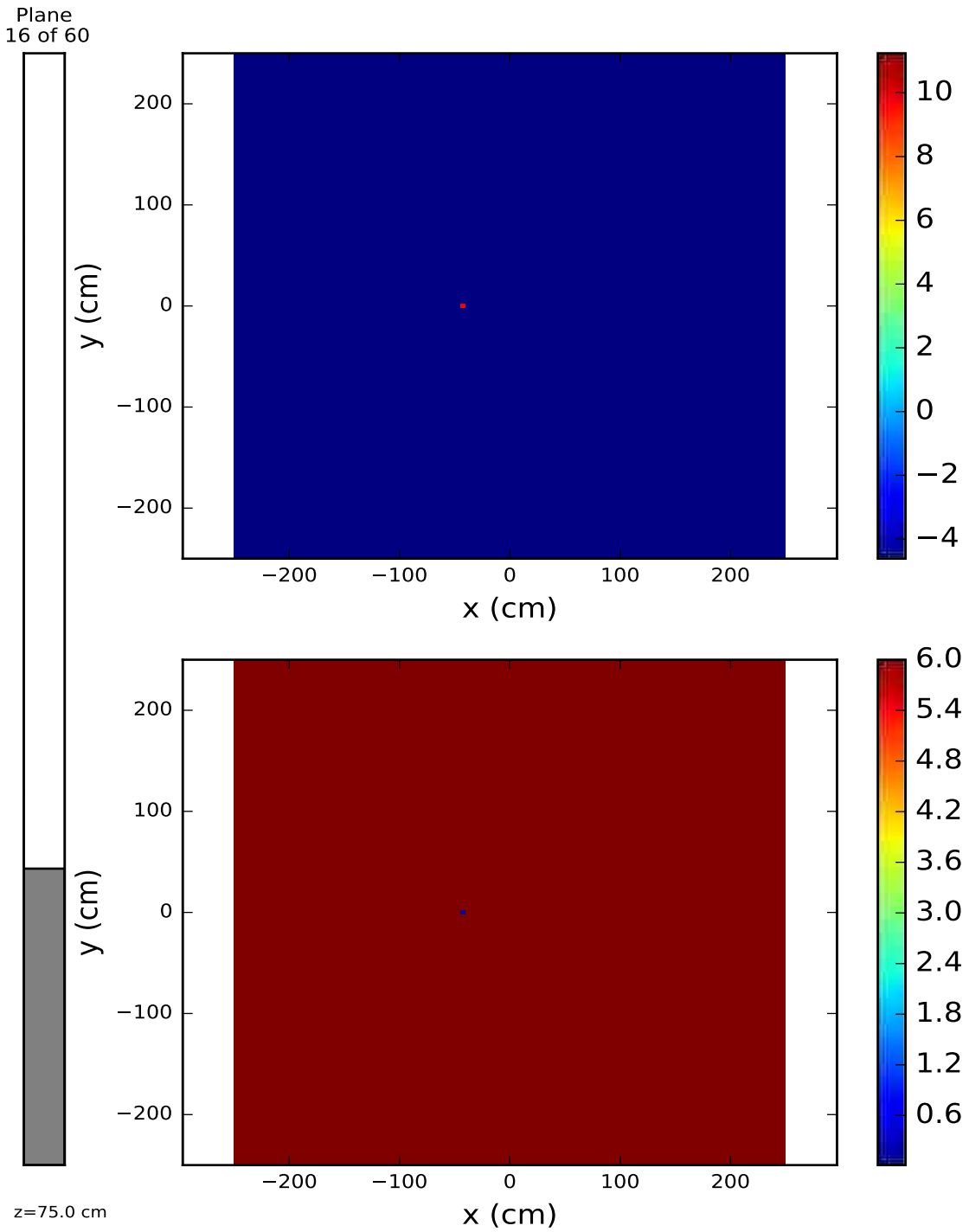

Figure 5.4 Global DIMP predicted source map (top) for a 5m x 5m square space (full search space) with a Cs-137 point source suspended by clamps on a ring stand, and the corresponding uncertainty (bottom).

Global DIMP also performed well, in spite of minor locational variation in the source. Global DIMP spread the source into four cells located at (4.5, -4.5, 90; 0, 8.5 ,85-not shown; 8.5, 8.5, 70-not shown; and -42.5, 0, 75) collectively containing 94.6% of the true source activity with fairly low uncertainty and a lower chi-squared value of 1.77. It also was able to search the entire measurement space. While the collective source strength is more promising, only 67.58% of it is in the correct location and the more distant cells contain 16.6% (this cell is still only about 20 cm away) and 10.4% (for the anomalous cell) of the true source activity respectively. The distant source cell (shown in Figure 5.4) is positioned outside of the field of view of both detector measurements taken in the west quadrant (-x half), so DIMP may be merely accounting for the anisotropy of the radiation field imposed by the thin metal ringstand located on that side of the source that is not well represented by the coarse mesh of the adjoint transport solver. A small source under the western detectors would be equivalent in accounting for the slightly higher response values observed from the eastern quadrant (+x half) detectors.

5.2 HEU Disk Source

5.2.1 Measured Results

The first HEU case involved a calibrated disk source held by a steel ringstand clamp in the center of a 5m x 5m x 3m empty floorspace. Figure 5.5 shows the predicted logarithmic source map with uncertainty calculated by the original local DIMP search algorithm, while Figures 5.6 and 5.7 show the results from a single global search at slices z=90 cm and z=80 cm, respectively.

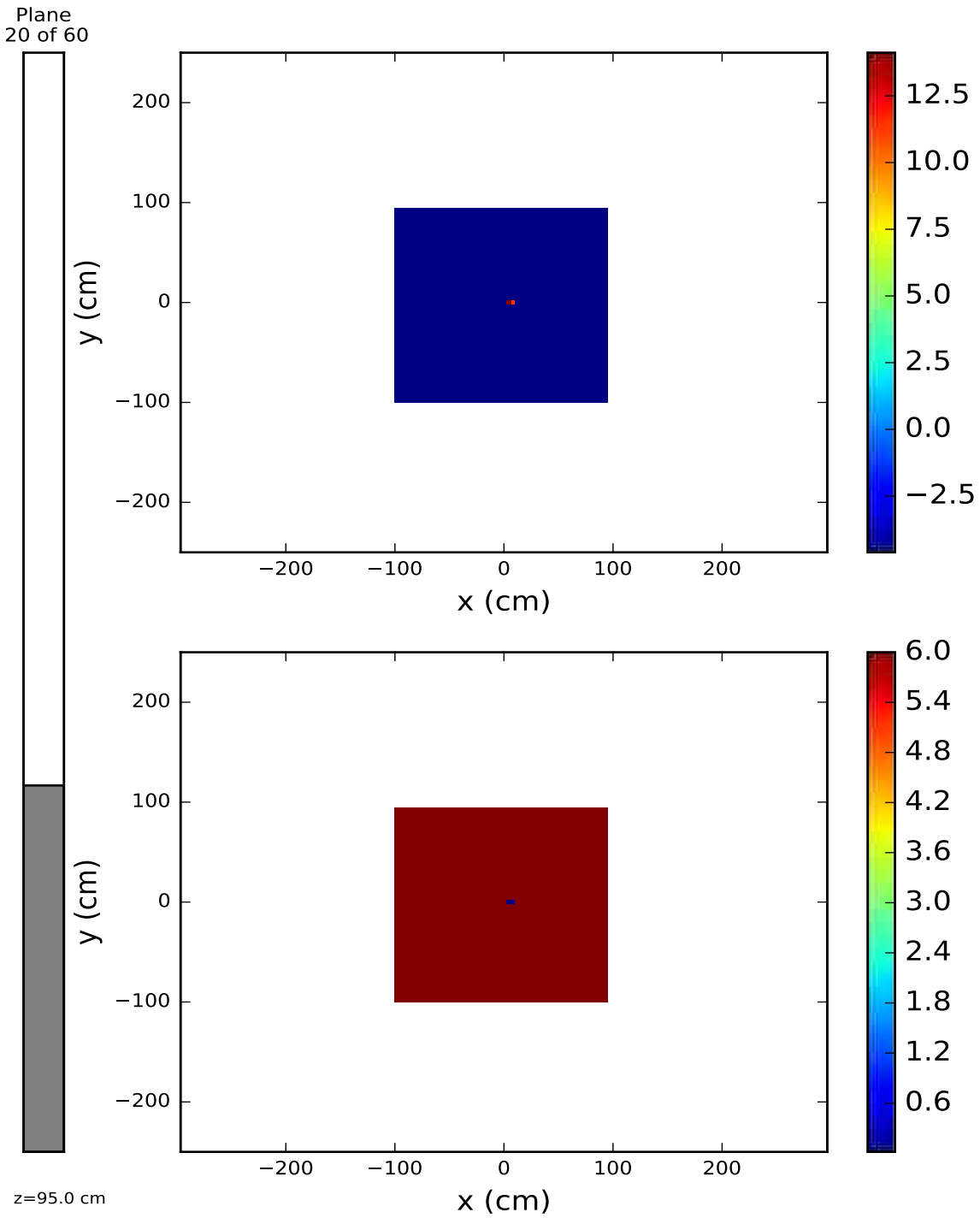

Figure 5.5 HEU disk 186 keV group local DIMP predicted source map (top) for a 5m x 5m square space (reduced to a 2m x 2m search) with corresponding absolute uncertainty (bottom).

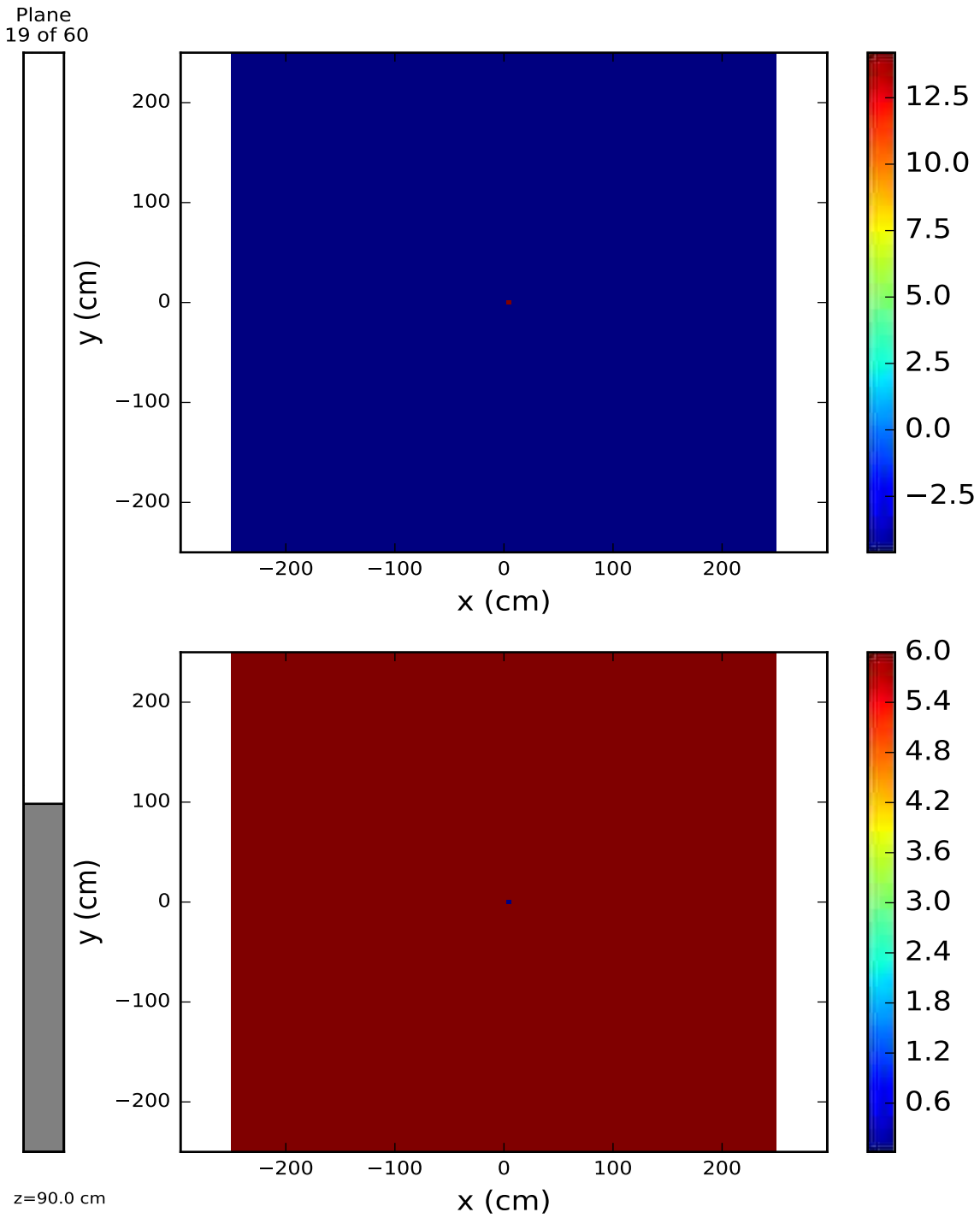

Figure 5.6 HEU disk 186 keV group global DIMP predicted source map (top) for a 5m x 5m square space (full search space) with corresponding absolute uncertainty (bottom).

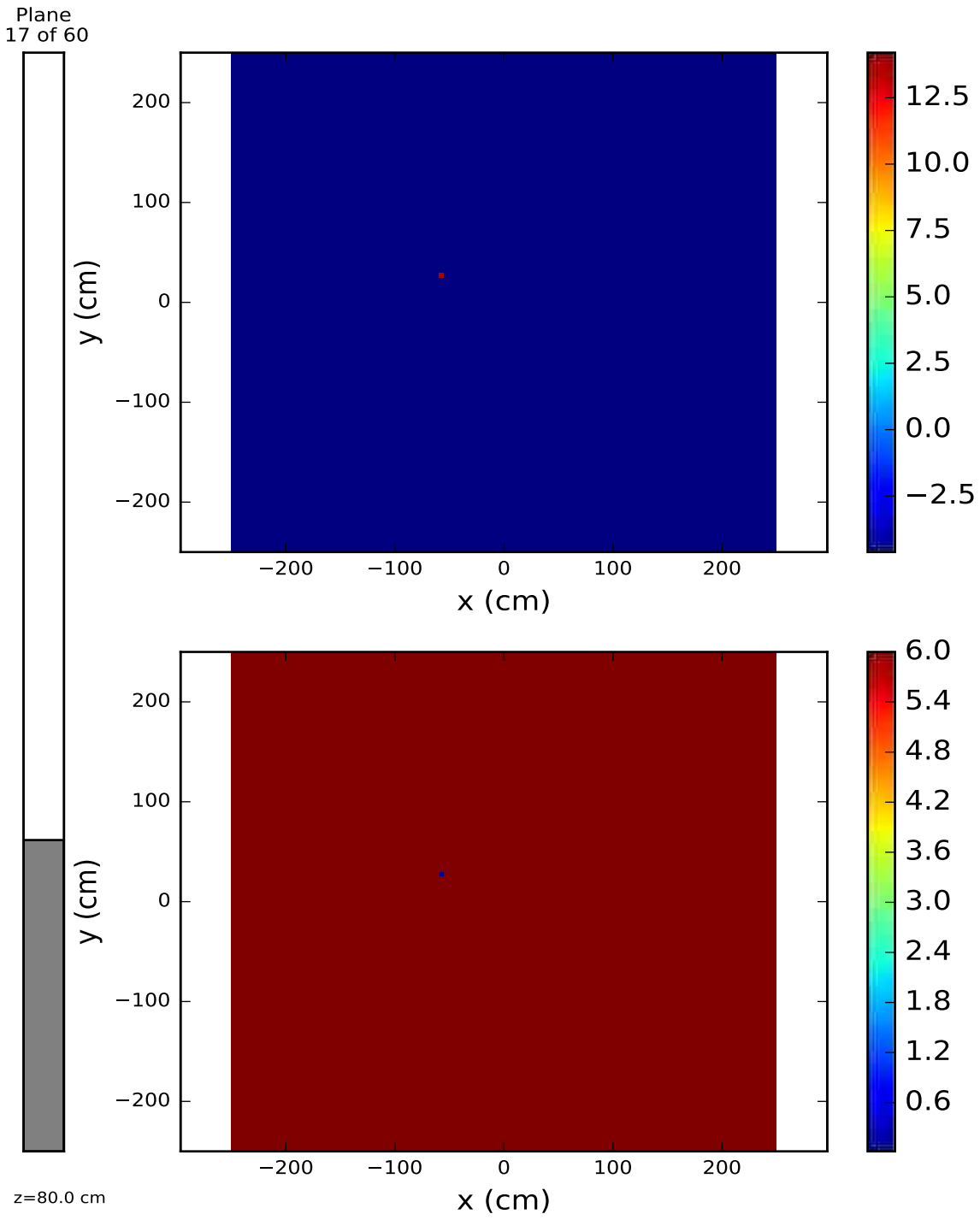

Figure 5.7 HEU disk 186 keV group anomalous global DIMP predicted source (top) and corresponding uncertainty (bottom).

As shown in Figure 5.5, DIMP's local search appeared to perform well predicting the source in cells that neighbor the correct cell (4.5,0,95 & 8.5,0,95) cm with 265% of the true source activity with fairly low uncertainty for the 186 keV gamma-ray and a much higher chi-squared value (2287) than the Cs-137 point source validation values in Section 5.1. The higher chi-squared value is inherent to all of the HEU measurements and reflects the greater difficulty in measuring Uranium due to increased peak interferences at 186 keV and the low resolution of NaI detectors. The true source location was in cell (0,0,95). Unfortunately, here too the search volume had to be reduced by nearly a factor of ten in order for the optimizer to converge to this solution (an inconvenient limitation), and the low intensity 164 keV gamma-ray was too weak to be detected. The global search algorithm was included in DIMP in order to relieve that restriction.

Figure 5.6 shows the results from a ten iteration basin-hopping search across the entire experimental volume. A smaller anomalous source (approximately half of the strength of the dominant source cells near the true source location) was also predicted in this global search (Figure 5.7) 21 cells away from the true source location. At first glance, the global search appears to have performed slightly worse predicting three source cells (4.5,0,90; -57.5,27.5,80; and 8.5,0,95 - not shown) cm containing collectively 407% of the value of the true source strength with low uncertainty for the 186 keV gamma-ray. However, the global search computation time scaled linearly with the number of local search iterations, and the global search method slightly improved the overall chi-squared value by about 2% (representing a slightly better solution with a lower sum of the square errors). Furthermore, global DIMP succeeded in finding the source out of the entire 5m x 5m x 3m room instead of the reduced search limitation imposed by local DIMP. For comparison, HMS-4 predicted 10.91 grams of material with an uncertainty of 0.19 grams out of 10.97 grams (true quantity). This great result is unsurprising as this was the same source used to calibrate HMS-4 system initially. Note, the full HMS-4 output sheet can be found in Appendix A.

There are two likely contributions for DIMP's overestimation of the total source strength. First, the measured responses were generally much higher than the calculated fluxes at the detector (at least an order of magnitude difference). Possible reasons include neglecting to simulate the emissions in the 185 keV energy range from several uranium decay products and the overlapping of the 144, 164, 185, and 205 gamma ray spectral lines with NaI's low spectral resolution. This may have contributed to a breakdown of the point detector response function model for converting detector response peaks to uncollided fluxes. While peak fitting errors were greater than for Cs-137, they were bound by about 30% uncertainty and the intrinsic detector efficiency bias bounded by approximately 40% uncertainty as well. Note that this only measures the direct divergence from Gaussian shape and not necessarily the full area under the peak added by the tail of the nearby 164 keV peak.

Furthermore, the intrinsic detector efficiency bias could be amplified by a 40% uncertainty in mean chord length. Both the mean chord length and the intrinsic efficiency were calculated

using particle tracking calculations in MCNP. The efficiency was low for the collimated detector, which made the number of particles likely to pass through the detector crystal also low and the corresponding uncertainty high. Using several iterations of the Weight Windows [22] global variance reduction technique, the variance in the efficiency and the chord length were reduced to nearly half of their analog values.

Next, the flux models in DENOVO were then directly compared to MCNP models and analytical point source models as a sanity check. No large discrepancies were observed. Only a 20% difference was found due to differences in source geometry representation (a point source versus a 5 cm x 5 cm x 5 cm DENOVO source cell).

Therefore, it is conjectured that the remaining error must be attributed to the measurements directly. Higher measured responses can occur from either detector equipment malfunction or the presence of an unknown source of uranium. For example, a detector multi-channel analyzer (MCA) cable short circuited during a measurement and had to be replaced. Also, the detector fell to the ground once after slipping from the clamp on the ringstand. The only noticeable aberration that resulted from those events was calibration drift, which had to be corrected by a temporary energy calibration for a few measurements. Also, small human errors in measurement may have contributed, but the increase in response amplitudes would be minimal except when the detector was located in close proximity to the source or at the edge of the source. Only a handful of measurements were performed in these types of configurations for each source validation.

In order to estimate the experimental measurement error, simulated MCNP F8 detector responses were spread with the semi-empirical Gaussian Energy Broadening function (fit using data from the detector calibration in Ref. [12]) and compared to measured responses. An MCNP F8 response and the measured response for location 9 specified in Table 4.4 are shown in Fig. 5.8.

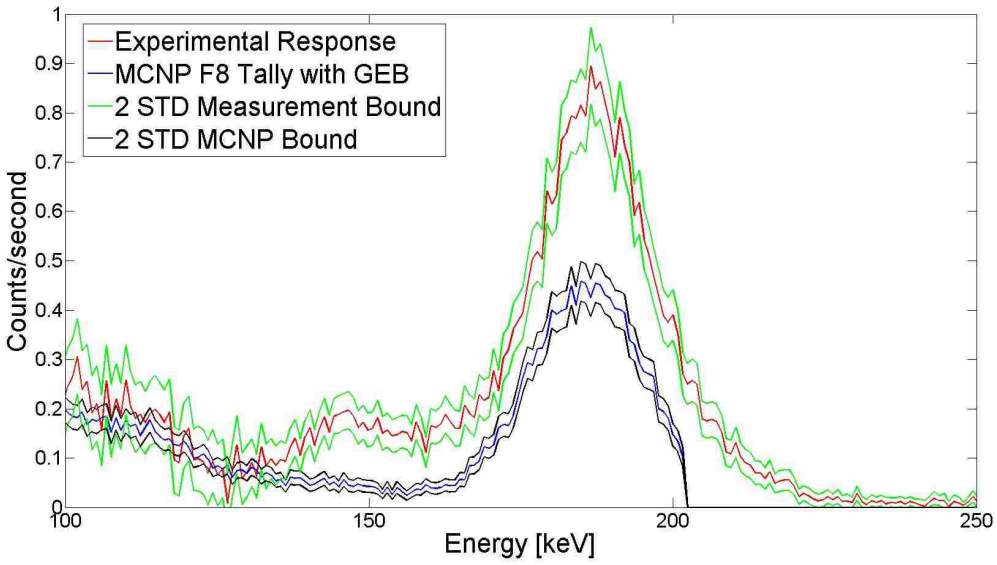

Figure 5.8 Experimental and MCNP F8 detector responses at measurement point 9 (40,0,91), which is inline with the source at 40 cm away (0,0,91) cm

Note the large differences in peak amplitude of about a factor of two. The measurement error combined with the other possible sources of errors mentioned previously come closer to accounting for the differences observed between the calculated DENOVO and uncollided peak fluxes (calculated from peak fits of the measured responses). Furthermore, it is unlikely that small inaccuracies in detector position or angle created these errors, as the collimated detector's solid angle to the source would only be greatly improved for measurements taken at the source edges. Most were not taken at the edges of the source of interest. Therefore, the measurement problem conjecture is supported.

Again, the anomalous source cells appearing in the global search source map likely occurred from poor representation of the steel ringstand pole by the coarse mesh used in the adjoint calculation. One measurement had particularly low count rate due to obscuration of the source by the pole, which may have permitted the alternate source configuration. A stronger source located behind the weak response detector would produce a similar set of detector responses to those where the weak detector's view was obstructed by a pole.

5.2.2 Synthetic Results

In order to eliminate modeling misrepresentation of the experimental HEU disk source, a global DIMP search was conducted using synthetic uncollided gamma-ray fluxes calculated by MCNP at the corresponding detector locations. Full detector geometry was maintained and the responses

were corrected by the same collimation factor calculated earlier for the measurements. The global DIMP predicted source map for the synthetic HEU disk case is shown in Figure 5.9.

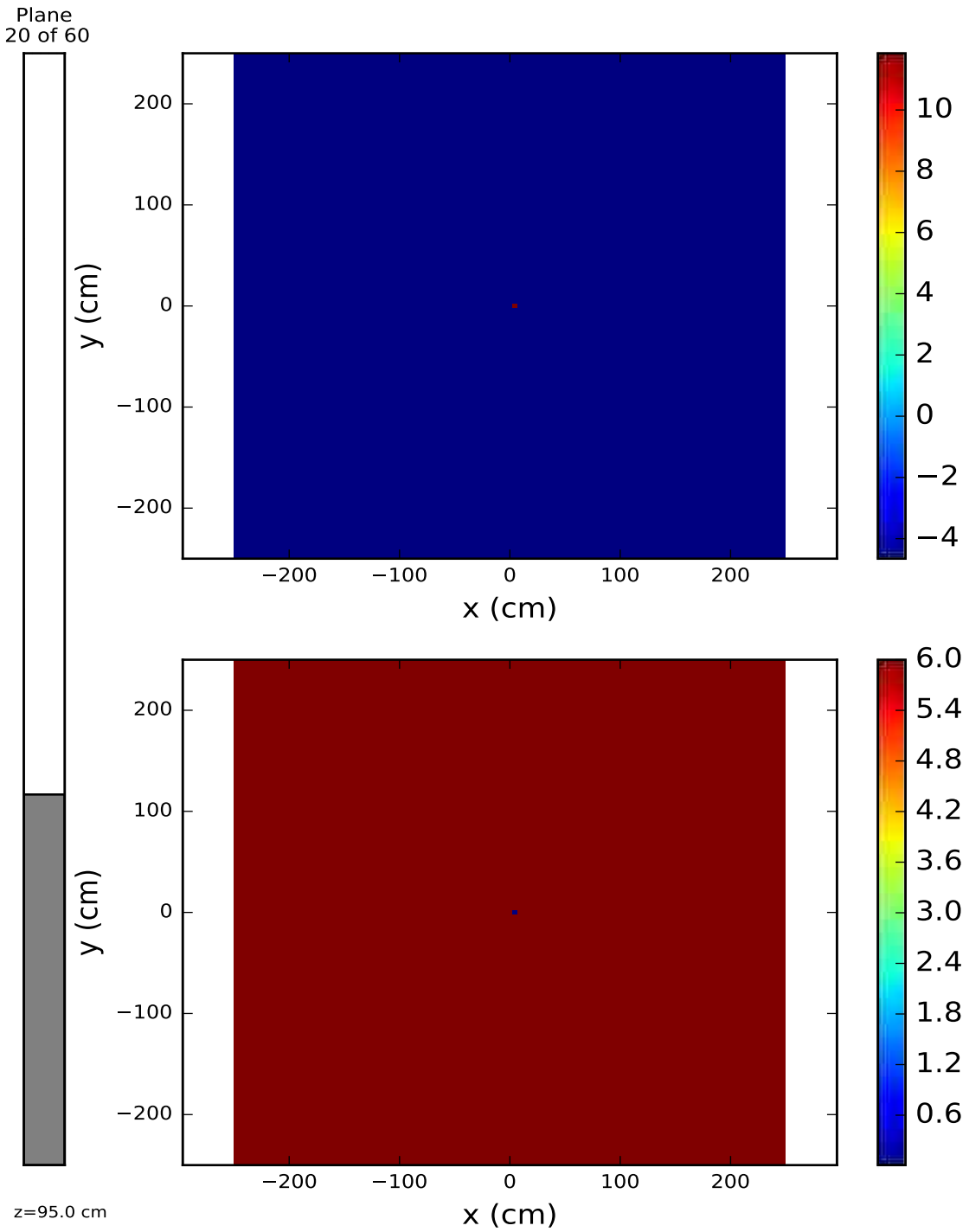

Figure 5.9 HEU disk 186 keV group global DIMP predicted source for a 75m^3 volume using synthetic data (top) and corresponding uncertainty (bottom).

Global DIMP predicted the source cell (4.5, 0,95) cm containing collectively 25% of the value of the true source for the 186 keV with comparable uncertainty to the measurements. Unfortunately, global DIMP did not converge a reasonable solution for the low intensity 164 keV gamma-ray group, but the chi-squared value was slightly lower at 2203. The underestimation was confirmed to be mostly due to an artifact of the cell geometry by running an MCNP simulation of the $5cm^3$ cell with the appropriate strength and comparing it to the disk. The responses were similar for both geometries. Considering a factor of three difference due to source geometry representation multiplied by the 407% source difference observed by global DIMP in the measurements, the difference approaches the factor of ten or more observed in the responses.

5.3 HEU Line Source

5.3.1 Measured Results

Another measurement case involved a set of six highly enriched uranium line sources taped together end to end along the y-axis of the 5m x 5m x 3m floorspace at a height of 116 cm. The sources were each approximately 30 cm in length and 1 cm in diameter. The sources were aligned along the bottom of the small round duct (as shown in Section 4.3). Figure 5.10 shows the predicted logarithmic source map and uncertainty calculated by DIMP's local search algorithm.

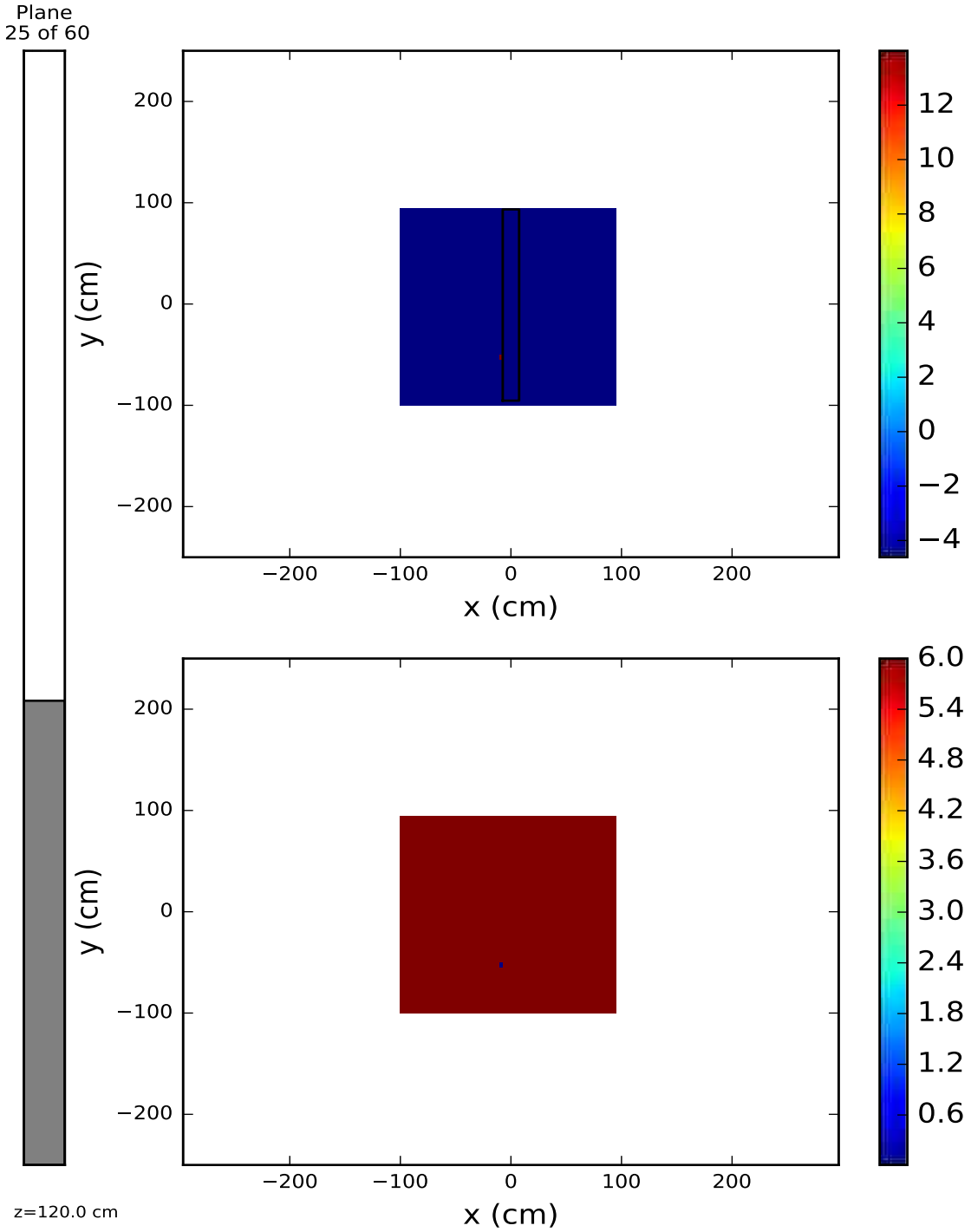

Figure 5.10 Local DIMP predicted sources for the small round duct in a 75m^3 volume (top) and corresponding uncertainty (bottom).

Local DIMP predicted concentrated the line source into a single cell located at (-8.5, -52.5, 120) cm containing collectively 253 % of the value of the true source for the 186 keV gamma-ray with a low prediction uncertainty (again, the 164 keV gamma-ray was too weak to detect) and a high chi-squared value of 10,825. With the exceptionally high chi-squared value and inconsistently large discrepancies in responses, DIMP likely struggled to resolve the line. So, it is likely that the strongest line source location coincides with the point source location. For comparison, HMS-4 predicted the line source to contain 5.89 grams of material with an uncertainty of 0.02 grams out of 9.17 grams (true quantity). HMS-4 underpredicted the source by about a third, which is likely due to differences in the material form measured (U_3O_8) and the form HMS-4 was calibrated with (U metal). Note, the full HMS-4 output sheet can be found in Appendix A. Only the local DIMP search was conducted because similar discrepancies to the HEU disk case between the detector measured fluxes and the calculated fluxes were found. Using the true source guess as an initial guess improved the mapping of the line source distribution but did not improve the source strength overestimation issue. It is likely that the HMS-4 results remained unaffected due to the initial detector response and system calibration.

5.3.2 Synthetic Results

Synthetic MCNP data was again used to avoid the measurement discrepancy in the HEU line source detector fluxes. Originally, the method used in Section 5.2 was attempted using the full ORNL collimated detector geometry for MCNP simulated directional detector fluxes, but global DIMP failed to converge to a source solution. Unshielded detectors avoid the added error introduced by the collimation factor and the large differences between the ORNL field detector DRF and the DIMP point DRF.

Unfortunately, the original 13 detector locations chosen were insufficient to resolve the HEU line source with unshielded synthetic detector response data. So, similarly to the previous convergence studies described in Chapter 3, sets of five unshielded detector points were added from 5 detectors to 40 detectors to determine the number necessary to resolve the HEU line source. The global DIMP predicted source map for the synthetic HEU line case using 25 unshielded detector responses is shown in Figures 5.11 and 5.12.

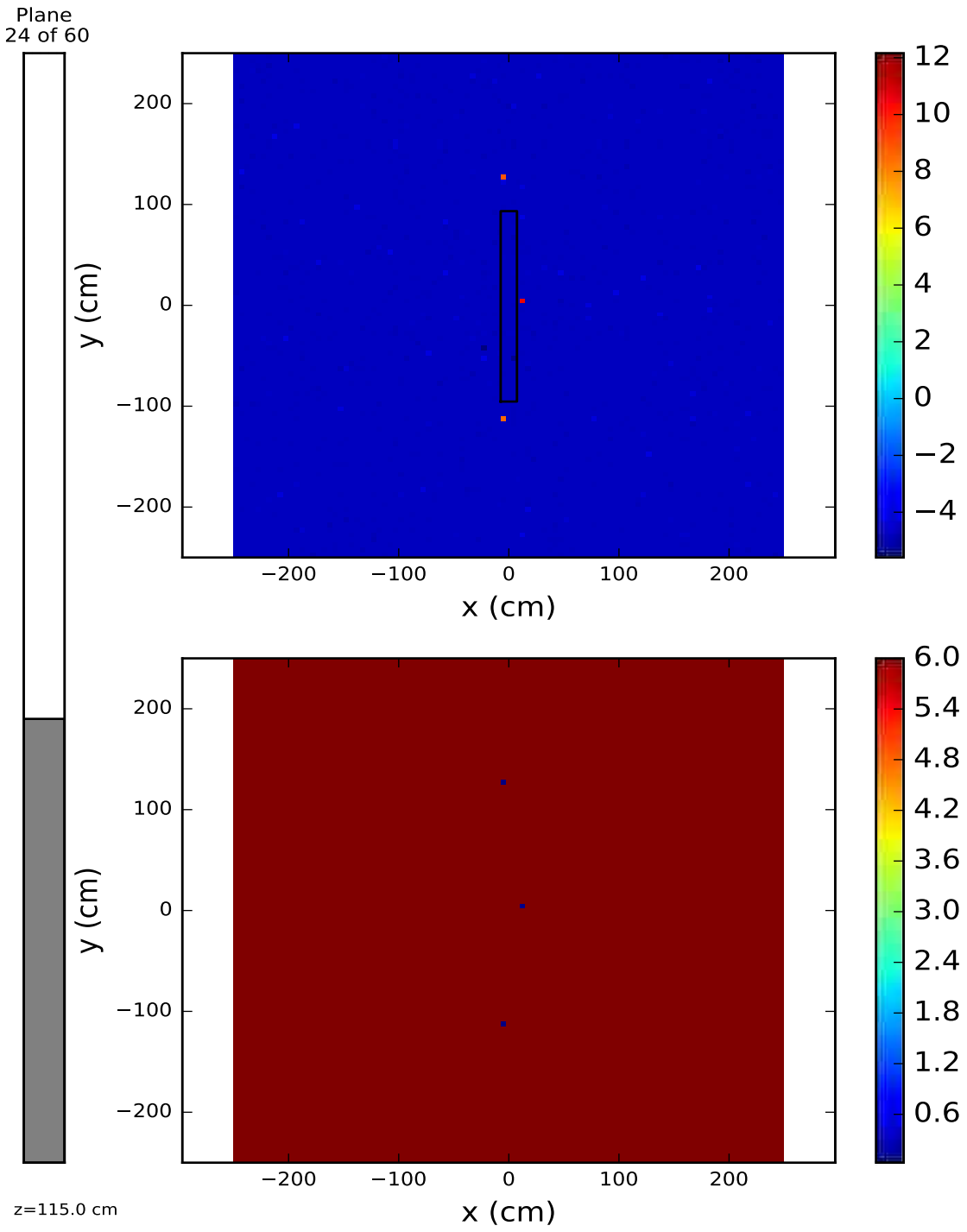

Figure 5.11 Global DIMP predicted sources for the small round duct in a 75m^3 volume using synthetic data (top) and corresponding uncertainty (bottom).

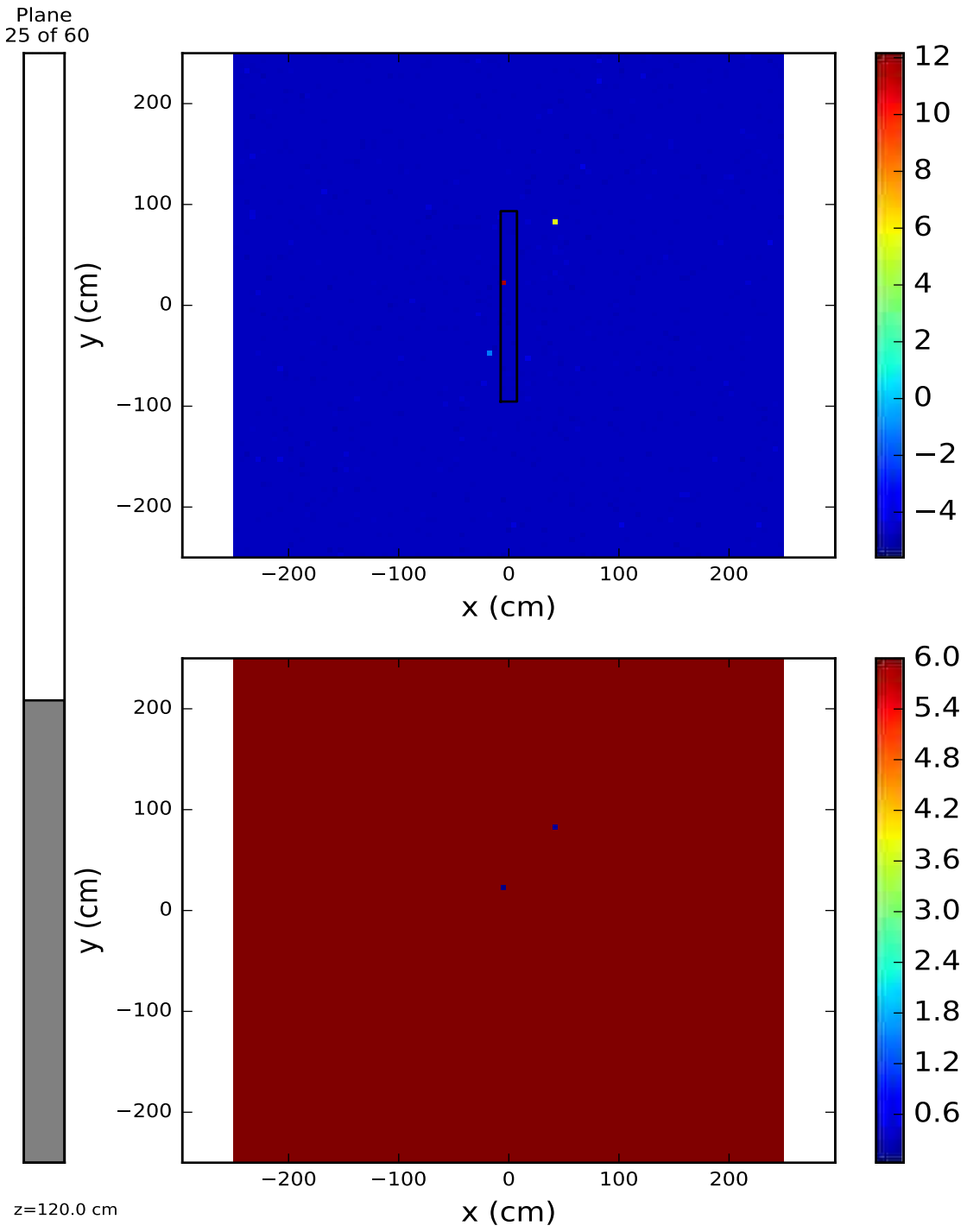

Figure 5.12 Global DIMP predicted sources for the small round duct in a 75m^3 volume using synthetic data (top) and corresponding uncertainty (bottom).

Global DIMP predicted the source cells (-4.5, 22.5,117.5; 12.5, 4.5, 112.5; -4.5, 127.5, 112.5; -4.5, -112.5, 112.5; and several other source cells slightly outside the pipe- not shown) cm containing collectively 85.5% of the value of the true source with comparable overall prediction uncertainty to the measurements for the 186 keV gamma-ray. A significantly lower chi-squared value of 21.2 was achieved over both the disk synthetic data run and the line measurement. The true source cell coordinates are (0, from -89.5 to 93.5, 116) cm. Most of the source error resulted from competing similar solutions in the pipe walls with strengthened intensities and solutions just outside of the pipe boundaries with weakened intensities. Similar results were observed with the 164 keV gamma-ray group with a weaker collective prediction of 31% of the true source strength, and more source cell locations were predicted just outside of the pipe. The underestimation was mainly due to competing weakened source solutions placed outside of the pipe, and differences between the DIMP mesh cells and the true source volume. The effect of the competing solutions is shown in the convergence graphs (Figures 5.13-5.15) formed by DIMP solutions across increasing detectors in increments of five detectors from 5 to 45 unshielded detector locations.

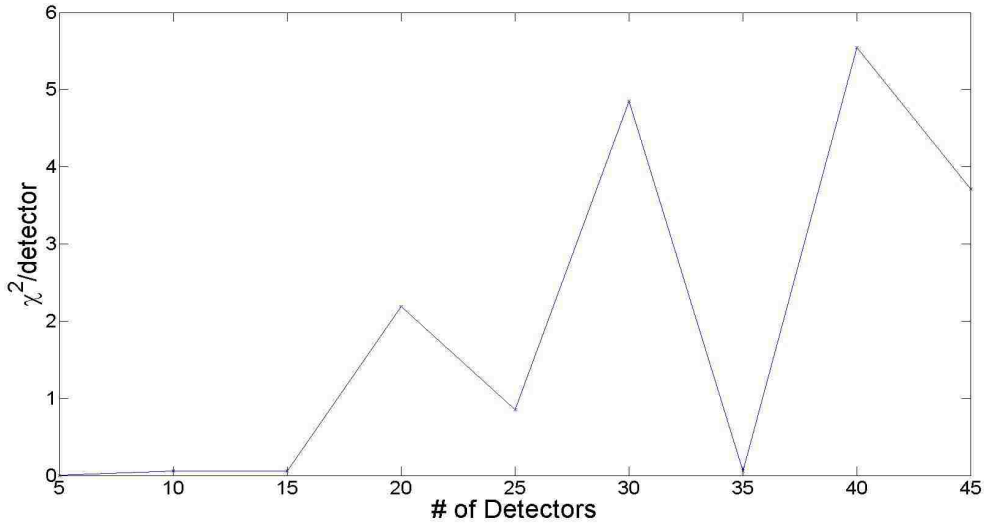

Figure 5.13 Chi-squred value of 10 iteration global DIMP searches from 5-45 unshielded detector locations.

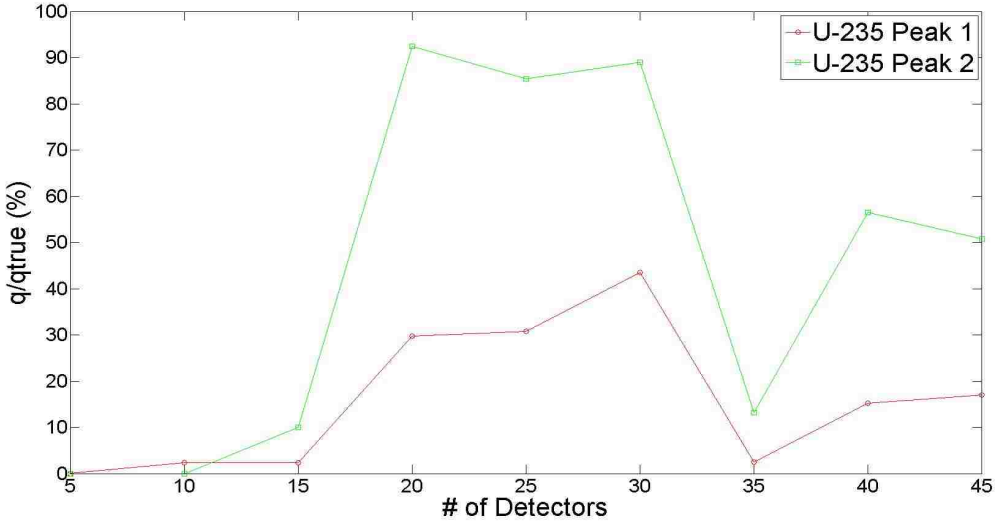

Figure 5.14 Percent of the true source strength value achieved by a 10 iteration global DIMP searches from 5-45 unshielded detector locations (164 keV and 186 keV gamma-ray peaks respectively).

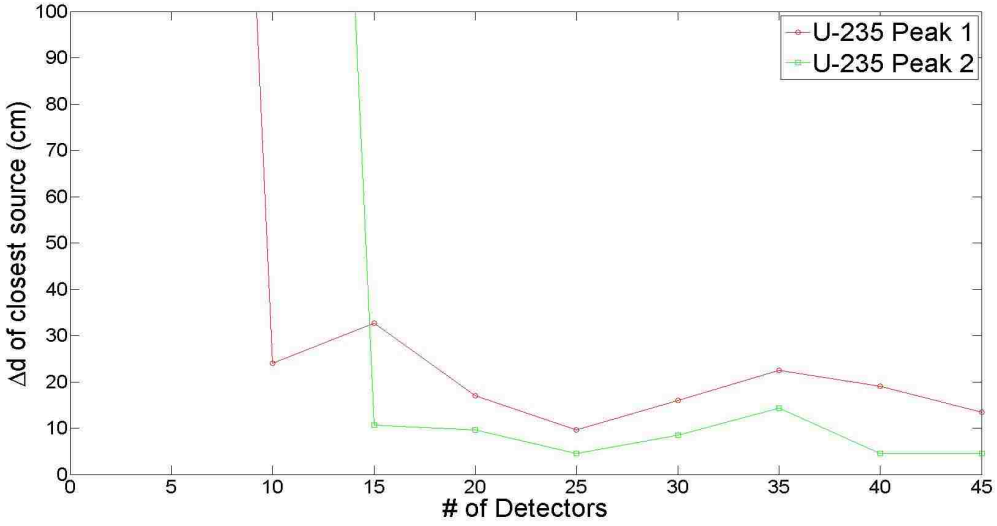

Figure 5.15 Distance of the closest source from the true source location achieved by a 10 iteration global DIMP searches from 5-45 unshielded detector locations (164 keV and 186 keV gamma-ray peaks respectively).

DIMP does not converge to a solution in both gamma-ray energies for the HEU line until at least 15 detector locations are selected. For both the 15 and 35 detector solutions, low intensity source solutions outside of the small round duct dominated. Beyond 20 detector locations (with the exception of 35 detector), 30% of the source solutions were fairly correct within the pipe and 70% were weaker and just outside the pipe boundary. Weak solutions just outside of the pipe again dominated the solution for 35 detectors. This behavior appears to point to a limitation of DIMP's uncollided flux point detector response function model. Without particle scattering (collided flux) information contained in a detector response continuum, the optimizer cannot distinguish an attenuated solution inside an object from a weaker unattenuated solution just outside of the object.

Attenuated source limitations aside, the unshielded case forthe HEU line source performed well with a sufficient number of detectors. The number of detectors is somewhat comparable to the original DIMP model of taken 7 measurements per detector location (one unshielded detector and six shielded directional detector measurements along +x,-x,+y,-y,+z, and -z). For a single source, generally the directional measurements would have three nonzero response measurements (facing the source) and three zero source measurements (facing away from the source). This model required a minimum of 5 detector locations for a simple point source to converge and predict a nonzero solution, and 5 detector locations would equal 20 measurements total, that is (5 detector locations) =(5 locations) x (3 directions + 1 unshielded)=20 responses minimum. This is a favorable result because unshielded detectors do not have to be aligned with the source in a measurement, have greater detection efficiency, and a much simpler DRF with less sensitivity to source solid angle measurement geometry (useful for future model improvements). DIMP could be used to predict sources from a passive, fixed, and unshielded, detector measurement grid in nuclear facilities, which could help to automate more of the NDA measurement process.

Finally, the last validation exercise, the HEU area sources in the L-Duct scenario, was not tested with DIMP due to the measured response discrepancy issues found with the earlier HEU cases. The measured data and parameters shall be preserved for future reference.

CHAPTER

6

CONCLUSION

The local DIMP inverse radiation transport source mapping method originally developed was analyzed for convergence stability as the number of detector points were increased from 3 to 24. The quality of solution was measured through reductions in the chi-squared values and comparison of the predicted source characteristics (energy, location, and strength) to the true source values. Local DIMP proved to be stable after correcting for a few model assumptions. DENOVO's point DRF model did not always simulate the correct directional response when set in line with the axis of the source, and the MCNP lead block synthetic detector response approximation created higher errors for detectors that were too close to the source. These errors were controlled manually in other simulations and will be corrected in future versions of the code.

The detector locational uncertainty study randomized a hundred detector locations and simulated groups of responses to predict source solutions in Hykes's benchmark problem. Groups of detectors were chosen from 7-24 detectors in realization sets of 10 or 100. Global DIMP reduced the spread of uncertainty in source prediction for many detector groupings below 20. However, both local and global DIMP suffered multiple solutions according to similar problems seen in the validation results. Weak sources close to the detectors and stronger sources in the walls were again indistinguishable from the true source solution. Also, it was found that detectors that are too close to other detectors, close to walls and corners, and very far away from sources should be avoided if possible. The first two are easily controlled but the third one may be impractical in some scenarios.

Local DIMP correctly predicted the Cs-137 point source in the first validation after the lead

collimator effects were simulated and corrected, but as with previous work required the search space to be reduced in order to converge to the correct solution. Often, local DIMP struggled with getting stuck in local minima (incorrect alternate solutions) that had similar chi-squared values to the true solution. Mesh refinement, source search space reductions, alternate optimization methods, and source guess preconditioners were identified as possible improvements to DIMP to address the local minima problem. The source search space reduction approach was a partial and simple solution that carried a price. Space reduction requires analyst assumptions on the location of the radioactive source. Unknown sources could escape detection if they lie within the eliminated space (i.e. spills, floor, etc.).

The global optimization search was developed for DIMP through the basin-hopping algorithm to address the local minima problem. It improved results overall when compared to the previous local DIMP search by more consistently identifying lower chi-squared value sources while performing full source space searches. Unfortunately, results worsened for the HEU validation cases (disk and line source cases). There was a large discrepancy by an order of magnitude in several cases between the measured responses and the calculated responses. The DENOVO calculated responses were verified using the analytical solution (calculated from the calibrated source data) and MCNP models. The peak fitting algorithm produced some discrepancies from the actual to the fitted curve due to overlapping of multiple peaks. Peaks tended to overlap for HEU due to the low resolution of NaI. This error was smaller than the differences between the measured and calculated responses. Finally, an MCNP F8 tally was used to simulate the experiment geometry and compute a detector response spectrum. The simulated response reflected a factor of two of difference between the peak amplitudes, which when combined with the other sources of error approaches the differences between the previously calculated DENOVO and experimental flux responses. This led to the conclusion that there was either an unknown measurement error (additional interference sources), equipment malfunction, a breakdown in peak uncollided flux DRF model when it is applied to overlapping peaks and a low detector efficiency, or some combination of these three effects occurred. Further sources of error include un-simulated Uranium decay products, source geometry differences between DIMP predicted source cells and actual source dimensions, and possible incompatibilities between the corrected point DRF model and the ORNL field holdup detector collimator true DRF.

Synthetic data was used in place of the measured data to validate DIMP. DIMP provided a fairly accurate point source solution, but the accuracy of the source distribution worsened with the long line source in a pipe problem. The point solution was predicted accurately in location, but with a decreased source strength due to large differences between the actual thin disk dimensions and the much thicker mesh cell dimensions. DIMP tended to split between two types of solutions. One solution was fairly close to the true solution with accurate source strength. The second competing solution simulated sources within 20 cm of the true location outside of the pipe with significantly reduced source strengths (to compensate for the lack of attenuation). DIMP appears to be unable to

distinguish weak uncollided sources closer to the detectors from stronger, more attenuated sources. This weakness could be improved by the incorporation of collided detector responses and improved comprehensive DRFs (peak and continuum inclusion).

6.1 Future Work

A better DRF could be developed that can include a continuum response model for DIMP. The continuum response represents gamma-ray Compton scattering effects resulting from attenuators between the source and detector. With this information DIMP could distinguish between attenuated and un-attenuated sources of radiation. Furthermore, the peak fitting algorithm could also be improved to accommodate detector response photopeak overlap and multi-peak complexes. Doing so would likely increase agreement between DIMP's calculated responses and measured responses.

While DIMP was validated using synthetic data, this still only counts as an "inverse misdemeanor." This is acceptable because the MCNP models incurred Monte Carlo variance (with sufficient particle histories) in a manner consistent with the Poisson variance of a radiation detection measurement and produced responses sufficiently different from those modeled by DENOVO. Additional measurements should be performed with an unshielded detector and uranium sources to fully validate DIMP and resolve any lingering detector response disagreement.

Although time and measurement issues prevented direct analysis of the HEU area sources in the L-Duct, further analysis could be performed using synthetic data. Such a complicated set of multiple sources could provide a rigorous benchmark for the DIMP code. This case was the most realistic and applicable to nuclear facilities, so it should be highly considered for future computational analysis.

Lastly, other global optimization methods could be considered to further improve DIMP performance such as Stochastic Gradient Descent [23]. DIMP could also be supplemented in the field by using lidar scans of the facility to create informed priors and direct mapping of geometry structures for the code. Furthermore, previously discovered holdup sources could be used to calibrate the DIMP initial prior and monitor the predicted source maps for any distortion in those known sources.

REFERENCES

[1] J. M. Hykes and Y. Azmy, "Radiation Source Mapping with Bayesian Inverse Methods," *Nuclear Science and Engineering*, vol. 179, pp 1-17, 2015.

[2] X.-5. M. C. Team, "MCNP-A General Monte Carlo N-Particle Transport Code, Version 5," Los Alamos National Laboratory, Los Alamos, NM, 2003.

[3] T. D. Reilly, "Nondestructive Assay of Holdup," *Passive Nondestructive Assay of Nuclear Materials 2007 Addendum*, Washington D.C.: Los Alamos National Laboratory, 2007.

[4] S. E. Smith, et al., "Holdup Measurement System 4 (HMS4)-Automation & Improved Accuracy," BWXT Y-12 report Y/DK-2190, ORTEC, 2004. [Online]. Available: `http://www.ortec-online.com`. [Accessed 16 August 2016].

[5] A. Tarantola, *Inverse Problem Theory and Methods for Model Parameter estimation*, Philadelphia: Society for Industrial and Applied Mathematics, 2005.

[6] F. Li, et al., "Implementation of the Monte Carlo-Library Least-Squares Approach to Energy Dispersive X-Ray Fluorescence Analysis," *International Centre for Diffraction Data*, vol. 1097, issue 2, pp 227-235, 2008.

[7] J. Mattingly and D. Mitchell, "A Framework for the Solution of Inverse Radiation Transport Problems," *IEEE Transactions on Nuclear Science*, vol. 57, issue 6, pp 3734-3743, 2010.

[8] D. G. Cacuci and M. Jonescu-Bujor, "Sensitivity and Uncertainty Analysis, Data Assimilation, and Predictive Best-Estimate Model Calibration," *Handbook of Nuclear Engineering*, New York: Springer, 2010.

[9] E. E. Lewis and W. F. Miller Jr., *Computational methods of neutron transport*, La Grange Park, IL: American Nuclear Society, 1993.

[10] J. Hykes, "Radiation Source Mapping with Bayesian Inverse Methods," PhD Thesis, North Carolina State University, 2012.

[11] R. P. Gardner and A. Sood, "A Monte Carlo simulation approach for generating NaI detector response functions (DRFs) that accounts for non-linearity and variable flat continua," *Nuclear Instruments and Methods in Physics Research B*, vol. 213, pp. 87-99, 2004.

[12] N. Nelson, "Validation and Uncertainty Quantification of a 1x2" NaI Collimated Detector Using Detector Response Functions Created by g03," MS Thesis, North Carolina State University, 2014.

[13] *Scale: A Comprehensive Modeling and Simulation Suite for Nuclear Safety Analysis and Design*, ORNL/TM-2005/39, Version 6.1, June 2011. Available from Radiation Safety Information Computational Center at Oak Ridge National Laboratory as CCC-785.

[14] D. J. Wales and J. P. K. Doye, "Global Optimization by Basin-Hopping and the Lowest Energy Structures of Lennard-Jones Clusters Containing up to 110 Atoms," *Journal of Physical Chemistry A*, vol. 101, pp 5111-5116, 1997.

[15] Z. Li and H. A. Scheraga, "Monte Carlo-minimization approach to the multiple-minima problem in protein folding," *Proceedings of the National Academy of Science, USA*, vol. 84, pp 6611-6615, 1987.

[16] R. C. Smith, *Uncertainty Quantification*, Philidelphia: Society for Industrial and Applied Mathematics, 2014.

[17] L. Ingber, "Simulated annealing: Practice versus theory," *Journal of Mathematical Computerl Modeling*, vol. 18, iss. 11, pp 29-57, 1993.

[18] Eckert & Ziegler Isotope Products, "Eckert & Ziegler Reference & Calibration Sources: Product Information," Valencia, CA, 2007.

[19] National Nuclear Data Center, "Nudat2.6: Decay Radiation Search," Brookhaven National Laboratory, 2013. [Online]. Available: `http://www.nndc.bnl.gov/nudat2/indx_dec.jsp`. [Accessed 14 June 2015].

[20] GBS Elektronik GmbH, "MCA 166-USB: Multi channel analyzer with USB interface," GroBerkmannsdorf, Germany, 2008.

[21] P. Russo, "Gamma-Ray Measurements of Holdup Plant-Wide: Application Guide for Portable, Generalized Approach," Los Alamos National Laboratory report LA-14206, May 2005.

[22] T.E. Booth and J.S. Hendricks, "Importance estimation in forward Monte Carlo calculations," *Nuclear Technology/Fusion*, vol. 16, issue 13, pp 90-100, 1984.

[23] S. Mei, A. Montanari, and P. Nguyen, "A mean field view of the landscape of two-layer neural networks," *Proceedings of the National Academy of Sciences of the United States of America*, vol. 115, iss. 33, pp E7665-E7671, 2018. [Online] Available: `https://doi.org/10.1073/pnas.1806579115`. [Accessed 6 November 2018].

APPENDIX

APPENDIX

A

HMS-4 OUTPUTS

Holdup Measurement System 4

Print Date: 5/21/2015 **Total Grams by Area/Equipment** Page No.: 1

AREA	LOCATION	DATE	TIME	SRC	GRP	SPEC. MASS (g,g/cm,g/cm^2)	SPEC MASS UNC (g,g/cm,g/cm^2)	LENGTH (cm)	AREA (cm^2)	TOTAL(g)	TOTAL UNC(g) uncty	sd in mean
0601	003	05/21/15	09:01	P	-	10.91435	0.19290	0.0	0.0	10.91	0.19	
									EQUIP. GRAMS:	10.91	0.19	
									GRAND TOTAL:	10.91	0.19	

Figure A.1 HMS-4 Output Sheet for the HEU disk source.

Holdup Measurement System 4

Print Date: 5/28/2015 **Total Grams by Area/Equipment** Page No.: 1

AREA	LOCATION	DATE	TIME	SRC	GRP	SPEC. MASS (g,g/cm,g/cm^2)	SPEC MASS UNC (g,g/cm,g/cm^2)	LENGTH (cm)	AREA (cm^2)	TOTAL(g)	TOTAL UNC(g) uncty	TOTAL UNC(g) sd in mean
0602	001	05/28/15	12:11	L	-	0.03391	0.00031	30.7	0.0	1.04	0.01	
0602	002	05/28/15	13:22	L	-	0.03296	0.00031	30.7	0.0	1.01	0.01	
0602	003	05/28/15	14:33	L	-	0.03136	0.00030	30.7	0.0	0.96	0.01	
0602	004	05/28/15	15:42	L	-	0.03081	0.00030	30.7	0.0	0.94	0.01	
0602	005	05/28/15	16:52	L	-	0.03155	0.00030	30.7	0.0	0.97	0.01	
0602	006	05/28/15	18:04	L	-	0.03139	0.00030	30.7	0.0	0.96	0.01	
								EQUIP. GRAMS:		5.89	0.02	
								GRAND TOTAL:		5.89	0.02	

Figure A.2 HMS-4 Output Sheet for the HEU line source.